



University of Crete
School of Sciences



Department of Materials Science and Technology

&

Foundation for Research and Technology - Hellas

Doctor of Philosophy Thesis

Light localization and diagnostics in micro-structured optical fibers



Nikolaos I. Korakas

Supervisor: Director of Research Dr. S. Pissadakis

Supervising Professor: M. Kafesaki

Co-supervisor: Prof. G. Petekidis

Heraklion, Crete

2023



Πανεπιστήμιο Κρήτης
Σχολή Θετικών Επιστημών



Τμήμα Επιστήμης και Τεχνολογίας Υλικών
&

Ίδρυμα Τεχνολογίας και Έρευνας

Διδακτορική Διατριβή

Διατάξεις εγκλωβισμού και διασποράς του
φωτός σε μικρό-δομημένες οπτικές ίνες

Νικόλαος Ι. Κόρακας

Επιβλέπων: Διευθ. Ερευνών Δρ. Σ. Πισσαδάκης

Υπεύθυνη καθηγήτρια: Μ. Καφεσάκη

Συνεπιβλέπων: Καθ. Γ. Πετεκίδης

Ηράκλειο, Κρήτη

2023

Table of Contents

Ευχαριστίες	9
Χρηματοδότηση- Funding	11
Abstract	12
Περίληψη	14
1 Introduction	17
1.1 Whispering gallery modes resonators	17
1.2 Glass poling of optical fibers.....	20
1.3 Silk Fibroin as an optoelectronic material.....	23
1.4 Aim and motivation of this Thesis	26
1.5 Outline of this Thesis	28
2 Light propagation in optical fibers	30
2.1 Single-mode optical fibers and their corresponding parameters	30
2.2 Total internal reflection	32
2.3 The optical fiber's numerical aperture	35
2.4 Waveguide modes in standard optical fibers.....	36
2.5 Tapered optical fibers	47
2.6 Summary.....	50
3 Theoretical foundations of this Thesis topics.....	51
3.1 Whispering gallery modes (WGMs) theory	51
3.1.1 Whispering gallery modes	51
3.1.2 Wave equation for cylindrical resonators	54
3.1.3 Tapered optical fiber-microresonator coupling	59
3.2 Thermal poling basic theory	62
3.2.1 Single-Carrier Model	62

3.2.2	Multiple-Carrier Model	63
3.3	Theoretical description of Strain-Optic effect in cylinders	66
3.4	Summary.....	72
4	Whispering gallery mode resonances in thermally poled borosilicate glass hetero-fibers	73
4.1	Borosilicate glass hetero-fiber.....	73
4.2	Thermal poling experimental setup.....	75
4.3	WGMs experimental setup.....	77
4.4	Optical and material diagnostics procedures.....	78
4.5	Type of thermal poling anode	79
4.6	Thermal poling results in Nitrogen Flow	80
4.6.1	Microscopy mapping using non-linear techniques.....	80
4.6.2	WGM spectra obtained experimentally in hetero-fiber cavities...	82
4.6.3	Structural investigations of the hetero-fiber WGM cavities.....	84
4.6.4	Finite element analysis simulations.....	90
4.7	Thermal poling results without implementing nitrogen flow.....	96
4.8	Chapter conclusions	101
5	A study of silk fibroin photo-elasticity in whispering gallery modes cavities	102
5.1	Silk fibroin.....	102
5.2	Methods and experimental setup.....	104
5.2.1	Extraction of the silk fibroin.....	104
5.2.2	Silk fibroin cavity preparation for forming WGM resonators....	105
5.2.3	Experimental setup	107
5.2.4	Brillouin Light Scattering measurements	110

5.2.5	Calibration of the strain fork apparatus	113
5.2.6	Finite element analysis of the component's strain tensors	117
5.2.7	Raman measurements	119
5.3	Spectral Results	120
5.4	Details of simulations for mode allocation in silk fibroin cavities ...	128
5.5	Discussion.....	131
5.6	Chapter conclusions	133
6	Thesis Conclusions and future plans	135
6.1	WGMs resonances in thermally poled glass optical cavities	135
6.2	WGMs resonances in silk fibroin optical cavities.....	138
	References	140
	Publications	156

Στην οικογένειά μου

Ευχαριστίες

Καθόλη τη διάρκεια της εκπόνησης της διδακτορικής μου διατριβής στάθηκαν δίπλα μου αρωγοί πολλοί άνθρωποι που συνέβαλαν καθοριστικά στην επιτυχή ολοκλήρωσή της. Ως ένδειξη ευγνωμωσύνης προς το πρόσωπό τους θα ήθελα να αναφερθώ παρακάτω σε αυτούς και στην πολύτιμη βοήθειά τους.

Αρχικά θα ήθελα να ευχαριστήσω τον επιβλέποντά μου, Διευθυντή Ερευνών του Ι.Η.Δ.Α., Δρ. Σταύρο Πισσαδάκη, ο οποίος μου έδωσε την ευκαιρία να εργαστώ στο εργαστήριό του και επίσης μου παρείχε όλη την υλικοτεχνική και επιστημονική υποστήριξη που χρειάστηκα. Οι συμβουλές του και τα σχόλιά του βελτίωσαν αναμφισβήτητα την ποιότητα της δουλειάς μου ενώ οι ανταλλαγές απόψεων κατά τη διάρκεια της διδακτορικής μου διατριβής συνέβαλαν αναμφίβολα στην εμβάθυνση των επιστημονικών μου γνώσεων.

Στη συνέχεια θα ήθελα να ευχαριστήσω την επιβλέπουσα καθηγήτριά μου στο Τμήμα Επιστήμης και Τεχνολογίας Υλικών του Πανεπιστημίου Κρήτης Μαρία Καφεσάκη καθώς επίσης και τον συνεπιβλέποντα καθηγητή στο ίδιο τμήμα, Γεώργιο Πετεκίδη. Επίσης θερμές ευχαριστίες και στα υπόλοιπα μέλη της επταμελούς επιτροπής, στον ομότιμο καθηγητή του τμήματος Φυσικής του Πανεπιστημίου Κρήτης Δ. Χαραλαμπίδη, στον αναπληρωτή καθηγητή του τμήματος Φυσικής του Πανεπιστημίου Κρήτης Ι. Κομίνη, στην καθηγήτρια του Τμήματος Επιστήμης και Τεχνολογίας Υλικών του Πανεπιστημίου Κρήτης Α. Μητράκη και τέλος στον ερευνητή Β΄ του Εθνικού Ιδρύματος Ερευνών Χ. Ριζιώτη.

Θα ήθελα να κάνω ιδιαίτερη αναφορά σε δύο άτομα που έπαιξαν καίριο ρόλο στην επιτυχή ολοκλήρωση του διδακτορικού μου. Αρχικά στον φίλο και συνεργάτη μου Δρ. Γιώργο Βιολάκη ο οποίος ερχόμενος στο εργαστήριο με βοήθησε τα μέγιστα στα πρώτα βήματα της ερευνητικής μου σταδιοδρομίας. Εξίσου σημαντική ήταν και η συνεισφορά του συνεργάτη μου Δρ. Οδυσσέα Τσιλιπάκου ο οποίος υποστήριξε σε τεράστιο βαθμό το θεωρητικό μέρος της

διατριβής, προσφέροντάς μου την ευκαιρία να επεκτείνω και να εμβαθύνω τις γνώσεις μου.

Να ευχαριστήσω ακόμα όλα τα άτομα με τα οποία συνυπήρξαμε αυτά τα χρόνια στο εργαστήριο φωτονικών υλικών και διατάξεων με ιδιαίτερη αναφορά στην Δρ. Μαρία Κωνσταντάκη για την αμέριστη βοήθειά της.

Θα ήθελα επίσης να ευχαριστήσω όλους τους συνεργάτες μου στις επιστημονικές δημοσιεύσεις που παρήχθησαν μέσα από αυτήν τη διδακτορική διατριβή καθώς ο ρόλος τους ήταν καταλυτικός με ιδιαίτερη αναφορά στον Δρ. Βασίλη Τσαφά.

Ιδιαίτερη μνεία θα ήθελα να κάνω σε τρεις φίλους μου, τον Βασίλη Τσαφά, τον Ανδρέα Λεμονή και τον Χρήστο Ντούλια με τους οποίους είχαμε εποικοδομητικές επιστημονικές συζητήσεις όλα αυτά τα χρόνια και οι οποίοι επίσης με βοήθησαν στη βελτίωση της παρουσίασης της διδακτορικής μου διατριβής.

Να ευχαριστήσω επιπλέον όλα τα παιδιά που μοιραστήκαμε αυτά τα χρόνια το ίδιο γραφείο, καθώς ο χρόνος που πέρασα μαζί τους κύλησε αρμονικά και ευχάριστα με ανταλλαγή χρήσιμων συμβουλών.

Τέλος το μεγαλύτερο ευχαριστώ θα ήθελα να το εκφράσω στην οικογένειά μου οι οποία με στήριξε με υπομονή όλα αυτά τα χρόνια.

Σας ευχαριστώ όλους!

Χρηματοδότηση- Funding

Το έργο συγχρηματοδοτείται από την Ελλάδα και την Ευρωπαϊκή Ένωση (Ευρωπαϊκό Κοινωνικό Ταμείο) μέσω του Επιχειρησιακού Προγράμματος «Ανάπτυξη Ανθρώπινου Δυναμικού, Εκπαίδευση και Διά Βίου Μάθηση», στο πλαίσιο της Πράξης «Ενίσχυση του ανθρώπινου ερευνητικού δυναμικού μέσω της υλοποίησης διδακτορικής έρευνας – 2ος Κύκλος» (MIS-5000432), που υλοποιεί το Ίδρυμα Κρατικών Υποτροφιών (ΙΚΥ).



This research is co-financed by Greece and the European Union (European Social Fund- ESF) through the Operational Programme «Human Resources Development, Education and Lifelong Learning» in the context of the project “Strengthening Human Resources Research Potential via Doctorate Research – 2nd Cycle” (MIS-5000432), implemented by the State Scholarships Foundation (IKY).



Abstract

Whispering gallery mode (WGMs) resonances are useful for various applications due to their unique characteristics, such as high Q-factor and sensitivity to changes in refractive index. This thesis explores the potential of utilizing whispering gallery mode resonances to study amorphous materials such as ion-rich glass and silk fibroin protein and to correlate the behavior of the spectral resonances with their specific optical and mechanical properties.

- Whispering gallery mode resonances in thermally polarized glass hetero-fibers with radial symmetry are studied for the first time. In comparison to the spectral behavior of the fibers in their pristine state, the TE and TM polarized responses go through a spectral "cleaning" process; higher-order radial modes are suppressed or eliminated because of radially oriented thermal poling. The thermally poled hetero-fiber WGM cavities have been rigorously simulated utilizing the finite element method. The calculated modal eigenstates and transmission spectra have affirmed the mode selection mechanism introduced by the azimuthally symmetric thermal polling procedure. To reveal the spatial profile of the structural and optical changes introduced to the thermally poled hetero-fibers and correlate them with the WGM spectral measurements, second-harmonic generation (SHG) microscopy, energy dispersive x-ray spectroscopy (EDX), and micro-Raman (μ Raman) measurements were carried out.

- During this research, cylindrical resonators made of silk fibroin were developed and attached to silica glass microfibers. For modal excitation, we employ a technique known as evanescent coupling, which uses optical fiber tapers. In addition, we investigate and analyze the optical birefringence properties of these resonators in the 1.5-micrometer spectral band. Through thermal annealing, silk fibroin undergoes a unique structural transformation from Silk I (amorphous) to Silk II (semi-crystalline). The increase of nano-

crystalline sheet structures in Silk II is accompanied by several modifications to this biomaterial's physical (wettability) and optical (birefringence) properties. The photoelasticity of amorphous (Silk I) and semicrystalline Silk (Silk II) is attributed to the emergence of the β -sheet conformations that dominate the Silk II structure. Photo-elastic experiments are performed, tracing the TE and TM shifts of the whispering gallery mode resonances upon applying an axial strain. The strain optical coefficient K' for Silk I fibroin was found to be 0.059 ± 0.004 , with the corresponding value for Silk II being 0.129 ± 0.004 .

Περίληψη

Οι τρόποι εγκλωβισμού ψιθυρισμού του φωτός είναι χρήσιμοι σε διάφορες εφαρμογές λόγω των μοναδικών χαρακτηριστικών τους, όπως ο υψηλός συντελεστής ποιότητας (Q-factor) και η ευαισθησία στις αλλαγές του δείκτη διάθλασης. Η παρούσα διατριβή εξετάζει τη δυνατότητα της αξιοποίησης των τρόπων εγκλωβισμού συντονισμού του φωτός σε κοιλότητες κυλινδρικής συμμετρίας για τη μελέτη άμορφων υλικών, όπως το θερμικά πολωμένου γυαλιού Duran και της αναγεννημένης φιμπροίνης του μεταξιού, και τη σύνδεση αυτών των συντονισμών με τις συγκεκριμένες οπτικές και μηχανικές τους ιδιότητες.

- Στο πρώτο μέρος της διδακτορικής διατριβής παρουσιάζεται η μελέτη που πραγματοποιήθηκε με τη μέθοδο των τρόπων εγκλωβισμού ψιθυρισμού σε ηλεκτρικά πολωμένες υάλινες οπτικές έτερο-ίνες. Οι TE και TM ρυθμοί ανώτερης της μονάδας τάξης των ηλεκτρικά πολωμένων έτερο-ινών υφίστανται έναν φασματικό “καθαρισμό” σε σύγκριση με τη φασματική απόκριση των αρχικών έτερο-ινών. Η συγκεκριμένη φασματική συμπεριφορά των ηλεκτρικά πολωμένων έτερο-ινών αποδίδεται σε αλλαγές του δείκτη διάθλασης οι οποίες λαμβάνουν χώρα κοντά στην περιφέρεια της έτερο-ίνας. Αυτές οι αλλαγές συνδέονται με ακτινικά συμμετρική ανακατανομή των ιόντων που προϋπάρχουν μέσα στην ύαλο, όπως αυτό προέκυψε από την διαδικασία της θερμικής πόλωσης. Οι φασματικές αποκρίσεις των ηλεκτρικά πολωμένων οπτικών κοιλοτήτων προσομοιώθηκαν χρησιμοποιώντας τη μέθοδο πεπερασμένων στοιχείων. Για να διερευνηθούν οι χωρικές αλλαγές της κατανομής των ιόντων και της δομής της ύαλου που λαμβάνουν χώρα στις ηλεκτρικά πολωμένες έτερο-ίνες πραγματοποιήθηκαν μια σειρά από επιπλέον μετρήσεις χαρακτηρισμού της μορφής της ύαλου. Αυτές ήταν οι εξής: μικροσκοπία δεύτερης αρμονικής τάξης (SGH), φασματοσκοπία διασποράς ενέργειας ακτίνων X (EDX) και

φασματοσκοπία μ -Raman. Οι παραπάνω μετρήσεις αποκάλυψαν ότι υπάρχει μεταβολή στην συγκέντρωση των ιόντων μετά την διαδικασία της θερμικής πόλωσης της υάλου η οποία επιφέρει αλλαγές στην δομή της καθώς και στην συμμετρία του πλέγματος της.

- Σε αυτήν τη μελέτη αναπτύχθηκαν οπτικές κοιλότητες κατασκευασμένες από φιμπροίνη, οι οποίες υποστηρίζουν τρόπους εγκλωβισμού ψιθυρισμού, εναποτεθειμένες σε γυάλινες οπτικές ίνες. Για την διέγερση των οπτικών αντηχείων μεταξιού χρησιμοποιήθηκαν θερμικά εφελκυσμένες οπτικές ίνες γυαλιού μικρής διαμέτρου (2 μm). Ο οπτικός χαρακτηρισμός των συγκεκριμένων οπτικών αντηχείων μεταξιού έγινε στο φασματικό εύρος των 1.5 μm . Μέσω θερμικής ανόπτησης το μετάξι υφίσταται μια δομική μεταμόρφωση από την άμορφη κατάσταση (μετάξι τύπου I) σε μια ημικρυσταλλική κατάσταση (μετάξι τύπου II). Αυτός ο μετασχηματισμός συνοδεύεται από αρκετές ευδιάκριτες αλλαγές στις οπτικές ιδιότητες αυτού του βιοϋλικού, επιπλέον της αύξησης των δομών νάνο-κρυσταλλικών β-φύλλων στο μετάξι τύπου II. Τα φωτοελαστικά πειράματα πραγματοποιήθηκαν καταγράφοντας τις φασματικές μετατοπίσεις των TE και TM τρόπων εγκλωβισμού ψιθυρισμού καθώς εφαρμόζαμε αξονική τάση στο σύστημα. Από τις παραπάνω μετρήσεις και την οπτική και μηχανική ανάλυση τους προέκυψε ότι ο φωτοελαστικός οπτικός συντελεστής K για το μετάξι τύπου I είναι 0.059 ± 0.004 με την αντίστοιχη τιμή για το μετάξι τύπου II να είναι 0.129 ± 0.004 .

1 Introduction

This chapter provides a comprehensive and insightful introduction to three distinct areas of study: whispering gallery mode resonators, the process of thermal poling in optical fibers, and the application of silk fibroin as optoelectronic material. Accordingly, the chapter focuses on each domain's most recent advancements and breakthroughs.

1.1 Whispering gallery modes resonators

Whispering Gallery Mode (WGM) optical microresonators have been extensively studied in the last few decades [1]. Optical WGM microresonators, which confine resonant photons in a microscale volume for extended durations, substantially enhance light-matter interactions, making them an ideal platform for photonic sensors. The light that circulates in the cavity via total internal reflection at specific resonant frequencies interacts with the local environment via the evanescent electromagnetic field. Lord Rayleigh was the first to introduce the term "whispering gallery waves" to describe an acoustic phenomenon in St. Paul's cathedral in London [2]. He observed that whispers at one end of the circular dome could be heard clearly at the opposite end. Whispering gallery modes have unique light resonance properties, making them ideal for applications in various fields, including sensing, non-linear photonics, lasers, and optomechanics. High-finesse cavities, characterized by their small mode volumes, yield exceptional measurement resolution, rendering them perfectly suited for high-precision sensing applications in various fields [3]. The quality factor (Q) serves as a crucial metric to quantify the effectiveness of light localization in a whispering gallery mode (WGM) cavity. The Q factor of WGM resonators signifies the proportion of stored energy to energy dissipation per oscillation cycle, resulting from reflections within the cavity. This parameter provides valuable insights into the performance and efficiency of WGM-based

systems. By using highly transparent, low scattering loss materials such as silica or CaF_2 , WGM resonators can achieve extremely high values of Q factor (10^8 - 10^9) in a small mode volume [4]. The Q factor is mainly limited by material attenuation and scattering loss contributed by surface roughness and geometrical imperfections. WGM cavities can be fabricated from various materials, including silica, CaF_2 , silicon, and polymers. Also, the corresponding cavities can be formed in different geometries, such as micro-spheres, micro-rings, micro-disks, micro-toroids, micro-bottles, and microbubbles. Figure 1.1 shows several examples of microresonator cavities with varying geometries.[5].

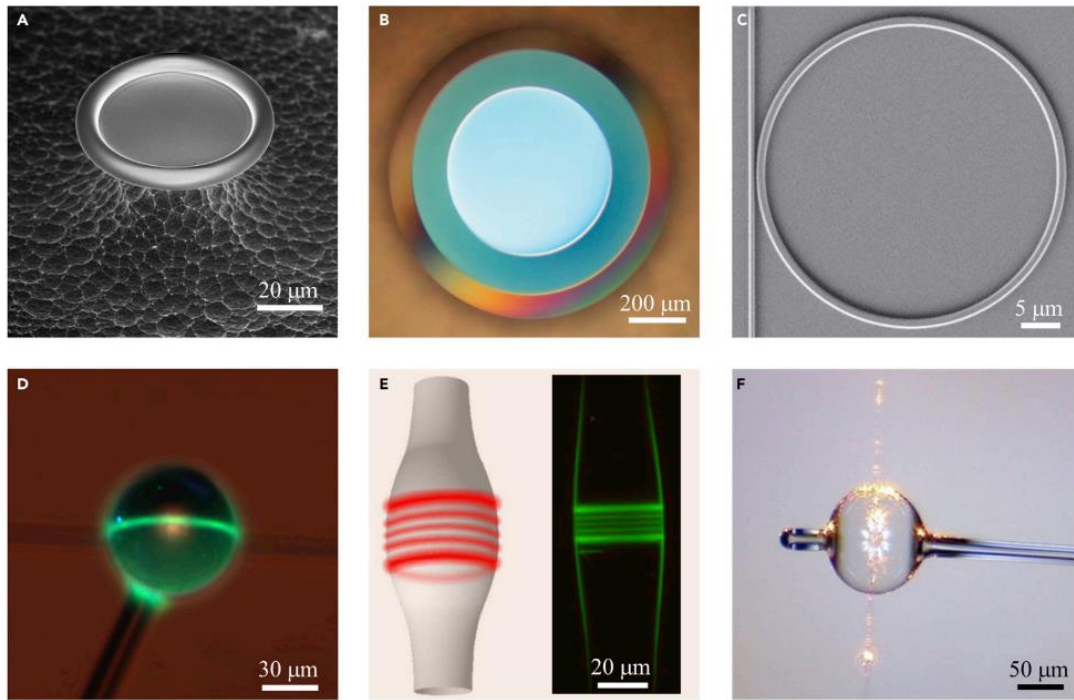


Figure 1.1 (A) Microtoroid (B) microdisk (C) microring (D) microsphere (E) microbottle and (F) microbubble [5]

The literature review will be focused on sensing devices using WGM resonance. Whispering gallery mode sensors provide an accurate solution for sensing physical, chemical, biological, and environmental parameters. Due to their adaptability in materials, geometries, and fabrication methods, they are

ideally suited for various sensing applications, such as temperature [6], pressure and displacement [7], electric and magnetic fields [8], biosensing [9], and gas sensing [10].

Extensive research has been conducted on using WGM resonators for sensing applications, focusing on detecting nanoparticles sized from tens to hundreds of nanometers in biology [11]. Volmer et al. reported in 2008 the detection of a single virus particle (Influenza A) with an average radius of 50 nm using the spectral shift of whispering gallery mode resonances in transmission mode [12]. Following this research, mode splitting [13] and mode broadening [14] sensing mechanisms were utilized to detect virus particles. As the most prevalent biomolecule, proteins are frequently the targets of detection by WGM devices. The studies [15], [16] demonstrate WGM cavities acts as biosensors with sensitivity for detecting unlabeled molecules. Surface-bound aptamers are used in these studies as a capture agent to confer protein specificity on the apparatus. A shift in resonance wavelength is utilized to measure protein binding on the WGM cavities.

Whispering gallery mode (WGM) resonators have also been investigated for gas-sensing applications. The ability to detect gases is useful in various scenarios, from environmental monitoring [17] to medical diagnostics [18]. Gas sensing with WGM resonators is based on detecting changes in the refractive index of the resonator caused by the adsorption of gas molecules onto the resonator's surface. This effect changes the optical path length of the WGMs circulating in the resonator, resulting in a shift in the resonant frequency. The high Q factor of WGM resonators provides high sensitivity and resolution in gas sensing applications in the ppm range. Most experiments involve coating a WGM device with a chemoresponsive layer sensitive to the target gas. Various gases have been detected using WGM resonators, including hydrogen, carbon dioxide, methane, ethanol vapors, and ammonia vapors [19]–[21].

WGM resonators can be used as sensors for electric and magnetic fields by utilizing the electro- and magneto-striction of a material [22]. PDMS spheres

have been used as electric-field sensors [23], with a higher resolution achieved (0.027 pm/Vm^{-1}) using a composite resonator structure consisting of a silica microsphere with a PDMS coating [24]. Moreover, creating a magnetic-field sensor out of PDMS microspheres is possible by incorporating magnetically polarizable particles into the polymer matrix before curing [22].

In the field of pressure and force detection, researchers have adopted a variety of configurations. The main design encompasses the use of WGM structures as transducers. Changes in device morphology are induced by force exerted on the WGM structure itself, resulting in mechanical stresses manifesting as refractive index fluctuations. This methodology has been efficaciously exhibited with both solid [7] and hollow [25] resonators, wherein the latter's hollow architecture confers the advantage of facilitating pressure transduction for subsequent measurement. Further, a method entails submerging the WGM cavity within a transduction medium or fastening the device directly to a polymer transducer [26].

These cutting-edge devices hold the potential to unlock novel perspectives and enable more accurate, real-time measurements, ultimately contributing to a greater comprehension of our environment.

1.2 Glass poling of optical fibers

Micro photonic device design relies heavily on precisely manipulating optical materials' linear and non-linear permeabilities across three spatial dimensions. Optical fibers are typically made from glasses, a material known as an amorphous dielectric. Parity inversion is invariant [27] in amorphous dielectrics because they are isotropic and centrosymmetric at the macroscopic scale. Thus their non-linear dielectric susceptibility $\chi^{(2)}$ is zero. Myers et al. [28] introduced thermal poling, a technique for inducing second-order susceptibility within glasses, in 1991. The concept behind the method is to heat the glass under a relatively strong static electric field. Therefore, electromigration occurs when the

glass reaches a temperature where the mobility of the glass containing alkali ions is no longer negligible. The ions progressively migrate, creating a static electric field within the glass. This induced static electric field becomes permanent when the glass is cooled down with the externally applied electric field until the glass reaches room temperature. While the above method was initially implemented for bulk glasses, thermal poling of a D-shaped fused silica optical fiber was presented by Kazankasy et al. [29]. Later different poling geometries were used, with the most adopted one being a twin-hole step-index silica fiber with the electrodes (anode and cathode) embedded into the two channels of the fiber [30], [31]. Following the publication of the preliminary findings, many additional works on poling silica twin-hole fibers, such as the one by Wong et al. [32], were published. They were the first to discover the existence of the frozen-in electric field E_{DC} in a poled fiber by employing a Mach–Zehnder interferometer in their research. The method employed allowed them to determine the magnitude and directional component of the frozen-in field. A space-charge region is generated exclusively in the area surrounding the channel where the anodic electrode is inserted by the standard anode-cathode configuration used for thermal poling silica fibers. The disadvantage of the anode-cathode configuration is that the distance between the two channels is relatively short (only 10-20 μm), significantly increasing the risk of unintended electric arcing discharge through the glass due to the elevated voltages. However, in 2009 Margulis et al. [33] demonstrated that connecting both embedded electrodes to the same anodic potential could form a depletion region around both electrodes. The reduced potential for electrical breakdown through the fiber is the primary advantage of this new thermal poling configuration. They also demonstrated that the $\chi^{(2)}$ produced by the cathode-less technique is larger and more stable than the corresponding produced by conventional poling. Four different electrode configurations were used to thermally polarize a twin-hole optical fiber in a study published in 2012 by An et al. [34].

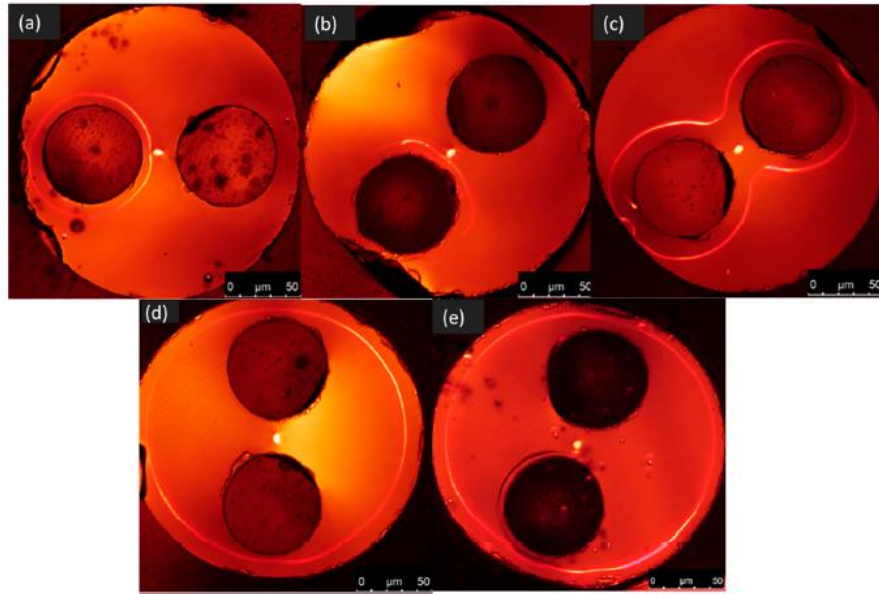


Figure 1.2 Second harmonic generation (SHG) micrographs of twin-hole silica fibers poled in various electrical configurations. The figures are extracted from the work of An et al. [34], [35]

These configurations used one anode wire, two anode wires, one cathode wire, and two cathode wires inserted inside the fiber's channels. To visualize the spatial distribution of the second-order nonlinearity that was created inside the poled fibers and to measure its magnitude, the second harmonic microscopy (SHM) method was utilized (Fig. 1.2).

There has been renewed interest in the thermal poling of glasses in recent years. Unlike the well-studied poling of silica glasses, the outcomes of thermally poling ion-rich glasses have been notably different. Ion-rich glasses exhibit various interesting phenomena after thermal poling, such as altering the wettability of the surface [36], changing the reactivity of the glass surface [37], inducing refractive index changes [38], enhancing the glass hardness [39], along with improved crystallization capability [40].

1.3 Silk Fibroin as an optoelectronic material

Traditional silicon-based electronics no longer fully meet market needs due to the rapid development of the Internet of Things (IoT) and the arrival of 5G, primarily because of mechanical mismatch in nonplanar application scenarios. This opens up new possibilities for flexible optoelectronics, which can avoid physical rigidity using flexible materials. Some applications include flexible sensors/actuators [41], flexible cells [42], flexible displays [43], electronic skins [44], and flexible integrated microsystems [45]. The global market for commercial flexible electronics is anticipated to generate \$77.3 billion in revenue by the end of 2029, expanding at a CAGR of 8.5% between 2018 and 2029 [46]. Nevertheless, the continued development of flexible optoelectronics is currently met with several significant obstacles, including, for example, the need for superior flexible materials, a sustainable energy supply, and the integration of multiple functionalities. Preparing functional components made of organic or inorganic materials on a flexible substrate, which bestows the device with excellent bendability, stretchability, and adaptability while ensuring normal working conditions, is the general method of a flexible optoelectronic device is realized. Because of their remarkable mechanical properties, such as long-term repeatable bendability and stretchability, flexible materials, such as polytetrafluoroethylene [47], polydimethylsiloxane (PDMS) [48], polyimide [49], fluorinated ethylene propylene [50], and silicone rubber [51], play a crucial role in the process of achieving flexibility in electronic devices.

On the other hand, most of them cannot offer the biocompatibility and biodegradability necessary for applications involving implantable and wearable devices. In addition, most of these materials are rather pricey, which creates hurdles for implementing them in large-scale applications. To address the aforementioned issues, researchers have made numerous attempts to develop biocompatible, biodegradable, and cost-effective flexible natural biomaterials, such as cellulose, pectin, chitosan, melanin, and silk fibroin (SF) [52].

Compared to other biological materials, silk fibroin has many advantages that render this distinct. These include its biocompatibility and biodegradability, as well as its adjustable water solubility, excellent optical transmittance, high mechanical robustness, lightweight, and ease of processing. Natural silk fibers made by insects like silkworms and spiders—are the source of Silk Fibroin. Similar in structure but not composition [53], silk from the silkworm (*Bombyx mori*) and spider silk contains glycine-rich proteins. Silk Fibroin can be prepared from the cocoons of the silkworm (*Bombyx mori*), which is more practical and feasible due to its amenability to industrial-scale production [54]. Flexible electrodes, flexible sensors, flexible power supply devices, electronic skins, etc., have all been reported as being based on some form of SF in the last decade [55]. Silk fibers have been explored as an unconventional substrate for electronic sensors, demonstrating promising results.

The electronic skin is considered the premium example of on-skin electronics, comprising flexible films that can conform to the shape of the human body. Silk films, with their remarkable biocompatibility, superior mechanical properties, and exceptional light transmittance, make them a top candidate for electronic skin applications. In a study by Huang et al. [56], a Silk fibroin composite membrane was used as a substrate for electronic skins, demonstrating exceptional stretchability and heat resistance. These membranes were then layered with a silver membrane electrode, and heating and temperature sensing functions were added by proceeding silk fibroin with silver and platinum nanofibers networks. The silk fibroin-based composite membranes could withstand temperatures exceeding 160 °C and stretch by more than 200% without fracturing. Even more remarkable is that no immune response was detected after several days of applying the electronic skin to a human arm.

In biomedical and biological research, the potential for versatile applications involving real-time and in vivo monitoring of analytes with heightened sensitivity has been recognized due to the innovative manipulation of plasmonic resonances and the biocompatibility of plasmonic devices. It has been reported that a biocompatible and highly adaptable plasmonic bio/chemical sensor,

comprising natural silk protein and a gold nanostructure, has been developed [57]. The silk plasmonic absorber sensor capitalizes on the potent local field enhancement within the metal-insulator-metal resonator. The silk protein assumes the dual role of an insulating spacer and substrate—the silk-insulating spacer, which possesses hydrogel properties, exhibits controlled swelling upon exposure to water-alcohol mixtures. Experimental and numerical demonstrations have shown that alterations induce considerable spectral shifts in reflectance minima in the silk spacer's physical volume and refractive index during the swelling process.

Konstantaki et al. [27] demonstrated a silk fibroin-coated optical fiber long-period grating to monitor alcohol vapor concentration. The silk fibroin utilized as a chemo-sensing transducer is discussed to devise an optical fiber sensing instrument aimed at methanol vapor monitoring. In the sensor configuration described, drop casting onto an optical fiber Long Period Grating (LPG) creates a thin silk fibroin layer. The research team has examined the sensor's response in methanol vapors, comprehensively analyzing its sensitivity and measurement repeatability.

Linhua Xu et al. presented in 2016 [58] an on-chip all-silk fibroin whispering gallery mode (WGM) microresonator fabricated with simple molding and technique. The fabricated silk protein microresonators exhibit high-quality factors on the order of 10^5 . In addition, the silk fibroin microtoroid was employed as a thermal sensor with greater sensitivity (1.17 nm/K) than previous WGM-based thermal sensors.

1.4 Aim and motivation of this Thesis

The objectives of this thesis involve two parts that utilize whispering gallery modes resonances to exploit light localization in micro-resonators and conduct studies on amorphous materials, specifically ion-rich glass and silk fibroin. The resonances of WGMs are then correlated with the specific optical and mechanical properties of the materials studied.

Regarding the investigation of ion-rich glass through WGM resonances, the subsequent factors can be identified as the driving forces behind it. The modal selection mechanisms of WGM cavities hold immense potential in various applications, including single-mode operation in light emission devices and spectral interrogation in sensing configurations. The tuning of WGMs resonances has been a topic of considerable research interest, with researchers investing substantial effort into adjusting the optical properties of cavity materials. Specifically, the real and imaginary refractive index components in linear and nonlinear susceptibility domains have been manipulated to fine-tune spectral characteristics [59]. Multiple approaches have been explored for their potential to control resonances in single WGM cavities selectively. These approaches include plasmonic layers [60], highly absorbing refractive index media [61], and the loss-gain interaction in cross-coupled systems [62]. Our work utilizes the thermal poling process to adjust the linear and non-linear susceptibility of a hetero-fiber composed of optical glass and a metal core, which serves as a WGM cavity. This thesis was focused on the study of the area adjacent to the anode side, more precisely on the two zones that emerged after the thermal poling process with varying ionic concentrations. Utilizing the whispering gallery modes resonance technique and its high finesse and small mode volume to investigate the specific region near the anode side was a novel approach and had not been previously presented to the best of our knowledge. Observations of refractive index changes in the vicinity of the anode side were made subsequent to the thermal poling process. As a result of these changes, high-order radial modes were selectively suppressed, leading to the “cleaning”

of the WGM spectrum. Through the use of second harmonic generation microscopy, we confirmed the introduction of the non-linear susceptibility $\chi^{(2)}$, which may be used in future work involving WGMs resonators and non-linear conversion methods.

Regarding the motivation of silk photoelasticity studies, optical biomaterials offer various mechanical, segmentation, and surface chemistry properties, all contributing to the optical biomaterials' ability to perform multiple physical and chemical functions. The functions above can potentially speed up the process of incorporating such materials into advanced and functional sensing, imaging, and actuating photonic devices [63]. The silk that has been extracted from Bombyx Mori is a natural biomaterial that is well-known for its applications in clothing as well as surgery. At the same time, the regenerated form of its fibroin protein has been the subject of significant research into its potential applications in optical circuits, drug delivery systems, and sensing components [64]. This enables the realization of skin-attachable components with readily accessible optoelectronic functions [65]. The photo-elasticity of silk fibroin presents a significant challenge to developing silk-based wearable photonic devices. Specifically, this refers to how much the silk fibroin's refractivity and birefringence will change in response to mechanical stimulation. For instance, the operation characteristics of optical devices in adhesive contact with human skin tissue can depend on the mechanical forces directly exerted at the interface region of the device. Our aim in this work was to study the photoelastic properties of silk fibroin by employing WGM light resonance [66] in cylindrical resonators cast onto glass fiber-supporting beams. The polarization-sensitive, modal dispersion of light confinement made possible by WGM resonance enables the detection of minimal birefringence changes, yielding the stress-optical coefficient and making it possible to correlate these findings to the molecular polarizability of soft materials [67].

1.5 Outline of this Thesis

Chapter 2-Light propagation in optical fibers:

This chapter is devoted to a detailed approach to light propagation in optical fibers. In the following sections, the principles of modified total internal reflection and the theory of tapered optical fibers are elaborated. Modal solutions for cylindrical waveguides are derived from Maxwell's equations.

Chapter 3-Theoretical foundations of the Thesis topics:

The chapter presents the theoretical background of whispering gallery mode resonances in cylindrical symmetries and coordinates. In addition, the theory of mode coupling is introduced in this chapter. The sensing mechanisms of whispering gallery mode resonances are subsequently analyzed. In addition, the fundamental theory behind thermal poling is presented. A theoretical discussion of the strain-optic effect will be presented as a final step toward completing the analysis.

Chapter 4-Whispering gallery mode resonances in thermally poled borosilicate glass hetero-fibers:

The chapter presents the radially oriented thermal poling in borosilicate glass optical fibers and, afterward, the whispering gallery mode resonances in those optical hetero-fibers. A presentation is given on both the WGMs and the thermal poling apparatus. The findings are then broken down according to the types of anodes used (Nitrogen flow or not). Finally, the experimental results are compared with finite element analysis simulations (COMSOL Multiphysics).

Chapter 5-A study of silk fibroin photo-elasticity in whispering gallery modes cavities:

The chapter focuses on studying silk fibroin photo-elasticity within whispering gallery mode cavities. Each procedure and the experimental design are thoroughly examined to gain insights into the behavior of silk fibroin under mechanical stress and the consequent impact on its optical properties. The results of the experiments are presented in this chapter, followed by a detailed discussion of their implications and potential impact on the field of materials science.

Chapter 6-Thesis conclusions and future plans:

The final chapter of this thesis comprises the research conclusions and provides a comprehensive summary of the experimental projects. This research's findings will be presented clearly and concisely by analyzing the results obtained from the experiments. Moreover, this chapter will also discuss the implications of the research and its potential impact on the field of materials science. This chapter serves as a culmination of the research and provides a roadmap for future studies that can build upon the findings presented in this thesis.

2 Light propagation in optical fibers

In this chapter, light propagation phenomena in optical fibers are thoroughly investigated. The subsequent sections explain total internal reflection and the theoretical underpinnings of tapered optical fibers. In addition, a systematic derivation of modal solutions for cylindrical waveguides employing the fundamental principles embodied in Maxwell's equations is presented.

2.1 Single-mode optical fibers and their corresponding parameters

The single-mode optical fiber (SMF) is explicitly designed for propagating only a single mode of light, namely the transverse mode. In fiber-optics, modes are the solutions of the Helmholtz equation for waves, which is derived by combining Maxwell's equations and boundary conditions. These modes dictate how light waves propagate through space, determining their spatial distribution. However, waves may have the same mode but different frequencies; the single-mode fiber restricts the transmission of waves with different frequencies but with the same mode and spatial distribution. Optical fibers are made of pure silica glass created by fusing SiO_2 molecules, which allows for low-loss transmission and simple fabrication. The difference in refractive index between the core and the cladding is achieved through the selective use of dopants during fabrication. In fiber optics, doping refers to adding impurities to an optical fiber's core to alter its properties. Materials such as GeO_2 , Al_2O_3 , and P_2O_5 are commonly used as dopants in optical fibers because they raise the refractive index, allowing the total internal reflection to be utilized. The presence of these dopants can also alter the fiber's mechanical, thermal, and chemical properties, making it more suitable for specific applications. Among the three materials, GeO_2 is mainly known for enhancing the fiber's photosensitivity, allowing it to be used for

sensing and other related applications. In its basic configuration, an optical fiber consists of a central glass core with a high refractive index, a cladding layer whose refractive index is slightly lower than the core index, and an outer plastic polymeric jacket for adding mechanical durability (Fig. 2.1) [68].

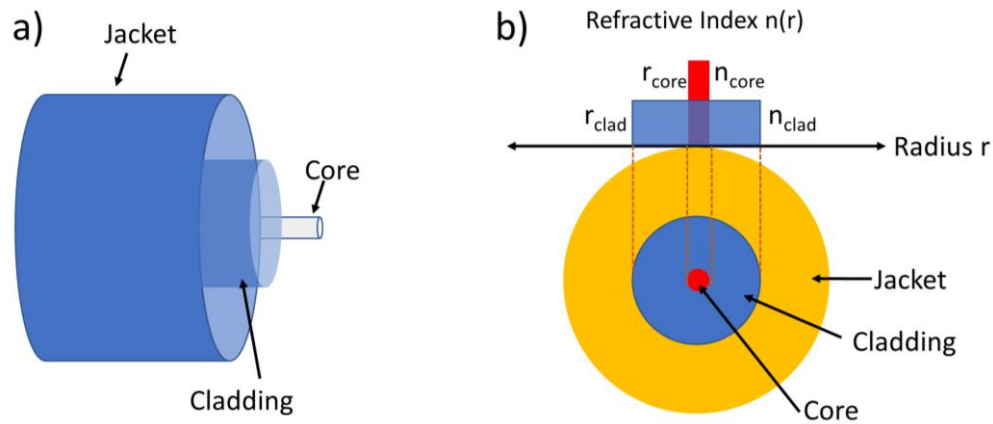


Figure 2.1 Illustration of a step-index fiber composed of a core, cladding, and polymeric plastic jacket (b) Figure depicting the cross-section of a step-index optical fiber and the refractive index profile.

The following are two fundamental parameters that can be used to characterize an optical fiber. The relative core-cladding refractive index difference, which is denoted by the symbol Δ and can be defined as [69]:

$$\Delta = \frac{n_{core} - n_{clad}}{n_{core}} \quad (2.1)$$

In addition to the so-called normalized frequency V , which is the parameter that determines the quality of guidance supported by the optical fiber and is defined as follows [70]:

$$V = k_0 r \sqrt{(n_{core}^2 - n_{clad}^2)} \quad (2.2)$$

Where $k_0=2\pi/\lambda$, r is the core radius, and λ is the wavelength of light. Only the lowest order mode (fundamental mode) propagates in the fiber for a step-index fiber if V is smaller than 2.405. Optical fibers designed to satisfy this condition are called single-mode fibers. A typical single-mode optical fiber for telecommunications has a core diameter of 8 μm and a cladding diameter of 125 μm . The core of this particular optical fiber has a refractive index of 1.447, while the cladding index is 1.444. However, it is only single-mode in the 1.5 μm IR band, and as the wavelength decreases below 1.2 μm , the V number exceeds 2.405, implying that the optical fiber is multimode. Multimode optical fibers are typically fibers with larger cores. A larger core allows multiple modes (or light rays) to travel down the core simultaneously. Similar to the single mode, the core is surrounded by a cladding that results in an overall diameter of 125 μm for the optical fiber.

2.2 Total internal reflection

Snell's law describes the refraction of an electromagnetic wave at the interface of two media with different refractive indices. Snell's formula is the following for two media with refractive indices n_1 and n_2 [71].

$$n_1 \sin \theta_1 = n_2 \sin \theta_2 \quad (2.3)$$

Where θ_1, θ_2 are the angles between the incident's wave vectors k_1 and k_2 and refracted light fields and the surface's normal vector (Fig. 2.2).

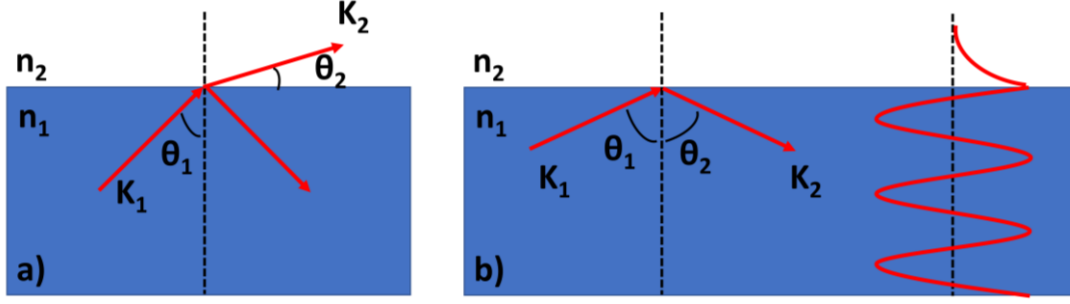


Figure 2.2 a) Reflection and refraction at an interface between two media with refractive indices n_1 and n_2 . The incident wave and the refracted wave vector are denoted by k_1 and k_2 , respectively. b) The interface completely reflects the light field for $n_2 < n_1$ and angles larger than the critical angle θ_c . A detailed analysis shows that the electromagnetic field decays exponentially beyond the interface. The penetration depth of this evanescent field into the optically thinner medium is typically on the order of the wavelength.

At an optically dense medium interface with an optically thinner medium, i.e., for $n_2 < n_1$, a refractive wave only exists for angles θ_1 smaller than the critical angle $\theta_c = \sin^{-1}(n_2/n_1)$. Otherwise, the incident wave is totally reflected from the interface, as shown in Fig. 2.2 b). The electric field in the optically thinner medium is treated as a scalar field of the form. In the case of total internal reflection, the electromagnetic field in the optically thinner medium will be examined in detail, following the analysis in [19], [20].

$$E_z = E_{0z} e^{i(k_2 \cdot r - \omega t)} \quad (2.4)$$

The wave vector \mathbf{k}_2 with an absolute value of $|\mathbf{k}_2| = n_2 \pi / \lambda_0$ can be split into a component \mathbf{k}_x that describes the propagation along with the interface and a component \mathbf{k}_y describing the propagation normal to the interface. Using Snell's law, a mathematical relationship can be found for $\mathbf{k}_y = \mathbf{k}_2 \cos(\theta_2)$.

$$k_y = k_2 \cdot \left(1 - \frac{n_1^2 \cdot \sin^2(\theta_1)}{n_2^2}\right)^{1/2} \quad (2.5)$$

If $\sin(\theta_1) > n_2/n_1$

$$k_y = ik_2 \cdot \left(\frac{n_1^2 \cdot \sin^2(\theta_1)}{n_2^2} - 1\right)^{1/2} = i\beta \quad (2.6)$$

becomes complex, while $k_x = (n_1 k_2 / n_2) \sin(\theta_1)$ is real. The electric field strength in the optically thinner medium is given by:

$$E_2 = E_{02} e^{-\beta y} e^{i(k_x x - \omega t)} \quad (2.7)$$

This so-called “evanescent field” exponentially decays with increasing distance y from the interface. Its penetration depth

$$\frac{1}{\beta} = \frac{\lambda_0}{2\pi \sqrt{n_1^2 \sin^2(\theta_1) - n_2^2}} \quad (2.8)$$

Light can be coupled to micro-resonators along d-shaped and ultra-thin tapered optical fibers via the evanescent field.

2.3 The optical fiber's numerical aperture

The light ray refracted at the air-core interface and then transmitted to the fiber's core is represented by the black light ray, denoted by the letter A in Figure 2.3. The light then travels through the optical fiber due to a phenomenon known as total internal reflection, which occurs between the core and cladding of the fiber.

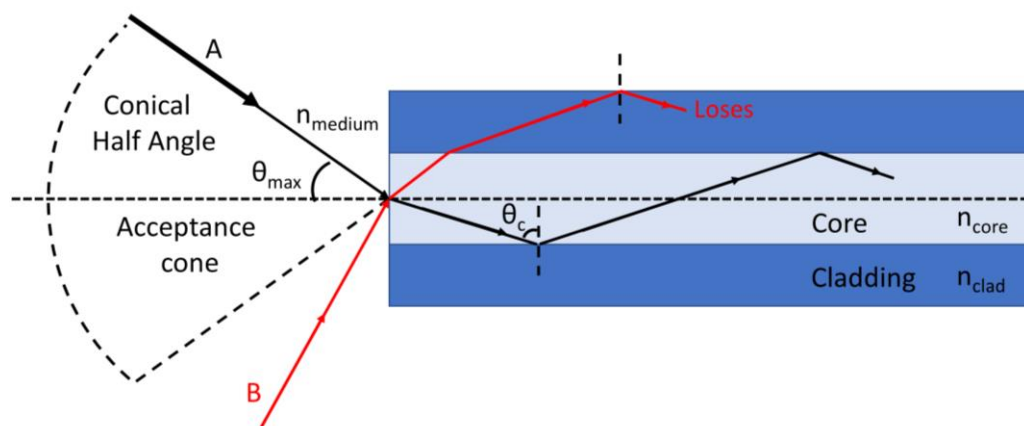


Figure 2.3 Total internal reflection in optical fiber and the acceptance angle of optical fiber are depicted schematically.

Rays that enter the optical fiber core at an angle greater than θ_{\max} concerning the fiber axis will have a fraction of their energy reflected. In contrast, the remaining amount of their energy will be transmitted out through the boundary in the direction of the cladding. Following a series of similar reflections, the energy contained within these rays will eventually be lost (see red-ray light noted as B). As a result, rays transmitted by total internal reflection within the fiber core must be incident on the acceptance cone. Therefore, θ_{\max} represents the maximum angle relative to the fiber axis at which light is permitted to enter the optical fiber for it to be propagated. This angle is also known as the conical half-angle or the total acceptance angle.

One must continue the ray theory analysis to obtain a relationship between the acceptance angle and the refractive indices of the three media involved: the core, the cladding, and the medium. Consequently, a more general term is the numerical aperture of the optical fiber (NA), which the following equation can define:

$$NA = n_{medium} \sin \theta_{max} = \sqrt{n_{core}^2 - n_{clad}^2} \quad (2.9)$$

The numerical aperture equation (2.9) conveniently measures an optical fiber's ability to collect light. It does not depend on the fiber core diameter and can be applied to core diameters as small as 8 μm . However, the geometric optics approach is insufficient when considering diameters of a smaller order. Therefore, electromagnetic mode theory has to be used in these situations.

2.4 Waveguide modes in standard optical fibers

Regarding the fiber optics field, the propagation of electromagnetic waves in cylindrically symmetric dielectric waveguides is fundamental. The theoretical background for optical fiber modal analysis is Maxwell's equations. Equations (2.10)-(2.13) provide the mathematical formula for defining electric and magnetic wave propagation through materials, further characterized by utilizing certain boundary conditions for optical fibers. The optical fiber dielectric material, usually glass, is isotropic, linear, and homogeneous, with no free charges or currents [72], [73]. Then the differential form of Maxwell equations for these becomes:

$$\nabla \times \mathbf{E} = -\frac{\partial \mathbf{B}}{\partial t} = -\mu \frac{\partial \mathbf{H}}{\partial t} \quad (2.10)$$

$$\nabla \times \mathbf{H} = \frac{\partial \mathbf{D}}{\partial t} = \varepsilon \frac{\partial \mathbf{E}}{\partial t} \quad (2.11)$$

$$\nabla \cdot \mathbf{D} = 0 \quad (2.12)$$

$$\nabla \cdot \mathbf{B} = 0 \quad (2.13)$$

The field quantities \mathbf{E} and \mathbf{H} in the above relations represent the electric and magnetic fields, respectively, as well as \mathbf{D} and \mathbf{B} , the electric and magnetic displacements defined by (2.14) and (2.15) :

$$\mathbf{B} = \mu \cdot \mathbf{H} \quad (2.14)$$

$$\mathbf{D} = \varepsilon \cdot \mathbf{E} \quad (2.15)$$

Applying the vector operator ($\nabla \times$) to equations 2.10 and 2.11, the homogenous form of the electromagnetic wave equation is described by (2.16) and (2.17):

$$(\nabla^2 - \mu\varepsilon \frac{\partial^2}{\partial t^2})\mathbf{E}(r, t) = 0 \quad (2.16)$$

$$(\nabla^2 - \mu\varepsilon \frac{\partial^2}{\partial t^2})\mathbf{H}(r, t) = 0 \quad (2.17)$$

The electromagnetic wave equation's solution defines energy propagation in the medium in consideration and is given by:

$$\mathbf{E}(r, t) = \mathbf{E}(r, \varphi) e^{i(\omega t - \beta z)} \quad (2.18)$$

$$\mathbf{H}(r, t) = \mathbf{H}(r, \varphi) e^{i(\omega t - \beta z)} \quad (2.19)$$

For propagation along the optical fiber axis (z-axis), each field vector component assumes the same z and t dependency of $e^{i(\omega t - \beta z)}$ [71].

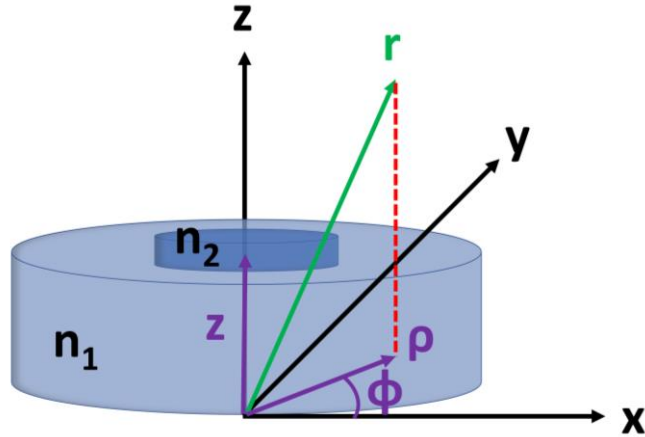


Figure 2.4 Cross-section of a standard optical fiber

A conventional optical fiber's cross-section (Fig. 2.4) is divided into two regions: the fiber's core, which has a refractive index of n_2 , and the cladding, which has a refractive index of n_1 , with $n_2 > n_1$ [73]. In addition to the infinite continuum of radiation modes that are not guided by the structure but are solutions to the boundary problem, dielectric waveguides support a finite number of guided modes [72]. A comprehensive analysis of guided modes in optical fibers is presented, starting with the time-independent wave equation in cylindrical coordinates (2.20a,b). The structural symmetry of optical fibers

allows the homogeneous wave equation to be fully separated into r and φ components. :

$$\left[\frac{\partial^2}{\partial r^2} + \frac{1}{r} \frac{\partial}{\partial r} + \frac{1}{r^2} \frac{\partial^2}{\partial \varphi^2} + (k^2 - \beta^2) \right] \mathbf{E}(r, \varphi) = 0 \quad (2.20a)$$

$$\left[\frac{\partial^2}{\partial r^2} + \frac{1}{r} \frac{\partial}{\partial r} + \frac{1}{r^2} \frac{\partial^2}{\partial \varphi^2} + (k^2 - \beta^2) \right] \mathbf{H}(r, \varphi) = 0 \quad (2.20b)$$

Where $k = \omega\sqrt{\mu\varepsilon} = \frac{\omega}{c} \sqrt{\frac{\varepsilon}{\varepsilon_0}} = k_0 n$ is the waveguide number and $n = \sqrt{\frac{\varepsilon}{\varepsilon_0}}$ is the refractive index of the dielectric medium. Maxwell's curl equations written in terms of the cylindrical components are given by:

$$i\omega\varepsilon E_r = i\beta H_\varphi + \frac{1}{r} \frac{\partial H_z}{\partial \varphi} \quad (2.21a)$$

$$i\omega\varepsilon E_\varphi = -i\beta H_r - \frac{\partial H_z}{\partial r} \quad (2.21b)$$

$$-i\omega\mu H_r = i\beta E_\varphi + \frac{1}{r} \frac{\partial E_z}{\partial \varphi} \quad (2.21c)$$

$$-i\omega\mu H_\varphi = -i\beta E_r - \frac{\partial E_z}{\partial r} \quad (2.21d)$$

The field components E_r , E_ϕ , E_z , H_r , H_ϕ , H_z are:

$$E_r = \frac{-i\beta}{k^2 - \beta^2} \left(\frac{\partial}{\partial r} E_z + \frac{\omega\mu}{\beta} \frac{1}{r} \frac{\partial}{\partial \phi} H_z \right) \quad (2.22a)$$

$$E_\phi = \frac{-i\beta}{k^2 - \beta^2} \left(\frac{1}{r} \frac{\partial}{\partial \phi} E_z - \frac{\omega\mu}{\beta} \frac{\partial}{\partial r} H_z \right) \quad (2.22b)$$

$$H_r = \frac{-i\beta}{k^2 - \beta^2} \left(\frac{\partial}{\partial r} H_z - \frac{\omega\varepsilon}{\beta} \frac{1}{r} \frac{\partial}{\partial \phi} E_z \right) \quad (2.22c)$$

$$H_\phi = \frac{-i\beta}{k^2 - \beta^2} \left(\frac{1}{r} \frac{\partial}{\partial \phi} H_z + \frac{\omega\varepsilon}{\beta} \frac{\partial}{\partial r} E_z \right) \quad (2.22d)$$

The E_z and H_z components must be determined according to the given relations to specify the wave solution uniquely [71], [74]. Time-independent wave equation E_z and H_z in cylindrical coordinates have taken the form:

$$\left[\frac{\partial^2}{\partial r^2} + \frac{1}{r} \frac{\partial}{\partial r} + \frac{1}{r^2} \frac{\partial^2}{\partial \phi^2} + (k^2 - \beta^2) \right] \begin{bmatrix} E_z \\ H_z \end{bmatrix} = 0 \quad (2.23)$$

The longitudinal components E_z and H_z are used to derive the simplified guided modes of the optical fiber. The solutions to the partial differential equations (2.20a,b), which are separable, are described by [72]:

$$E_z(r, \varphi) = AR(r)\Phi(\varphi) \quad (2.24a)$$

$$H_z(r, \varphi) = AR(r)\Phi(\varphi) \quad (2.24b)$$

Where $\Phi(\varphi) = Ae^{\pm il\varphi}$ so that:

$$E_z(r, \varphi) = R(r)e^{\pm il\varphi} \quad (2.25a)$$

$$H_z(r, \varphi) = R(r)e^{\pm il\varphi} \quad (2.25b)$$

Where $l=0,1,2,\dots$, E_z and H_z are hence single-valued functions of φ . As a result, equations (2.20a,b) and (2.25a,b) generate equation (2.26), also known as Bessel's differential equation [71], [72]:

$$\left[\frac{\partial^2}{\partial r^2} + \frac{1}{r} \frac{\partial}{\partial r} + \left(k^2 - \beta^2 - \frac{l^2}{r^2} \right) \right] R(r) = 0 \quad (2.26)$$

The generic solution of the Bessel function is (2.27) divided into:

$$R(r) = \begin{cases} c_1 J_l(hr) + c_2 Y_l(hr), & \text{for } h^2 = k^2 - \beta^2 > 0 \\ c_1 I_l(hr) + c_2 K_l(hr), & \text{for } -q^2 = k^2 - \beta^2 < 0 \end{cases} \quad (2.27)$$

Appropriate cylindrical function solutions of the Bessel equation must be determined to generate optimal field configurations in an optical fiber while meeting the physical limitations. A Bessel function $J_l(hr)$ is utilized because the

electric and magnetic fields must be finite at the center of the optical fiber core, $r=0$. The field components in this case ($r < a$) are given by:

$$E_z(r, \varphi) = A J_l(hr) e^{il\varphi} \quad (2.28a)$$

$$H_z(r, \varphi) = B J_l(hr) e^{il\varphi} \quad (2.28b)$$

On the other hand, the fields in the cladding of the optical fiber diminish in an exponential form of $e^{-\gamma r}$. The decaying behavior of the electric and magnetic fields in the cladding ($r > a$) is described using a modified form of the Bessel $K_l(qr)$ function.

$$E_z(r, \varphi) = C K_l(hr) e^{-il\varphi} \quad (2.29a)$$

$$H_z(r, \varphi) = D K_l(hr) e^{-il\varphi} \quad (2.29b)$$

The unknown constants A, B, C, and D can be determined using the boundary conditions and field components. In the case that $l \neq 0$, the solutions correspond to the hybrid modes $HE_{m,l}$ and $EH_{l,m}$, which have non-zero electric and magnetic field components. We derive the following set of equations for the transverse field components for hybrid mode propagation by replacing the equations (2.28 a), (2.28 b) and (2.29 a), (2.29 b) with equations (2.30 a) - (2.30 d) for the electric and magnetic field components:

$$E_r(r, t) = \begin{cases} -i \frac{\beta}{h^2} \left[A h J'_l(hr) + i \frac{\omega \mu l}{\beta r} B J_l(hr) \right] (r < a) \\ i \frac{\beta}{q^2} \left[C q K'_l(qr) + i \frac{\omega \mu l}{\beta r} D K_l(qr) \right] (r > a) \end{cases} \times e^{il\varphi} e^{i(\omega t - \beta z)} \quad (2.30a)$$

$$E_{\varphi}(\mathbf{r}, t) = \begin{cases} -i \frac{\beta}{h^2} \left[\frac{il}{r} A h J_l(hr) - i \frac{\omega\mu}{\beta} B J_l'(hr) \right] (r < a) \\ i \frac{\beta}{q^2} \left[\frac{il}{r} C K_l(qr) - i \frac{\omega\mu}{\beta} D q K_l'(qr) \right] (r > a) \end{cases} \times e^{il\varphi} e^{i(\omega t - \beta z)} \quad (2.30b)$$

$$H_r(\mathbf{r}, t) = \begin{cases} -i \frac{\beta}{h^2} \left[B h J_l'(hr) + i \frac{\omega\varepsilon_1 l}{\beta r} A J_l(hr) \right] (r < a) \\ i \frac{\beta}{q^2} \left[D q K_l'(qr) + i \frac{\omega\varepsilon_2 l}{\beta r} C K_l(qr) \right] (r > a) \end{cases} \times e^{il\varphi} e^{i(\omega t - \beta z)} \quad (2.30c)$$

$$H_{\varphi}(\mathbf{r}, t) = \begin{cases} -i \frac{\beta}{h^2} \left[\frac{il}{r} B h J_l(hr) - i \frac{\omega\varepsilon_1}{\beta} A J_l'(hr) \right] (r < a) \\ i \frac{\beta}{q^2} \left[\frac{il}{r} D K_l(qr) - i \frac{\omega\varepsilon_2}{\beta} C q K_l'(qr) \right] (r > a) \end{cases} \times e^{il\varphi} e^{i(\omega t - \beta z)} \quad (2.30d)$$

The following equations are derived by combining equations (2.30 a) – (2.30 d) and the continuity equation of the electric and magnetic field components E_{φ} , E_z , H_{φ} , and H_z at the interface between the core and the cladding ($r=a$):

$$J_l(ha)A - K_l(qa)C = 0 \quad (2.31a)$$

$$\left[i \frac{l}{h^2 a} J_l(ha) \right] A + \left[-\frac{\omega\mu}{h\beta} J_l'(ha) \right] B + \left[i \frac{l}{q^2 a} K_l(qa) \right] C + \left[-\frac{\omega\mu}{h\beta} J_l'(ha) \right] B = 0 \quad (2.31b)$$

$$J_l(ha)B - K_l(qa)D = 0 \quad (2.31c)$$

$$\left[\frac{\omega\varepsilon_1}{h^2 \beta} J_l'(ha) \right] A + \left[i \frac{l}{h^2 a} J_l(ha) \right] B + \left[\frac{\omega\varepsilon_2}{q\beta} K_l'(qa) \right] C + \left[i \frac{l}{q^2 a} K_l(qa) \right] D = 0 \quad (2.31d)$$

Solving the previous set of equations will determine the relationship between the coefficients A, B, C, and D. The following conditions must be fulfilled to achieve wave guidance via the optical fiber core:

$$h^2 = k_o^2 n_1^2 - \beta^2 > 0, \quad 0 < r < a \quad (2.32a)$$

$$-q^2 = k_o^2 n_2^2 - \beta^2 < 0, \quad r > a \quad (2.32b)$$

The radius of the fiber core is denoted by a . Because the parameters $h = \sqrt{k_o^2(n_1^2 - n_2^2) - q^2}$ and $q = \sqrt{k_o^2(n_1^2 - n_2^2) - h^2}$ are real, positive numbers, $0 < (h, q) \leq k_o^2(n_1^2 - n_2^2)$ is evident. In the general solution (2.27), Bessel functions Y_l and I_l are rejected because they tend to infinity for $r \rightarrow 0$ and $r \rightarrow \infty$, respectively. Acceptable solutions for the E_z , H_z components have the general form:

$$E_z(\mathbf{r}, t) = \begin{cases} A J_l(hr) \\ C K_l(qr) \end{cases} \times e^{il\phi} e^{i(\omega t - \beta z)}, \quad \begin{matrix} r < a \\ r > a \end{matrix} \quad (2.33a)$$

$$H_z(\mathbf{r}, t) = \begin{cases} B J_l(hr) \\ D K_l(qr) \end{cases} \times e^{il\phi} e^{i(\omega t - \beta z)}, \quad \begin{matrix} r < a \\ r > a \end{matrix} \quad (2.33b)$$

Where $l=0, \pm 1, \pm 2, \dots$ and A, B, C, D are coefficients determined by the boundary conditions. When $E_z=0$ and $E_\phi, H_r, H_z \neq 0$, the solutions correspond to transverse electric, $TE_{0,m}$ modes, and when $H_z=0$ and $E_r, E_z, H_\phi \neq 0$, the solutions correspond to transverse magnetic $TM_{0,m}$ modes. Considerable simplification arises in the weakly guiding approximation, $n_1 - n_2 \ll 1$.













LP mode Designations	Traditional mode Designations	Electric field Distribution	Intensity Distribution of E_z
$LP_{11} \begin{cases} l = 0 \\ m = 1 \end{cases}$	$HE_{11} \begin{cases} l = 0 \\ m = 1 \end{cases}$		
$LP_{01} \begin{cases} l = 1 \\ m = 1 \end{cases}$	$\begin{cases} TE_{01} \begin{cases} l = 0 \\ m = 1 \end{cases} \\ TM_{01} \begin{cases} l = 0 \\ m = 1 \end{cases} \\ HE_{21} \begin{cases} l = 1 \\ m = 1 \end{cases} \end{cases}$	  	  
$LP_{21} \begin{cases} l = 2 \\ m = 1 \end{cases}$	$\begin{cases} HE_{11} \begin{cases} l = 2 \\ m = 1 \end{cases} \\ HE_{21} \begin{cases} l = 2 \\ m = 1 \end{cases} \end{cases}$	 	 

Figure 2.5 Correlation between the electric field vectors and intensity profiles of the three first $LP_{l,m}$ modes, and conventional modes [8]

The Linearly Polarized modes are formed by the linear superposition of $HE_{l+1,m}$, and $EH_{l-1,m}$ modes, as shown in Figure 2.5. Extensive calculations using Bessel equations and boundary conditions for optical fiber geometry result in overlapping between the basic modes. Moreover, Figure 2.6 estimates the cut-off wavelength of each mode in a visual format.

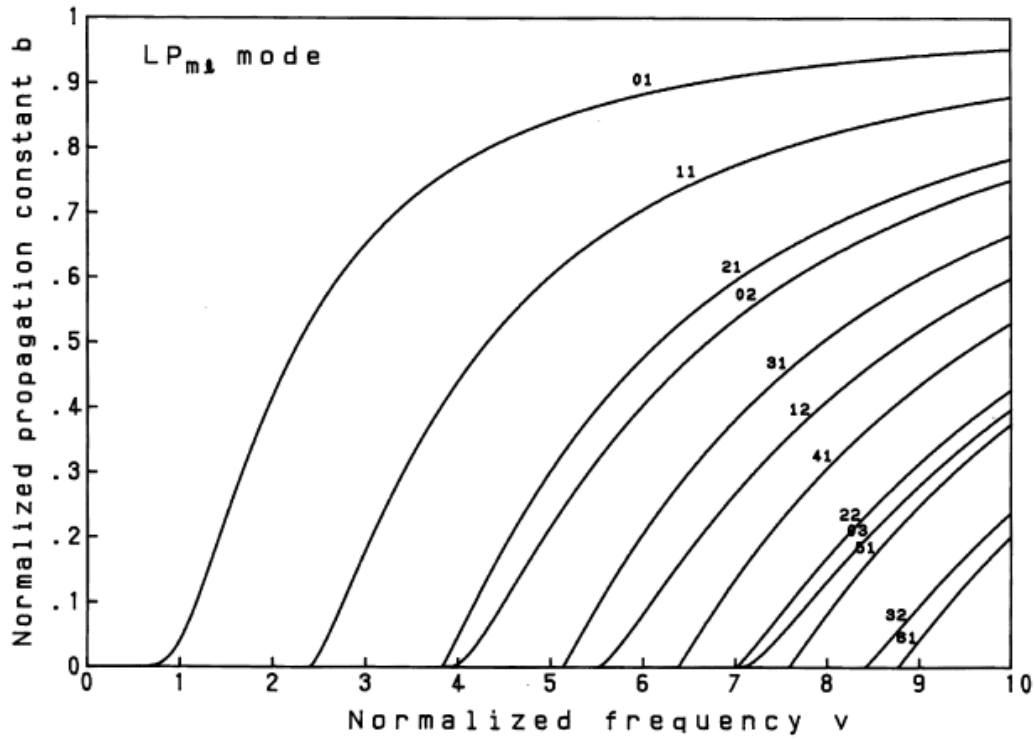


Figure 2.6 LP mode dispersion curves in step-index fibers [3]

The normalized propagation constant b as a function of normalized frequency V for guided modes of standard optical fiber is depicted in the diagram above. The number pairs written on each curve give the l and m of the $LP_{l,m}$ modes. The equation (2.34) yield the value of b [72].

$$b = \frac{\left(\frac{\beta}{n_2 k} - 1\right)}{\frac{n_1}{n_2} - 1} \quad (2.34)$$

As shown in figure 2.6, the normalized cut-off frequency for the first higher mode $LP_{1,1}$ is $V=2.405$. The condition $V<2.405$ is required for single-mode propagation of the fundamental mode $LP_{0,1}$.

2.5 Tapered optical fibers

As previously mentioned, the V-number cut-off dictates the restricted transmission of higher-order modes. On the other hand, optical fiber structures can be multi-modal in various opto-geometrical designs. An example of multi-modal optical fibers is the optical fiber tapers (OFT). An OFT is a thinned optical fiber with a geometric gradient segment where the mode propagates in the cladding at a specific point by a modal transformation. A typical optical fiber can be heated to its softening point and subjected to tensile force to produce an OFT [75]. Optical fibers are tapered using advanced glass processors (Fig. 2.7).

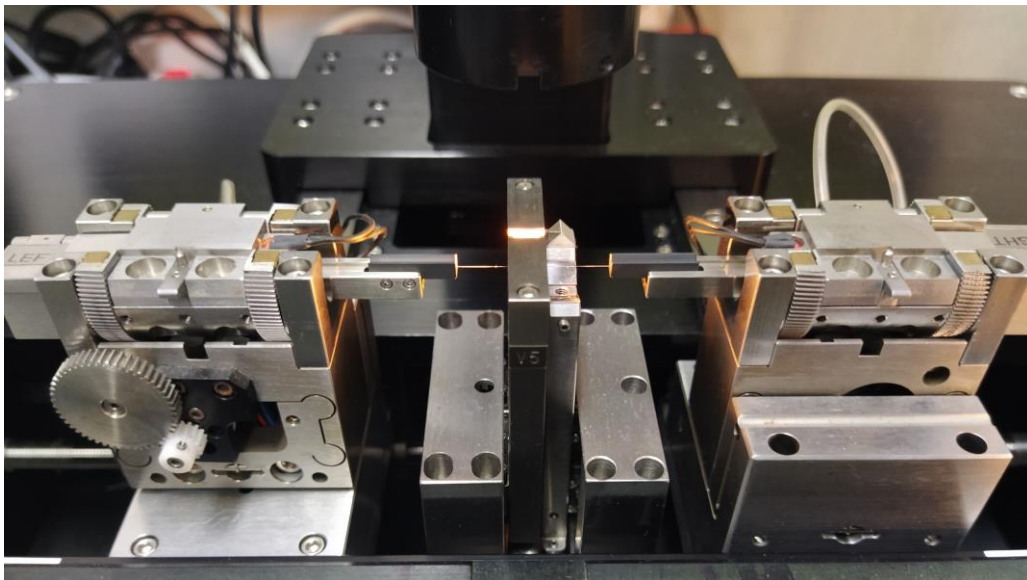


Figure 2.7 Vytran GPX-3000 glass fiber processor for thermally tapering down the optical fibers

The optical fiber taper is separated into three primary regions (Fig. 2.8) after the heat-and-pull technique: the untapered part, the taper transition, and the taper waist, the region with the largest decreased diameter of the tapered optical fiber.

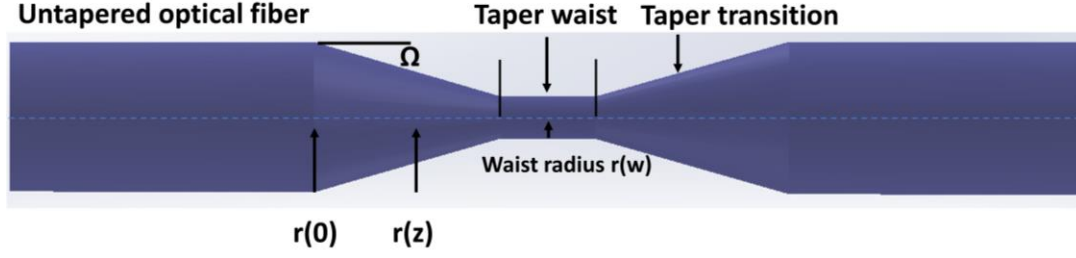


Figure 2.8 The primary sections of a tapered optical fiber are depicted schematically.

Subsequently, the fundamental mode's field distribution shifts as the optical fiber are tapered. The energy transfer from the fundamental mode to the closest higher-order modes varies depending on the diameter change rate [75], [76]. For a given wavelength and core-cladding refractive index difference, a core radius exists at which light has escaped the core and is guided by the interface between the cladding and the external medium surrounding the optical fiber. This specific point is called taper transition, and the effective refractive index of the fundamental mode is equal to the refractive index of the cladding. The optical fiber is no longer single-mode beyond the tapered transition region, and higher-order modes can be coupled. The fundamental mode LP_{01} can only couple to higher-order modes with the exact azimuthal symmetry, $LP_{0,m}$ modes, providing the axially symmetric taper [76].

Straightforwardly, we may deduce that mode coupling inside a taper is inversely proportional to the taper geometry. The adiabaticity criterion for tapered optical fibers is then introduced to determine the mode propagation parameters in the taper [77]. A tapered fiber is adiabatic if most energy is coupled into the fundamental mode and does not couple into higher-order modes throughout its propagation [77], [78]. By connecting the length associated with the tapering angle at the local core radius (z_t) with the beating length between two modes, the adiabaticity criterion may be derived (z_b). The adiabaticity condition is provided by the inequality (2.35), which states that the beat length between the fundamental and first higher-order mode must be less than the local taper length [77], [78].

$$z_b < z_t \quad (2.35)$$

$$z_b = \frac{2\pi}{\beta_1 - \beta_2} \quad (2.36)$$

where β_1 denotes the basic mode propagation constant at radius r and β_2 denotes the first excited mode propagation constant at radius r , and the local taper length is represented by :

$$z_t = \frac{\rho}{\tan\Omega} \quad (2.37)$$

Where Ω is the angle formed by the tangent to the core-cladding contact and the z -axis of the fiber. We can calculate using the above formulas and the rate of change of the local core radius:

$$\tan\Omega = \frac{d\rho}{dz} \quad (2.38)$$

The adiabaticity criterion can be defined as follows:

$$\left| \frac{d\rho}{dz} \right| < \frac{\rho}{z_b} = \frac{\rho(\beta_1 - \beta_2)}{2\pi} \quad (2.39)$$

In terms of the local cladding radius r_z , it is as follows:

$$\left| \frac{dr}{dz} \right| < \frac{r}{z_b} = \frac{r(\beta_1 - \beta_2)}{2\pi} \quad (2.40)$$

According to Equations 2.39 and 2.40, the taper must be gradual enough to prevent coupling from the fundamental to higher-order modes. Otherwise, the mode evolution will be non-adiabatic if the taper angle is too steep, increasing the higher-order mode excitation [78].

2.6 Summary

The chapter at hand offers an exhaustive exploration into how light travels within optical fibers, delving into pivotal concepts such as total internal reflection, which is fundamental to the functioning of fiber optics. It sheds light on the theory behind tapered optical fibers, elucidating their operational mechanisms. The chapter further presents a systematically derived set of modal solutions pertinent to cylindrical waveguides, all underpinned by fundamental Maxwell's equations. This chapter is a deep dive into light propagation's nuances and core principles within optical fibers, revealing its complexities and foundational aspects.

3 Theoretical foundations of this Thesis topics

In this chapter, we embark on a comprehensive exploration of the theoretical underpinnings of three salient topics. We will delve into the theory of whispering gallery modes, which has captured the attention of researchers due to its diverse applications in optical resonators. Furthermore, we shall examine the principles of thermal poling, elucidating the mechanisms that underlie this technique's ability to change the optical properties of glasses. Lastly, we will probe the theoretical background of photoelasticity, a phenomenon that has found immense value in stress analysis and material characterization. As we venture through these interconnected themes, we aim to provide a robust foundation for understanding each domain's scientific principles and intricacies.

3.1 Whispering gallery modes (WGMs) theory

3.1.1 Whispering gallery modes

Whispering gallery mode (WGM) resonators are a distinct class of optical resonators that have attracted considerable interest due to their exceptional properties. In these resonators, waves travel along a curved path and are confined by total internal reflection, resulting in high-Q resonances with small mode volumes and extended lifetimes. WGM resonators have been demonstrated in various geometries, such as spheres, toroids, and disks, and can support a broad spectrum of electromagnetic modes. The resonant frequencies and quality factors of WGM resonators can be modified by adjusting the resonator's geometry and composition. Losses through the surface are included in a wave description, and as a result, in the absence of external excitation, the mode's amplitude decreases

[79]. Despite their maturity as a platform technology, these resonators attract significant research into new applications, improved fabrication, and theoretical concerns. In terms of spectral appearance, the power stored in a WGM, $P(\omega)$, has a Lorentzian lineshape defined by

$$P(\omega) = P_0 \frac{\frac{\gamma_0^2}{2}}{(\omega - \omega_0)^2 + \frac{\gamma_0^2}{2}} \quad (3.1)$$

Therefore, the principal parameters describing the WGM resonance are its resonance frequency ω_0 , full-width at half maximum (FWHM) γ_0 , and amplitude P_0 . Quality factor Q applies to this resonator type and can be expressed in wavelength $Q = \lambda_0 / \Delta\lambda$. Because the energy is contained within the cavity, direct observation of $P(\omega)$ is generally impossible. Excitation of WGMs must instead be inferred experimentally through indirect means. The monitoring of the excitation channel is a typical method. It is possible to obtain evanescent coupling to WGMs by bringing an adiabatically tapered optical fiber close to the resonator surface [80], [81]. A typical Lorentzian resonance dip can be noticed by monitoring the transmitted power $P_t(\omega)$ of the excitation light launched into the fiber as the frequency of incident light is tuned (Fig. 3.1). The achieved coupling efficiency β then determines the depth of the observed transmission dip, $P_t(\omega) = P_0 - \beta P(\omega)$, where P_0 is the input laser power.

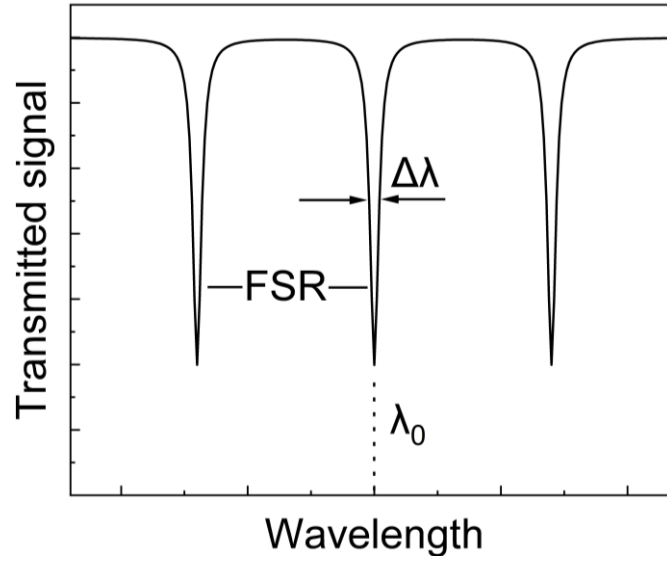


Figure 3.1 WGMs resonance spectrum of a cavity resonator. The individual peaks of FWHM $\Delta\lambda$, corresponding to the resonator modes, are separated by the free spectral range FSR.

Radiation, surface scattering, bulk scattering, and material absorption are loss mechanisms contributing to the total resonance linewidth [82], [83]. Accordingly, the FWHM of the WGM resonance can be written in the form:

$\Delta\lambda = \Delta\lambda_{\text{rad}} + \Delta\lambda_{\text{sca}} + \Delta\lambda_{\text{mat}} + \dots$, or equivalently $Q_0^{-1} = Q_{\text{rad}}^{-1} + Q_{\text{sca}}^{-1} + Q_{\text{mat}}^{-1} + \dots$. The resonator size, inherent material qualities, and manufacturing quality determine the relative importance of each contribution. Radiative losses dominate small resonators, but absorption losses in the host medium become increasingly crucial as the resonator size grows. The WGM gets more confined within the cavity as the size expands, and the material properties of the cavity dictate the final, ultimate, material limited Q , given by $Q_{\text{abs}} = 2\pi n / \alpha \lambda$ where n_r is the refractive index of the resonator, with associated absorption coefficient α [4].

3.1.2 Wave equation for cylindrical resonators

The WGM's guiding mechanism in a microresonator's azimuthal direction (MR) is total internal reflection, similar to axial propagation in conventional waveguides. When the guided wave travels along the MR's perimeter, resonance occurs since the wave drives itself coherently by returning in phase after each revolution. In this manner, the wave continuously follows the surface of the MR as it travels in a circle around it. The optical path in a circumnavigation must equal an integer multiple of the optical wavelength, denoted by λ . When this condition is satisfied, resonances and several discrete modes will manifest at various wavelengths [84]. The resonant condition can be written as [85]:

$$\lambda_R = \frac{2\pi a n_{eff}}{m} \quad (3.2)$$

Where λ_R is the resonant wavelength, a is the radius of the MR, n_{eff} is the effective index of the WGM, and m is the azimuthal order of the mode (i.e., is the total number of different wavelengths around the MR).

The MR can be subdivided into two regions. Region I consists of an infinitely long dielectric rod with anisotropic permittivity, $\epsilon_0\epsilon_1$. In contrast, region II surrounding the MR comprises an infinite dielectric medium (typically air) with an isotropic permittivity of $\epsilon_0\epsilon_2$. Both media are homogeneous, source-free, lossless, and have a μ_0 magnetic permeability. Because of the geometry involved, it is necessary to use a cylindrical coordinate system to solve this problem. Solving Maxwell's equations in the two distinct regions and applying the appropriate boundary conditions makes it possible to solve the problem of WGMs propagating in cylindrical MRs. The direction in which the signal is transmitted is entirely azimuthal. Therefore, the dependence of the electric E field and the magnetic H field as a coordinate function can be described as $e^{-j\beta\phi}$, where β is the propagation constant of the modes. In addition, a harmonic time

dependence of the fields is considered. This is denoted by the notation $e^{j\omega t}$, where ω is the angular frequency. The electromagnetic field can be written as:

$$\begin{aligned} \mathbf{E}(\mathbf{r}, t) &= \mathbf{e}(\rho) e^{-j\beta\varphi} e^{j\omega t} \\ \mathbf{H}(\mathbf{r}, t) &= \mathbf{h}(\rho) e^{-j\beta\varphi} e^{j\omega t} \end{aligned} \quad (3.3)$$

Where

$$\begin{aligned} \mathbf{e}(\rho) &= e_\rho(\rho) \hat{\mathbf{u}}_\rho + e_\varphi(\rho) \hat{\mathbf{u}}_\varphi + e_z(\rho) \hat{\mathbf{u}}_z \\ \mathbf{h}(\rho) &= h_\rho(\rho) \hat{\mathbf{u}}_\rho + h_\varphi(\rho) \hat{\mathbf{u}}_\varphi + h_z(\rho) \hat{\mathbf{u}}_z \end{aligned} \quad (3.4)$$

According to Eqs. (3.4), the electromagnetic field's amplitude only depends on the coordinate r . The electromagnetic field will not show any dependence on the z coordinate because it is assumed that the length of the cylinder is infinite, and there is also symmetry in the translational direction. Solving Maxwell's equations for the fields described in Eqs 3.3 is necessary to obtain the WGMs guided by the MR.

The expression of the tensor varies depending on the material or effect that induces anisotropy. Here, we will consider a uniaxial medium because the response of WGMs to the experiments described in subsequent chapters can be theoretically derived from this anisotropy. Two of the tensor's diagonal elements are the same, while the other diagonal element is unique and can be expressed in the following way:

$$\bar{\varepsilon} = \begin{pmatrix} \varepsilon_t & & \\ & \varepsilon_t & \\ & & \varepsilon_z \end{pmatrix}; \quad \left\{ \begin{array}{l} \varepsilon_t: \text{transversal to the } z \text{ coordinate} \\ \varepsilon_z: \text{parallel to the } z \text{ coordinate} \end{array} \right. \quad (3.5)$$

The wave equations for the electric and magnetic fields can be obtained by expanding Maxwell's equations with the expression of the fields and the permittivity tensor, as follows:

$$\begin{aligned}\nabla \times (\nabla \times \mathbf{E}) &= \omega^2 \mu_0 \varepsilon_0 \bar{\varepsilon} \mathbf{E} \\ \nabla \times (\bar{\varepsilon}^{-1} \nabla \times \mathbf{H}) &= \omega^2 \mu_0 \varepsilon_0 \mathbf{H}\end{aligned}\tag{3.6}$$

The wave equations for the axial components can be written as follows:

$$\begin{aligned}[\rho^2 \partial_\rho^2 + \rho \partial_\rho + (\rho^2 k_0^2 \varepsilon_z - \beta_\varphi)] \varepsilon_z(\rho) &= 0 \\ [\rho^2 \partial_\rho^2 + \rho \partial_\rho + (\rho^2 k_0^2 \varepsilon_t - \beta_\varphi)] h_z(\rho) &= 0\end{aligned}\tag{3.7}$$

The wavenumber in a vacuum is denoted as k_0 . Both differential equations can be represented as what is known as Bessel equations due to their identical form. Before applying boundary conditions at the interface between the two media, we study the conditions the propagation constant, β_φ , must fulfill to have WGM resonances. This is done so that boundary conditions can be applied at the interface. It is necessary to have constructive interference to observe a WGM resonance. WGMs travel in an azimuthal direction during their transmission, which causes the confined wave to interfere with itself after completing one entire circuit. To have constructive interference, the phase of the confined wave must be the same with a difference that is a multiple of 2π after each round trip. In the alternative scenario, the loaded energy of the resonator is in the same order as the energy lost by radiation; consequently, the resonances do not appear. According to their polarization, the guided modes can be categorized into groups within an axial waveguide. The modes supported by a dielectric waveguide can be divided into three categories: hybrid modes, TE modes, and TM modes [72]. Even though WGMs propagate in the azimuthal direction, the classical notation

where the fields are perpendicular to the axial direction is maintained. Moreover, hybrid modes with pure azimuthal propagation cannot exist in the case of isotropic dielectric cylinders [86]. As a result, the WGMs can be divided into two distinct families: the TE and the TM.

TM Modes

Region I ($\rho < a$):

$$\begin{aligned}
 E_z^I &= A_1 J_m(k_0 n_z \rho) e^{-jm\varphi} e^{i\omega t} \\
 H_\rho^I &= \frac{m}{\omega \mu_0} \frac{1}{\rho} A_1 J_m(k_0 n_z \rho) e^{-jm\varphi} e^{i\omega t} \\
 H_\varphi^I &= \frac{k_0 n_z}{j\omega \mu_0} A_1 J'_m(k_0 n_z \rho) e^{-jm\varphi} e^{i\omega t} \\
 E_\rho^I &= E_\varphi^I = H_z^I = 0
 \end{aligned} \tag{3.8}$$

Region II ($\rho > a$):

$$\begin{aligned}
 E_z^{II} &= A_2 H_m^{(2)}(k_0 n_2 \rho) e^{-jm\varphi} e^{i\omega t} \\
 H_\rho^{II} &= \frac{m}{\omega \mu_0} \frac{1}{\rho} A_2 H_m^{(2)}(k_0 n_2 \rho) e^{-jm\varphi} e^{i\omega t} \\
 H_\varphi^{II} &= \frac{k_0 n_2}{j\omega \mu_0} A_2 H_m^{(2)'}(k_0 n_2 \rho) e^{-jm\varphi} e^{i\omega t} \\
 E_\rho^{II} &= E_\varphi^{II} = H_z^{II} = 0
 \end{aligned} \tag{3.9}$$

TE Modes

Region I ($\rho < a$):

$$\begin{aligned}
 H_z^I &= B_1 J_m(k_0 n_t \rho) e^{-jm\varphi} e^{i\omega t} \\
 E_\rho^I &= -\frac{m}{\omega \varepsilon_0 \varepsilon_t} \frac{1}{\rho} B_1 J_m(k_0 n_t \rho) e^{-jm\varphi} e^{i\omega t} \\
 E_\varphi^I &= -\frac{k_0 n_t}{j\omega \varepsilon_0 \varepsilon_t} B_1 J'_m(k_0 n_t \rho) e^{-jm\varphi} e^{i\omega t} \\
 H_\rho^I &= H_\varphi^I = E_z^I = 0
 \end{aligned} \tag{3.2}$$

Region II ($\rho > a$):

$$\begin{aligned}
 H_z^{II} &= B_2 H_m^{(2)}(k_0 n_2 \rho) e^{-jm\varphi} e^{i\omega t} \\
 E_\rho^{II} &= -\frac{m}{\omega \varepsilon_0 \varepsilon_2} \frac{1}{\rho} B_2 H_m^{(2)}(k_0 n_2 \rho) e^{-jm\varphi} e^{i\omega t} \\
 E_\varphi^{II} &= -\frac{k_0 n_2}{j\omega \varepsilon_0 \varepsilon_2} B_2 H_m^{(2)'}(k_0 n_2 \rho) e^{-jm\varphi} e^{i\omega t} \\
 H_\rho^{II} &= H_\varphi^{II} = E_z^{II} = 0
 \end{aligned} \tag{3.11}$$

J_m and H_m are the derivative of the Bessel function of the first kind and the Hankel function of the second kind, respectively. After the fields have been acquired, boundary conditions are implemented to ensure the continuity of the tangential components of the electromagnetic field at the interface ($\rho = a$):

$$\begin{aligned}
 \text{TM: } E_z^I(\rho = a) &= E_z^{II}(\rho = a); & H_\varphi^I(\rho = a) &= H_\varphi^{II}(\rho = a); \\
 \text{TE: } H_z^I(\rho = a) &= H_z^{II}(\rho = a); & E_\varphi^I(\rho = a) &= E_\varphi^{II}(\rho = a);
 \end{aligned} \tag{3.12}$$

These conditions lead to two equations with two unknown variables for each polarization state, A_i and B_i 's constants. If the determinant vanishes, there are only nontrivial solutions to the 2x2 equation system. Consequently, the characteristic equations for TM and TE modes are as follows:

$$\begin{aligned}
 TM: n_z \frac{J'_m(k_0 n_z a)}{J_m(k_0 n_z a)} &= n_2 \frac{H_m^{(2)'}(k_0 n_2 a)}{H_m^{(2)}(k_0 n_2 a)} \\
 TE: \frac{1}{n_t} \frac{J'_m(k_0 n_z a)}{J_m(k_0 n_z a)} &= \frac{1}{n_2} \frac{H_m^{(2)'}(k_0 n_2 a)}{H_m^{(2)}(k_0 n_2 a)}
 \end{aligned} \tag{3.13}$$

The refractive indices n_z refer to the refractive index parallel to the z coordinate and n_t transversal. The left-hand side term in both characteristic equations is defined by the Bessel function J_m and its derivative, while the right-hand side term is determined by the Hankel function $H_m^{(2)}$ and its derivative.

3.1.3 Tapered optical fiber-microresonator coupling

It is essential to achieve an effective and efficient coupling to observe high-Q WGM resonances. Several methods can be used to couple light from a waveguide structure to a resonator, which has both advantages and disadvantages. This chapter will examine a theoretical approach employing microfiber to couple the energy into the micro-resonator. The system comprises an input field, denoted by E_i , coupled with a micro-resonator guided through the microfiber. The symbol η indicates the coupling strength between the cavity and the waveguide. It is determined by the degree to which the microfiber and the micro-resonator fields overlap.

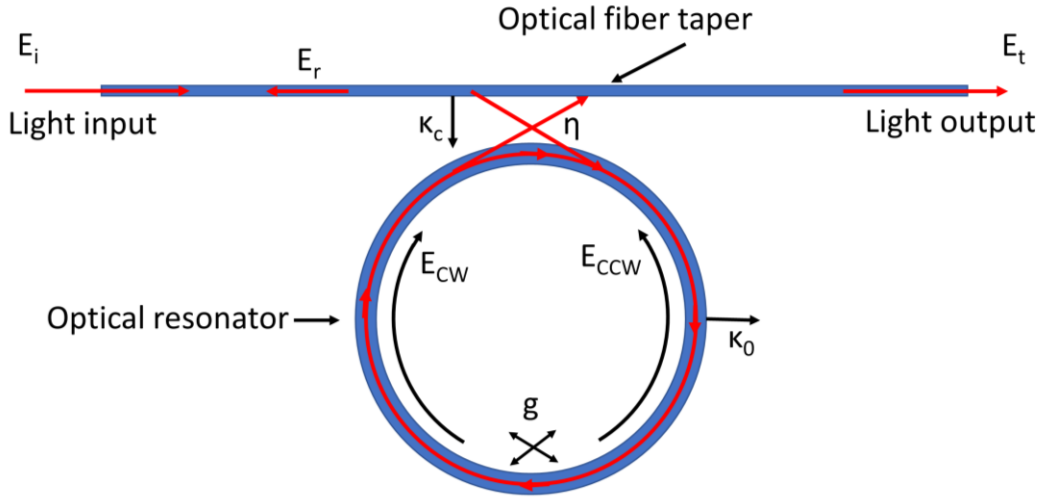


Figure 3.2 A schematic depiction of the phenomena that result from the interaction of microfiber and WGM fields in a micro-resonator.

The coupling excited a WGM propagating in the clockwise (CW) direction. The field transmitted by the microfiber is denoted by the symbol E_t , while the field reflected by the coupling of the backscattered clockwise WGM is represented by the symbol E_r . The value g represents the coupling coefficient between the two WGM counter-propagating due to the surface inhomogeneities. An exponential decline of the WGMs field with time is taken into account. This decline is denoted by the notation $E_{WGM} \approx e^{-k_0 t}$, where $k_0 = \omega/2Q_0$ is the cavity decay rate [87]. The parameter $k_c = \eta^2/2\tau = \omega/2Q_c$ is used to describe the coupling rate. The coupled-mode equations are [88]:

$$\begin{aligned}
 E_{CCW}(t) &= j\eta E_i(t) + \sqrt{1 - \eta^2} E_{CCW}(t - \tau) e^{-k_0 \tau} e^{j\delta\omega\tau} + jg\tau E_{CW}(t) \\
 E_{CW}(t) &= jg\tau E_{CCW}(t) + \sqrt{1 - \eta^2} E_{CW}(t - \tau) e^{-k_0 \tau} e^{j\delta\omega\tau} \\
 E_r(t) &= j\eta E_{CW}(t) \\
 E_t(t) &= \sqrt{1 - \eta^2} E_i(t) + j\eta E_{CCW}(t)
 \end{aligned}
 \tag{3.14}$$

If $\psi(t-\tau) \approx \psi(t) - \tau(d\psi/dt)$ also assume low losses, the equations presented above can be rewritten as:

$$\begin{aligned}
\frac{dE_{CCW}}{dt} &= -(k_0 + k_c - j\delta\omega)E_{CCW}(t) + j\frac{\eta}{\tau}E_i + jgE_{CW}(t) \\
\frac{dE_{CW}}{dt} &= -(k_0 + k_c - j\delta\omega)E_{CW}(t) + jgE_{CCW}(t) \\
E_r(t) &= j\eta E_{CW}(t) \\
E_t(t) &= \sqrt{1 - \eta^2}E_i(t) + j\eta E_{CCW}(t)
\end{aligned} \tag{3.15}$$

It is possible to derive the transmittance and reflectivity of the system in a situation where the solution is stationary.

$$\begin{aligned}
T(\omega) &= \left| \frac{E_t}{E_i} \right|^2 = \left| \sqrt{1 - \eta^2} - \frac{2k_c(k_0 + k_c - j\delta\omega)}{(k_0 + k_c - j\delta\omega)^2 + g^2} \right|^2 \\
R(\omega) &= \left| \frac{E_r}{E_i} \right|^2 = \left| \frac{2k_c g}{(k_0 + k_c - j\delta\omega)^2 + g^2} \right|^2
\end{aligned} \tag{3.16}$$

Under experimental conditions, the intrinsic losses of the resonator determine the value of k_0 , while the inhomogeneities of the surface determine the value of g . As a result, the k_c value can be modified experimentally; in most cases, this is accomplished by adjusting the distance that separates the microfiber and the micro-resonator.

3.2 Thermal poling basic theory

3.2.1 Single-Carrier Model

In 1994, Mukherjee et al. [44] described the thermal poling process's dynamics for the first time. According to the model, impurity ions in the glass matrix can create locally static electric fields capable of orienting the bonds by applying an external electric field. The induced $\chi^{(2)}$ is expressed by:

$$\chi^{(2)} \approx \chi^{(3)} E_{DC} + \frac{np\beta}{5k_B T} E_{DC} \quad (3.17)$$

Where $\chi^{(3)} E_{DC}$ denotes the third-order optical rectification process, and E_{DC} denotes the local field caused by the non-uniform charge distribution. In equation (3.17), β denotes the electric field-induced orientation of the second-order molecular hyperpolarizability, k_B denotes the Boltzmann constant, T indicates the absolute temperature of the sample, and p represents a permanent dipole moment associated with the bond. Finally, N is the total number of dipoles involved in the process. The latter entails the creation of a space-charge zone close to the anodic electrode that is entirely devoid of impurities. The negatively charged non-bridging oxygen (NBO) centers are contained within this part of the glass. Applying high electric fields at elevated temperatures allows the originally electrostatically linked ions to be dislodged and moved away. As a result of Poisson's equation, the electric field in the depletion region can be calculated [89].

$$E_{DC} = \frac{qn}{\epsilon}(\alpha - x), \quad 0 < x < a, \quad a = \left(\frac{2\epsilon V}{qn}\right)^{\frac{1}{2}} \quad (3.18)$$

Where α is the depletion width, n is the impurity concentration, q is the magnitude of the electronic charge, ϵ is the dielectric constant, and V is the difference in potential applied externally between the two electrodes. This result is based on the assumption that the width of the depletion layer on the anodic side is significantly greater than the width of the corresponding cathode accumulation layer. However, a subsequent study by Alley et al. [90] revealed several experimental observations incompatible with this single-carrier model, including multiple time scales for poling and the dependence on the sample thermal polling history.

3.2.2 Multiple-Carrier Model

Early experimental results appeared to confirm that a negatively charged region under the bulk silica sample's anodic surface [91] had formed as predicted by the single carrier model described in Section 4.2.1. Still, subsequent observations revealed that the thermal poling process of silica is more complicated than just a uniformly negatively charged region. For example, Kazansky et al. [92] discovered zones of alternating charge below the anode. At the same time, Myers et al. [28] found that the depth of the nonlinearity generated in polarized bulk samples was greater when samples were thermally poled for two hours rather than fifteen minutes. Suppose the depletion region was a uniformly negatively charged region. The electric field frozen into the glass was expressed by equation (3.18); then, according to equation (3.17), the $x^{(2)}$ induced would be peaked in the region closest to the anode rather than at a specific distance as was commonly observed in the initial poling experiments [93]. A more comprehensive description of space-charge region formation and the induction of second-order nonlinearity in bulk silica glasses was acquired by Kudlinski et al. in 2005 [94].

Even though the single-carrier model can still be used to describe the temporal evolution of depletion region formation early in the electromigration process,

multiple-carrier models become necessary to describe the poling process's temporal evolution after a specific time, called the optimal time (t_{opt}) [95]. Assuming that we take into account both the fast carriers (impurity charges) and the slow carriers (hydrogenated species), as well as both migration and diffusion phenomena, the equation of continuity and Poisson's equation can be written as [94]:

$$\frac{\partial p_i}{\partial t} = -\mu_i \frac{\partial(p_i E)}{\partial x} + D_i \frac{\partial^2 p_i}{\partial x^2} \quad (3.19)$$

$$\frac{\partial E}{\partial x} = \frac{q}{\varepsilon} \left[\sum_i (p_i - p_{0,i}) \right] \quad (3.20)$$

At the temperature used in the poling experiment, the i th species' instantaneous ion concentration (in ions/m³) is p_i , its initial ion concentration is $p_{0,i}$, and its mobility is μ_i . Aside from that, q denotes the electron charge, ε denotes the permittivity of the medium, D_i denotes the diffusion constant of the i th species, and k_B denotes the Boltzmann constant, with T representing the temperature of the medium. Equations (3.19) and (3.20) describe the spatial distribution of the electric field in the sample. The following assumptions concerning the voltage applied: the potential at the anodic surface ($x=0$) equals V_{app} , and the potential at the cathodic surface ($x=l$) equals zero. Consequently, the first boundary condition is as follows:

$$\int_0^l E dx = V_{\text{app}} \quad (3.21)$$

In contrast to the impurity charges (such as Na^+) already present in the sample at an initial uniform concentration p_{0,Na^+} , the hydrogenated species have an initial density p_{0,H^+} . They are injected into the glass at a rate dependent on how strong the electric field is at the anodic surface. As a result, the second boundary condition has the following form:

$$\left(\frac{\partial p_{\text{H}^+}}{\partial t}\right)_{x=0} = \sigma_{\text{H}^+} E(x=0) \quad (3.22)$$

Where σ_{H^+} denotes a variable parameter describing the charge injection of the hydrogenated species into the glass. By applying the voltage (V_{app}) throughout the entire sample of length l , an electric field equal to V_{app}/l is generated, and because $\mu_{\text{Na}^+} \gg \mu_{\text{H}^+}$, a depleted layer close to the anode surface of the glass is formed as a result of the Na ions migrating toward the cathode. External electromagnetic fields are shielded by an increased electric field generated at the sample's surface. The maximum E_{DC} value is achieved when the fully formed space charge region. The injected carriers' concentration per second increases rapidly at this point. Also, at this point, the drift velocity of the hydrogenated species $v_{\text{H}} = \mu_{\text{H}^+} E_{\text{DC}}$ equals or exceeds that of Na ions outside the depletion region, which has a reduced external electric field due to the space charge screening. When thermal poling lasts longer than a few minutes, the injected ions slowly replace the Na ions removed earlier, neutralizing the NBO^- centers [94].

3.3 Theoretical description of Strain-Optic effect in cylinders

A material's optical properties can change due to mechanical strain, described as the "strain-optic effect." Traditionally, this effect is expressed in terms of strain-induced (ϵ) variations of the relative dielectric impermeability tensor (the inverse of the permittivity tensor), denoted as η .

$$\eta_{i,j}(\epsilon) = \eta_{i,j}^{(0)} + \Delta\eta_{i,j}(\epsilon) = \eta_{i,j}^{(0)} + \sum_{k,l} p_{i,j,k,l} \epsilon_{k,l} \quad (3.23)$$

Where $\eta_{i,j}^{(0)}$ represents the impermeability tensor of the undisturbed material and $p_{i,j,k,l}$ represents the tensor of the strain-optic coefficients. In general, a tensor of the fourth rank has 81 independent elements. However, due to the strain tensor symmetry ($\epsilon_{k,l} = \epsilon_{l,k}$) [96] and the impermeability of tensor symmetry ($\eta_{i,j} = \eta_{j,i}$) [97], the number of elements is reduced to 36.

This enables the use of a contracted index notation to avoid double indices. As a result, $p_{i,j,k,l} = p_{m,n}$ where $m,n=1,2,\dots,6$. Equation 5.1 can be reduced to its simplest form using this notation.

$$\eta_m(\epsilon) = \eta_m^{(0)} + \Delta\eta_m(\epsilon) = \eta_m^{(0)} + \sum_n p_{m,n} \epsilon_n \quad (3.24)$$

There are no dimensions in terms of strain-optic coefficients, and the structure of the material medium determines the number of independent components. For isotropic materials, which is the case study in this chape, the number of independent components is reduced to two, and the strain-optic tensor can be written in contracted notation as follows:

$$p_{ij} = \begin{pmatrix} p_{11} & p_{12} & p_{12} & & \\ p_{12} & p_{11} & p_{12} & & \\ p_{12} & p_{12} & p_{11} & & \\ & & & p_{44} & \\ & & & & p_{44} \\ & & & & & p_{44} \end{pmatrix} \quad (3.25)$$

Where $p_{44} = \frac{1}{2}(p_{11} - p_{12})$. Once the expression of the strain-optic tensor has been described, it is necessary to determine the form of the strain tensor (i.e., how the mechanical strain is applied to the material) to obtain the variation of the dielectric permittivity of the material. This chapter will investigate the deformation a cylindrical MR (a rod) experiences when subjected to axial stretch.

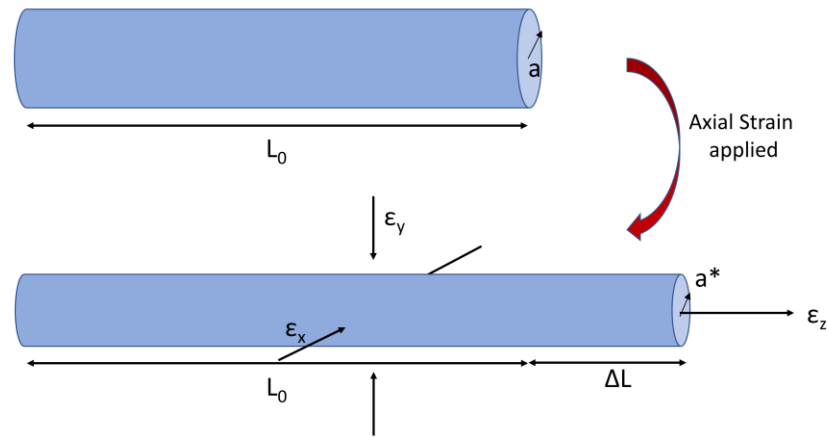


Figure 3.3 A schematic representation of the deformations experienced by a cylindrical-shaped resonator when subjected to axial stretch.

In Figure 3.3, an axial stretch is applied to a rod, and the effects of this stretch are depicted schematically. The unperturbed cylinder has the following dimensions: length L and radius a when no external strain is applied. It is important to note that when an axial deformation is considered, the length of the rod experiences elongation ΔL , which is combined with a reduction in the radius Δa . The axial deformation, denoted by ϵ_z , is given by the elongation of the axis

divided by the unperturbed length: $\varepsilon_z = \Delta L/L_0$. When a positive Poisson's ratio material is stretched in one direction, the elongation in that direction is accompanied by contractions in the two transversal directions of the material. The Poisson's ratio gives the ratio between these deformations, $\nu = -\varepsilon_x/\varepsilon_z$, $\nu = -\varepsilon_y/\varepsilon_z$.

We can calculate the variation of the impermeability of a rod under axial stretch by considering the different deformations and the strain-optic tensor:

$$\begin{pmatrix} \Delta\eta_x \\ \Delta\eta_y \\ \Delta\eta_z \\ \Delta\eta_{xy} \\ \Delta\eta_{yz} \\ \Delta\eta_{zy} \end{pmatrix} = \begin{pmatrix} p_{11} & p_{12} & p_{12} & & & \\ p_{12} & p_{11} & p_{12} & & & \\ p_{12} & p_{12} & p_{11} & & & \\ & & & p_{44} & & \\ & & & & p_{44} & \\ & & & & & p_{44} \end{pmatrix} \begin{pmatrix} -\nu\varepsilon_z \\ -\nu\varepsilon_z \\ \varepsilon_z \\ 0 \\ 0 \\ 0 \end{pmatrix} \quad (3.26)$$

We can determine the axial strain-induced changes in the permittivity tensor by solving the equation (3.26). The refractive index (n) of a material is linked with the permittivity (ε_r) and permeability (μ_r) with the following mathematical formula $n = \sqrt{\varepsilon_r \mu_r}$. However, materials are nonmagnetic in optical frequencies, and as a result $\mu_r = 1$. As a result, the 3.26 can be written as:

$$\begin{pmatrix} \Delta\varepsilon_x^{-1} \\ \Delta\varepsilon_y^{-1} \\ \Delta\varepsilon_z^{-1} \end{pmatrix} = \begin{pmatrix} p_{11} & p_{12} & p_{12} \\ p_{12} & p_{11} & p_{12} \\ p_{12} & p_{12} & p_{11} \end{pmatrix} \begin{pmatrix} -\nu\varepsilon_z \\ -\nu\varepsilon_z \\ \varepsilon_z \end{pmatrix} \quad (3.27)$$

Using the relationship $\varepsilon_r = n^2$ we can derive

$$\frac{1}{(n + \Delta n)^2} - \frac{1}{n^2} = \begin{pmatrix} p_{11} & p_{12} & p_{12} \\ p_{12} & p_{11} & p_{12} \\ p_{12} & p_{12} & p_{11} \end{pmatrix} \begin{pmatrix} -\nu\varepsilon_z \\ -\nu\varepsilon_z \\ \varepsilon_z \end{pmatrix} \quad (3.28)$$

We can analyze the left term of the above with the Taylor series.

$$\frac{1}{(n + \Delta n)^2} - \frac{1}{n^2} = \Delta n \text{ is very so } \frac{\Delta n}{n} \rightarrow 0 \text{ and } \frac{\Delta n}{n} = x \quad (3.29)$$

Taylor series in $\frac{1}{(1+x^2)}$ around 0.

$$f(x) = \frac{1}{(1+x)^2}, \quad f(x) = f(a) + f'(a) \frac{(x-a)}{1!} + \dots, \quad a = 0$$

$$f(x) = 1 - 2x \text{ As a result } \frac{1}{n^2 \left(1 + \frac{\Delta n}{n}\right)^2} - \frac{1}{n^2} \rightarrow \frac{1-2x}{n^2} - \frac{1}{n^2} = -\frac{2\Delta n}{n^3}$$

As a result, the 3.26 equation becomes:

$$\begin{pmatrix} \Delta n_x \\ \Delta n_y \\ \Delta n_z \end{pmatrix} = -\frac{n^3}{2} \begin{pmatrix} p_{11} & p_{12} & p_{12} \\ p_{12} & p_{11} & p_{12} \\ p_{12} & p_{12} & p_{11} \end{pmatrix} \begin{pmatrix} -v\varepsilon_z \\ -v\varepsilon_z \\ \varepsilon_z \end{pmatrix} \quad (3.30)$$

The transversal components x and y have the same variation. $\Delta n_t \equiv \Delta n_x = \Delta n_y$.

$$\begin{aligned} \Delta n_t &= -\frac{n^3}{2} [-vp_{11} + (1-v)p_{12}] \varepsilon_z \\ \Delta n_z &= -\frac{n^3}{2} [p_{11} - 2vp_{12}] \varepsilon_z \end{aligned} \quad (3.31)$$

Another view of the above equations is the following.

$$\begin{aligned}\frac{\Delta n_t}{n\varepsilon_z} &= -\frac{n^2}{2}[-vp_{11} + (1-v)p_{12}] = p_{TE} \\ \frac{\Delta n_z}{n\varepsilon_z} &= -\frac{n^2}{2}[p_{11} - 2vp_{12}] = p_{TM}\end{aligned}\tag{3.32}$$

Axially induced strain, $\varepsilon_z = \Delta L/L_0$, and variations in the radius and Poisson's ratio (v) determine the changes in the mechanical properties of an optical resonator. Specifically, to investigate how an axial stretch influences the spectral position of the WGM resonances in a cylindrical dielectric resonator, it is necessary to solve the characteristic equations for a uniaxial medium described in equation 3.10.

$$\Delta\alpha = -\alpha v\varepsilon_z = -\alpha v \frac{\Delta L}{L_0}\tag{3.33}$$

We can obtain the relative shift of the WGM resonances considering the resonant condition for a WGM, $m\lambda_R = 2\pi n_{eff}$, and apply a perturbative approach as a function of the axial strain.

$$\frac{\Delta\lambda_R}{\lambda_R} = \left(\frac{1}{\alpha} \frac{d\alpha}{dS_z} + \frac{1}{n_{eff}} \frac{dn_{eff}}{dS_z} \right) \Delta\varepsilon_z\tag{3.34}$$

Incorporating strain as a perturbation in the characteristic equations of the WGMs, Eqs (3.10), enables us to write the first-order approximation for the relative shift of the resonances [66]:

$$\left[\frac{\Delta \lambda_R}{\lambda_R} \right]_{TE, TM} = \frac{\Delta \alpha}{\alpha} + (1 - C_{TE, TM}) \frac{\Delta n_{t,z}}{n_0} \quad (3.35)$$

$C_{TE, TM}$ is a small coefficient dependent on wavelength, radius, and the material's refractive index. The coefficient is distinct for each polarization state and can be determined using the experimental parameters. The strain-optic coefficients can be obtained by measuring the shift of both polarizations as a function of the strain and solving a linear system of equations.

$$S_{TE, TM} = -\nu - (1 - C_{TE, TM}) p_{et, ez} \quad (3.36)$$

The slopes of the WGM resonances relative shift with axial strain for each polarization are S_{TE} and S_{TM} , respectively. Eq. (3.35) adds a 4 percent correction to the rough estimate obtained when the effective index of the modes is approximated to the material refractive index ($C_{TE, TM} = 0$) in Eq (3.34). As a result, to obtain the most precise values for evaluating the strain-optic effect, we will use Eq. (3.35) to calculate p_{11} and p_{12} . According to Equations (5.5) and (5.9), strain-induced birefringence is

$$\frac{\Delta n_{strain}}{n_0} = \frac{\Delta n_{TM}}{n_0} - \frac{\Delta n_{TE}}{n_0} = \frac{\Delta \lambda_{TM}}{\lambda_{TM}} - \frac{\Delta \lambda_{TE}}{\lambda_{TE}} \quad (3.37)$$

And leads to the optical strain coefficient

$$K' \equiv \frac{\Delta n_{strain}}{\varepsilon_z(1 + \nu)} = \frac{n^3}{2} (p_{12} - p_{11}) \quad (3.38)$$

with corresponding stress optical coefficient

$$K \equiv K' \frac{1 + \nu}{2E} \quad (3.39)$$

3.4 Summary

This chapter presents the theoretical framework of whispering gallery mode resonances, emphasizing cylindrical symmetries and coordinates. The discourse extends to an in-depth consideration of mode resonance theory and associated sensing mechanisms. Subsequently, it elucidates the fundamental principles of thermal poling, culminating with a comprehensive analysis of the strain-optic effect.

4 Whispering gallery mode resonances in thermally poled borosilicate glass hetero-fibers

This chapter investigates radially oriented thermal poling in borosilicate glass optical fibers, then examines whispering gallery mode resonances within these hetero-fibers.

4.1 Borosilicate glass hetero-fiber

The Duran® Schott, a borosilicate glass tube in which a co-centric silver wire is placed, was used to create the glass hetero-fibers used in the current experiments. The diameter of the resulting glass fiber is approximately 115 μm , and the diameter of the silver wire is about 20 μm , respectively (see Fig.4.1). The chemical composition of Duran® Schott glass is 81% SiO_2 , 13% B_2O_3 , 4% $\text{Na}_2\text{O}+\text{K}_2\text{O}$, and 2% Al_2O_3 [98]. While we employ this specific optical fiber to stimulate WGMs resonances, it has been demonstrated that these optical fibers can facilitate light waveguiding proximal to the fiber's core [99]. A value of $n_{\text{Duran}}=1.4563$ was calculated using extrapolation of the Sellmeier equation at 1.5 μm spectral region using coefficients from the visible wavelength regime for the refractive index of the pristine Duran® Schott glass hetero-fiber. The Sellmeier equation is an empirical relationship between the refractive index and the wavelength of a transparent medium. Light dispersion in a medium can be calculated using this relationship. Specifically, the equation consisting of three terms is commonly used to characterize the glasses [100].

$$n^2(\lambda) = 1 + \frac{B_1\lambda^2}{\lambda^2 - C_1} + \frac{B_2\lambda^2}{\lambda^2 - C_2} + \frac{B_3\lambda^2}{\lambda^2 - C_3} \quad (4.1)$$

Where n is the refractive index of the glass, λ is the wavelength, and $B_{1,2,3}$ and $C_{1,2,3}$ are experimentally determined Sellmeier coefficients. We can calculate the six unknown parameters of equation 4.1 by using the specific 6 combinations of refractive index and wavelength for Duran glass that have been identified [101].

<i>Wavelength (nm)</i>	<i>Refractive index</i>
435.8	1.4802
479.9	1.4768
546.1	1.4731
589.3	1.4713
643.8	1.4695
656.3	1.4692

Then, the coefficients that best fit the equation can be extracted for the previously mentioned wavelength-refractive index combinations.

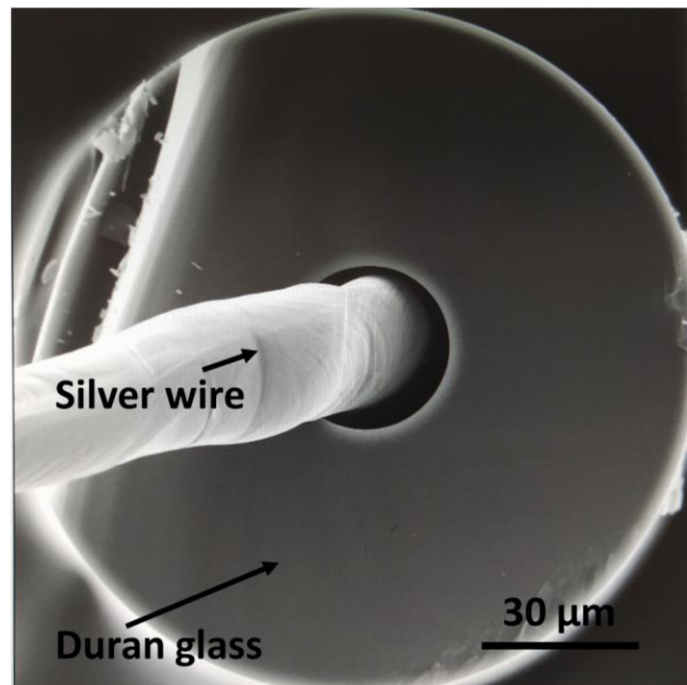


Figure 4.1 A SEM image depicting the cross-section of a borosilicate glass hetero-fiber

4.2 Thermal poling experimental setup

Initially, an effort was invested to thermally pole the optical hetero fiber within a stainless steel ferrule. In this specific arrangement, the central metallic wire was connected to the negative electrode of the high power supply, while the metallic ferrule was linked to the positive electrode. However, by applying up to 200 Volts, the micrometric-scale distance between the electrodes exceeded the electric breakdown threshold of the borosilicate glass ($\sim 40 \text{ V}/\mu\text{m}$).

As a result, the Margulis et al. [33] approach was adopted to achieve significant ion migration in the outer circumference of the particular glass hetero-fiber geometry, where WGM resonance is confined. Thus the cathode was connected to the inner metallic wire, while the surface of the hetero-fiber was grounded (see Fig. 4.2).

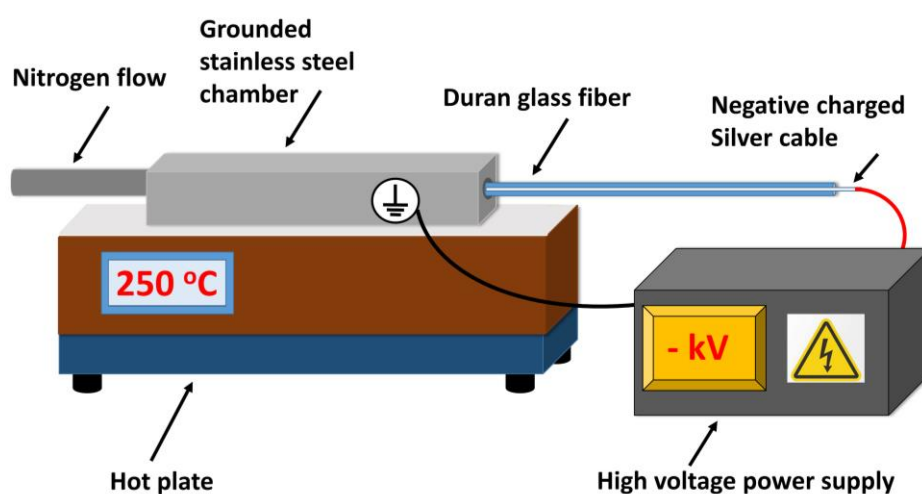


Figure 4.2 Schematic representation of the thermal poling experimental setup

Glass hetero-fibers with lengths $\sim 12 \text{ cm}$ were thermally poled in a stainless-steel chamber (with a fixed volume of 20 cm^3) in a flowing nitrogen atmosphere (with a flow rate of approximately $65 \text{ cm}^3/\text{sec}$). Using nitrogen gas flow, it was possible to prevent the introduction of hydroxyl groups into the glass network

from the surrounding environment, thereby avoiding partial neutralization of the ion-depleted zone that had formed [102].

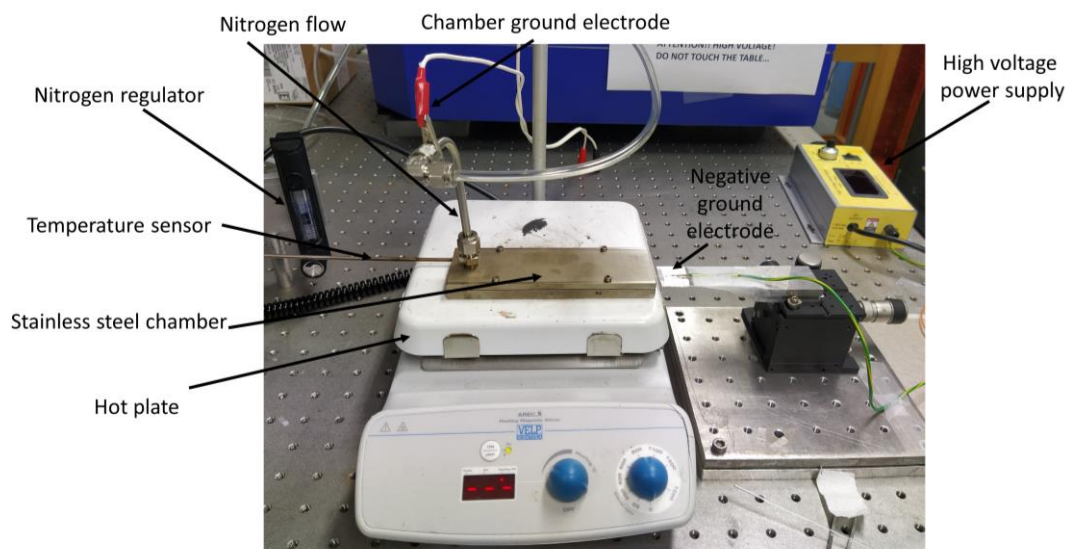


Figure 4.3 The thermal poling experimental setup

A high-voltage power supply (HVPS) was used to generate axial electric fields (18 MV/m) between the metal core and the glass cavity's circumference (Fig. 4.2). Silver conductive paste connected the HVPS's negative electrode (cathode) to the metalcore. Additionally, the stainless-steel anode directly contacted the glass fiber surface. The stainless-steel chamber was placed on top of a hot plate that could reach temperatures of up to 300 degrees Celsius with an accuracy of one degree Celsius. The central metallic core applied negative voltages ranging from 700 V to 1000V. The breakdown voltage of the borosilicate glass necessitated limiting our experiments to 1000 V. Due to the high alkali concentrations in Duran® Schott glass, it was impossible to pole it using the same procedure used for fused silica glass, that is, to directly set the final value of electric potential. Instead, it was poled using a different approach. A step-by-step voltage increment was implemented to ensure the current flow did not exceed a critical limit (1mA) [103], preventing a thermal runaway. Experimental evidence has revealed that an increment rate of 100V every 10 minutes, following an initial increase of 600 V, meets the criteria outlined in the previous

section. Thermal polling was conducted at a temperature of 250°C for poling times ranging from 20 minutes to 75 minutes. After this period, the hotplate was turned off to cool down, but the DC voltage was kept on until the poled hetero-fiber reached room temperature.

4.3 WGMs experimental setup

Before and after the thermal poling process, the spectral characteristics of Duran® glass hetero-fiber cavities were determined using the apparatus illustrated in Figure 4.3. An adhesive tape was used to attach the hetero-fibers to a bronze fork custom designed for this project.

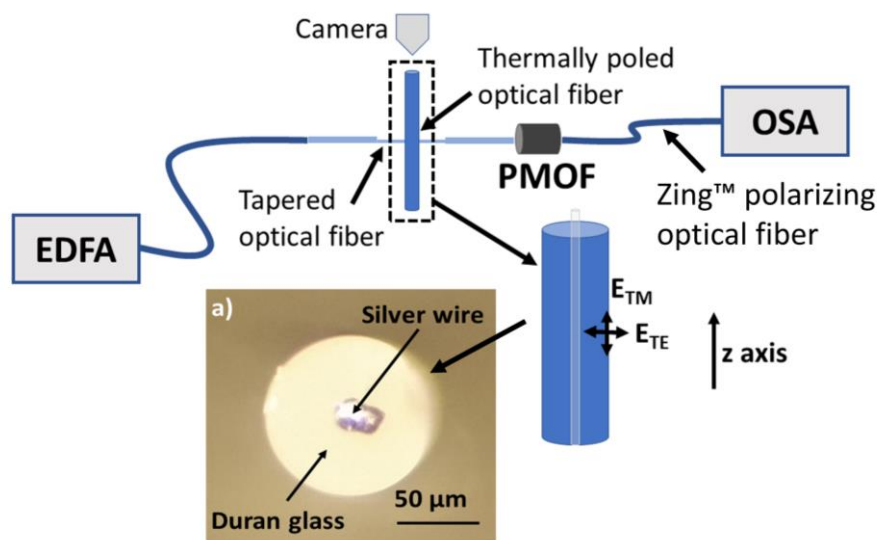


Figure 4.4 Whispering gallery modes experimental setup Inset (a) Optical microscopy cross-section picture of the 115 μm diameter Duran glass microcavity.

A 2.2 μm diameter tapered standard telecom optical fiber was used to excite the WGMs within the optical cavity and light from an erbium-doped fiber amplifier (EDFA) in the 1.5-micron spectral region. An optical spectrum analyzer (OSA) was used for signal recording. A Zing™ polarizing optical fiber (ZF) was used

to resolve the TE and TM modes supported inside the cylindrical resonator, respectively (see Fig. 4.4), with a polarization extinction ratio of 6 dB/m approximately. Our notation has stated that TE modes' electric field vectors are perpendicular to the z-axis. In contrast, TM modes' electric field vectors are perpendicular to the z-axis. The radial (l) and azimuthal (m) modal numbers can be used to define the localization of each optical WGM within a cylindrical resonator. No axial modal number is determined since the resonator structure is nearly cylindrical.

4.4 Optical and material diagnostics procedures

Non-linear microscopy was used to probe second-harmonic generation (SHG) in backscattered mode, using femtosecond laser radiation at 1028nm, 200fs, and 50MHz to confirm the impact of the thermal poling process on the treated hetero-fiber under the specific conditions. Thermally poled samples that had been well-cleaved were examined using the experimental setup (apart from the laser source) and procedure described elsewhere [104]. Also investigated was the possibility of structural changes occurring within the glass, specifically close to the anode side.

A Raman spectroscopy setup was used to accomplish this. A laser of 532 nm wavelength with a power of 24mW was used to illuminate the sample during the Raman measurements [105]. A long working distance objective lens with 50x magnification and 0.50 NA was used to focus the laser beam on the end face of the glass hetero-fiber. The grating groove density was 600 grooves/mm, and each measurement was exposed for 5 seconds.

Finally, Energy Dispersive X-Ray Spectroscopy (EDX) was used to determine the spatial distribution of ions within the hetero-fiber glass matrix and confirm the presence of electromigration effects in the matrix.

4.5 Type of thermal poling anode

As mentioned earlier, negative charges are formed after the poling process due to the depletion of the subanodic glass region from positive charge carriers, alkali, and alkali-earth ions. Alkali ions move under a very high electric field with magnitudes of up to volts per nanometer in a thick micrometer layer beneath the anode [106]. Using an open anode that is an electrode that allows contact between the negatively charged anodic surface of the glass under poling and the surrounding atmosphere; it is proposed that the essential compensation of negatively charged non-bridging oxygen atoms is due to the injection of positively charged species of atmosphere origin into the glass. The positively charged species of atmosphere origin are most likely $\text{H}_3\text{O}^+/\text{H}^+$ ions [107]. This process results in hydrogen bonding with non-bridging oxygen in glass, thus, neutralizing the negative charge. In poled glasses, oxygen-bonded hydrogen has been observed several times [108].

Similarly, in the presence of an anodic electrode that prevents the glass from coming into contact with the atmosphere, such as metal films deposited via vacuum sputtering [109] (poling with a so-called blocking anode), poling in a vacuum [110], or poling in an inert atmosphere, the depth of the alkali-depleted region decreases to the micrometer range, and the negative charge is compensated. Most studies using poled glasses have failed to uncover this compensatory mechanism. Regarding soft silicate glasses, such as the widely used soda-lime glass or borosilicate glass in poling experiments, there are only two negatively charged species: oxygen ions and electrons, both in abundance. As a result, the nature of the anode electrode is expected to influence the type of compensation mechanism that occurs during poling, which is triggered by the depletion of mobile cations. According to the IR and Raman spectroscopy results presented by Marc Dussauze et al. [109], the formation of the hydroxyl group was detected only in the case of the air-poled glass, which suggests that it is possible to distinguish significantly between the two electrode configurations. However, they observed a common characteristic for both atmospheric

conditions: an increase in the degree of polymerization of the silicate network within the space charge zone, regardless of the atmospheric condition. The loss of non-bridging oxygen atoms would cause an increase in the population of bridging bonds within the silicate network, as previously discussed for other glass systems [111]. This would indicate that oxygen ions played an important role in anionic conduction during poling. So it turns out that both $\text{H}_3\text{O}^+/\text{H}^+$ ions injection and, to a lesser extent, non-bridging oxygen removal serves as compensation mechanisms for the air-poled sample [109]. However, no $\text{H}_3\text{O}^+/\text{H}^+$ ions were detected in the argon-poled sample. Structural rearrangements inducing anionic conduction by releasing non-bridging oxygen atoms appear to be the dominant compensatory mechanism.

4.6 Thermal poling results in Nitrogen Flow

The thermal poling process was carried out in the hetero-fiber under the presence of nitrogen flow, inhibiting the insertion of cation species from the surrounding atmosphere into the glass on the anode side throughout the procedure.

4.6.1 Microscopy mapping using non-linear techniques

To validate the glass structure's thermal poling, we examined poled and unpoled hetero-fibers using non-linear 1028nm laser microscopy to trace the SHG signal caused by ion displacement. Figure 4.4a shows an SHG image of the hetero-fiber cross-section illustrating the spatial distribution of second-order nonlinearity for a cavity poled in the presence of nitrogen at 250 °C for 75 minutes with a negative voltage of 900 V applied to the central wire; Fig. 4.4b shows a corresponding SHG image of the unpoled hetero-fiber.

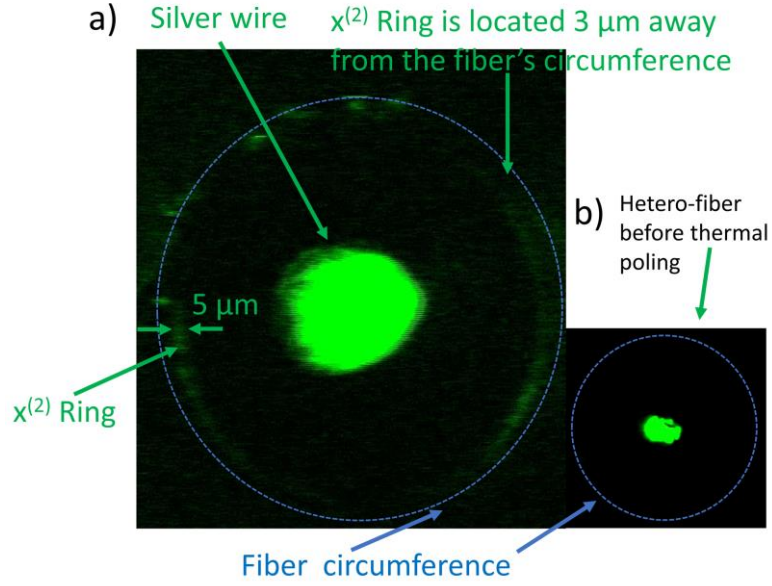


Figure 4.5 a) SHG signal obtained from a poled hetero-fiber WGM cavity cross-section for 75 min poling time b) The corresponding SHG image from the unpoled hetero-fiber.

As a result of the ion migration and dipole formation, the SHG experiments revealed an annular green ring around the hetero-fiber glass cavity's outer circumference, with typical dimensions of about 5 μm , locally introducing non-linear dielectric susceptibility $\chi^{(2)}$. The distance between the green SHG ring and the outer surface of the hetero-fiber is measured to be approximately 3 microns; this is in good agreement with poling experiments in fused silica and borosilicate glasses, respectively [112]. The silver cable responsible for the SHG signal can be seen in the center of Figure 4.5 [113]. After six months, the same hetero-fiber was obtained, with the same SHG signal intensity, to ensure the poling process was stable. The experiments described above show that the hetero-fiber was thermally poled, and ion electromigration occurred in a radially distributed pattern.

4.6.2 WGM spectra obtained experimentally in hetero-fiber cavities

Non-linear laser microscopy investigations were followed by measurements of WGM spectra, which were obtained using the experimental procedure described earlier and compared to the WGM spectra of the unpoled cavities. In Figure 4.6-4.8, a comparison of the effect of thermal poling on the WGM spectra for each polarization component is shown, with modal (loaded) Q-factors reaching 5.9×10^4 for both polarisations, as estimated from their respective linewidths [114]. Along with the fundamental WGM modes (zeroth radial order and varying azimuthal order), the un-poled hetero-fiber sample (Fig. 4.6 a, b) supports many of higher-order interstitial radial modes, as expected given the large radius of the cylindrical resonator. Full-wave eigenvalue simulations (COMSOL Multiphysics) were used to allocate the modal order and describe the WGM resonance of the glass hetero-fiber cylindrical geometry. The free spectral range (FSR) of the azimuthal modes with radial order $l=1$ for both polarizations is 4.62 nm which agrees with the theoretical value $\frac{\lambda^2}{2\pi r n}$.

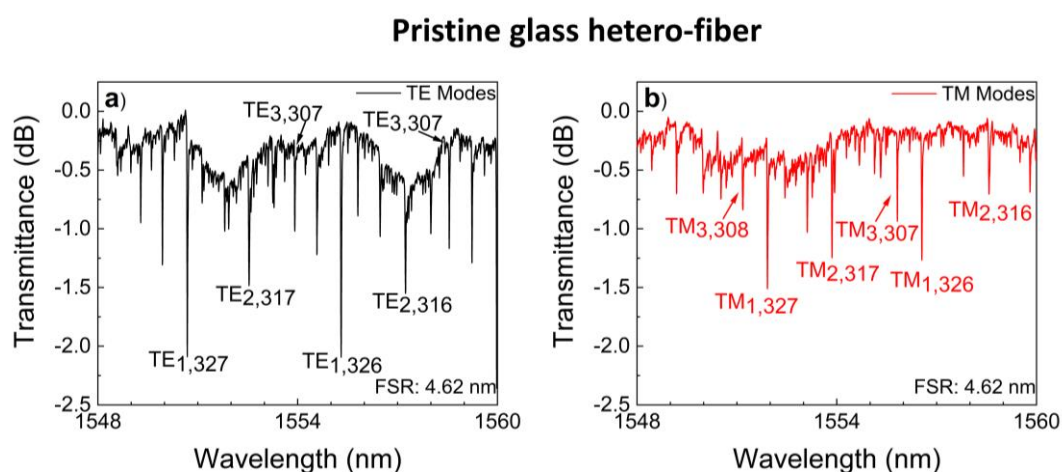


Figure 4.6 Experimental WGMs spectral results for both polarization states, TE Modes (black) and TM Modes (red), for pristine glass hetero-fiber

The corresponding spectra for the same wavelength band obtained after thermal poling for 75 min (Fig.4.7) reveal the impact of ion migration into the WGM resonance in the glass cavity.

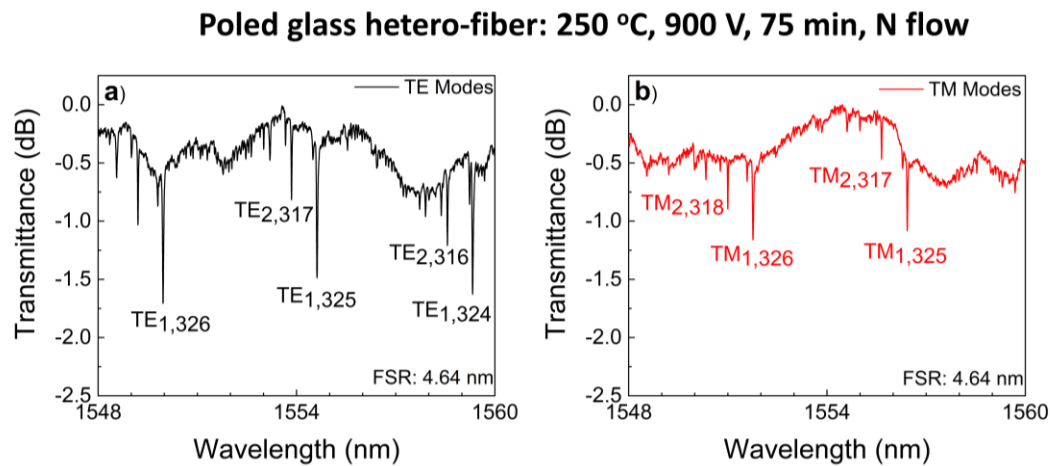


Figure 4.7 Experimental WGMs spectral results for both polarization states, TE Modes (black) and TM Modes (red), for poled glass hetero-fiber for 75 minutes poling time

More precisely, a selective compression, or even annihilation, of higher-order radial modes with radial orders $l=2$ and $l=3$. The mean value of the FSR of azimuthal modes for $l=1$ for both polarizations increased to 4.64 nm, indicating a change in the refractive index of the ring area where these modes are localized. Furthermore, a decrease in the strength of higher radial order modes is observed, accompanied by a reduction in the quality factor ($\sim 4.6 \times 10^4$).

In experiments with identical conditions, this specific spectral behavior of the WGMs resonances in thermally poled glass hetero-fibers was consistently detected. Shorter poling durations resulted in weaker and fewer mode suppressions (see Fig.4.8) for a cavity poled for a 45min session. In the case of poling times less than 20 minutes, no modal suppression effects were observed.

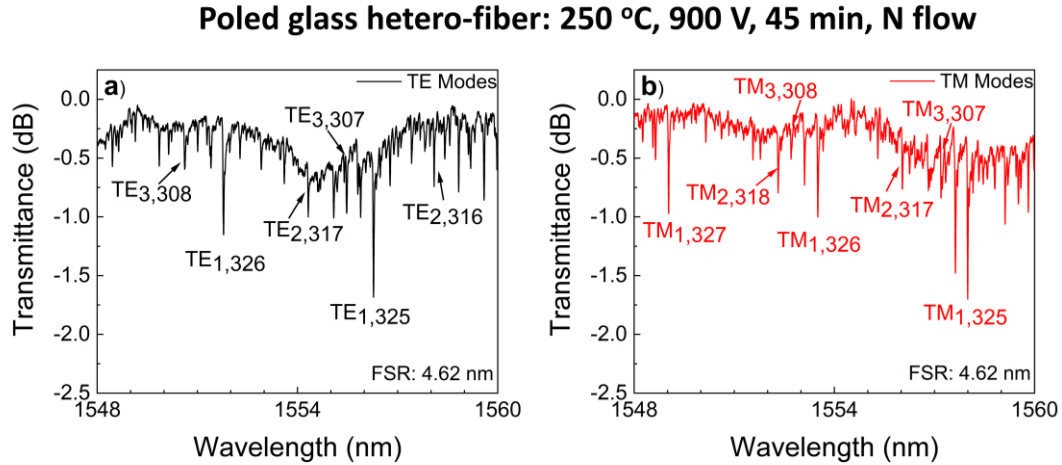


Figure 4.8 Experimental WGMs spectral results for both polarization states, TE Modes (black) and TM Modes (red), for poled glass hetero-fiber for 45 minutes poling time

4.6.3 Structural investigations of the hetero-fiber WGM cavities

Further understanding of the WGM spectral data in Figure 4.6-4.8 will require precisely mapping the radial refractive index changes induced in thermally poled optical hetero-fiber cavities. Due to the presence of the center metallic wire, which interfered with end-face light firing and efficient light guidance, traditional back-illumination procedures were unable to perform refractive index mapping. An alternative approach was used to investigate the spatial distribution of ion migration and the structural changes induced in the poled glass by employing energy-dispersive X-ray spectroscopy (EDX) and Raman scattering measurements close to the anode side. The above techniques gave us a qualitative picture of the profile of refractive index changes.

EDX measurements of a pristine and a thermally poled (75 min, at 250 °C) hetero-fiber are presented in Figure 4.9. The primary cations traced were sodium (Na) and potassium (K), as their distribution essentially defines the local refractive index profile. They are the glass network modifiers that can move in response to an external electric field. A flat-like ionic distribution runs along the length of the pristine hetero-fiber. Figure 4.9a reveals that the atomic

concentration changes along the radial direction are less pronounced for the heavier and larger (in volume) potassium cation than the lighter and smaller sodium. The data shows that this difference between the two cations is more pronounced at greater depths from the fiber circumference. Surprisingly, this finding is consistent with the well-established importance of activation volumes for cation transport in glassy electrolytes [115]. For the poled sample, Figure 4.9b illustrates how the spatial distribution of the total cationic atomic concentration ($\text{Na} + \text{K}$) varies concerning distance from the fiber's surface [116]. Fig. 4.9b represents the total spatial distribution of the ions in a thermally poled sample divided into three distinct zones [117]. The ion-depleted (ID) region, located just below the hetero-surface fibers and has a width of approximately 3 microns, is followed by the ion accumulation (IA) zone, which has a width of about 5 microns. The rest is consistent with the original glass state.

The spatial results obtained using SHG imaging (see Fig. 4.5) and those obtained using EDX spectroscopy (see Fig. 4.9a, b) are qualitatively consistent, with the SHG ring completely overlapping the EDX-mapped ion-accumulation zone [102], [118], [119]. The thermal poling technique negatively changes the refractive index profile near the anode side. Depending on the glass stoichiometry, it can be as high as $n \approx 0.1$ [120], with correspondingly positive changes in the refractive index assumed in the middle of the ion-accumulation zone.

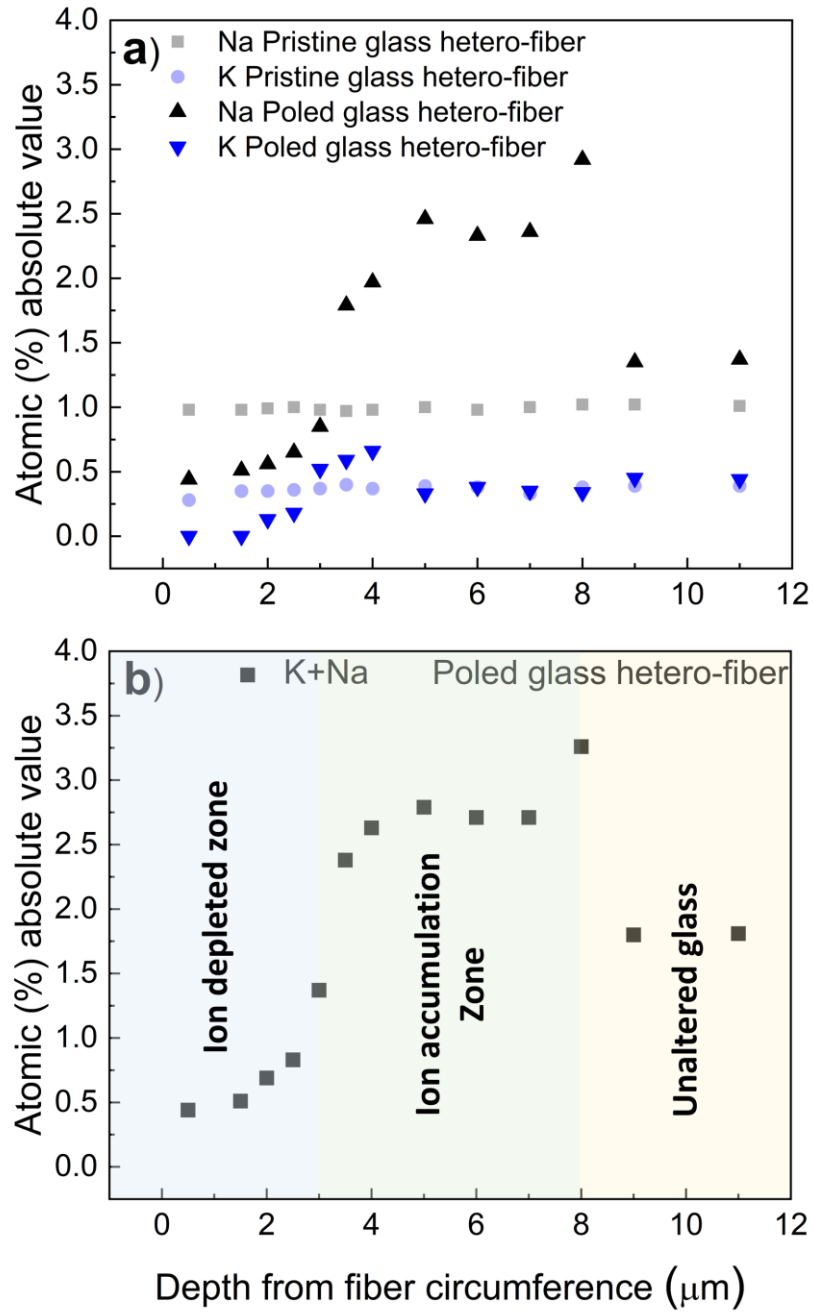


Figure 4.9 (a) Analysis of atomic concentration of the cationic network modifiers (Na, K) versus depth from fiber circumference was performed using EDX (b) The spatial distribution of the total atomic concentration of the ions above is plotted as a function of the distance from the circumference of the fiber.

We will then investigate the structural effects of cation displacement on the optical fiber's glass network by employing Raman vibrational spectroscopy. A representative μ -Raman spectrum from each of the three zones (cation depleted, cation accumulation, and pristine) is shown in Figure 4.10. A strong band dominates all spectra at around 450 cm^{-1} and a weaker profile at about 800 cm^{-1} . The former is attributed to the network's silicate entities, whereas the latter results from vibrations within the boroxol units of the borosilicate network [121], [122]. The spectra have been normalized to the dominant 450 cm^{-1} band to facilitate comparisons. In addition, Figure 4.11 depicts the variation in the full-width half maximum (FWHM) of the 450 cm^{-1} profile as a function of the circumference depth. This broad silicate Raman band comprises SiO_4 tetrahedral units containing four bridging oxygens, one non-bridging oxygen, and two non-bridging oxygens. It is well established that introducing non-bridging oxygens increases FWHM due to the gain of intensity near $580\text{-}590\text{ cm}^{-1}$, the region where the two non-bridging oxygen silicate entities are active. As shown in Figure 4.11, the full width at half maximum (FWHM) of the silicate band increases as we move from the ion-depleted region to the ion accumulation zone before stabilizing at a constant value for all depths within the unaltered glass. These findings are in excellent agreement with the relationship between cation concentration and depth (Fig.4.9). As the cations migrate towards the core of the optical fiber, the silicate part of the network depolymerizes, allowing the introduction of negatively charged non-bridging oxygen atoms into the network to balance the positive charge difference caused by the cation accumulation.

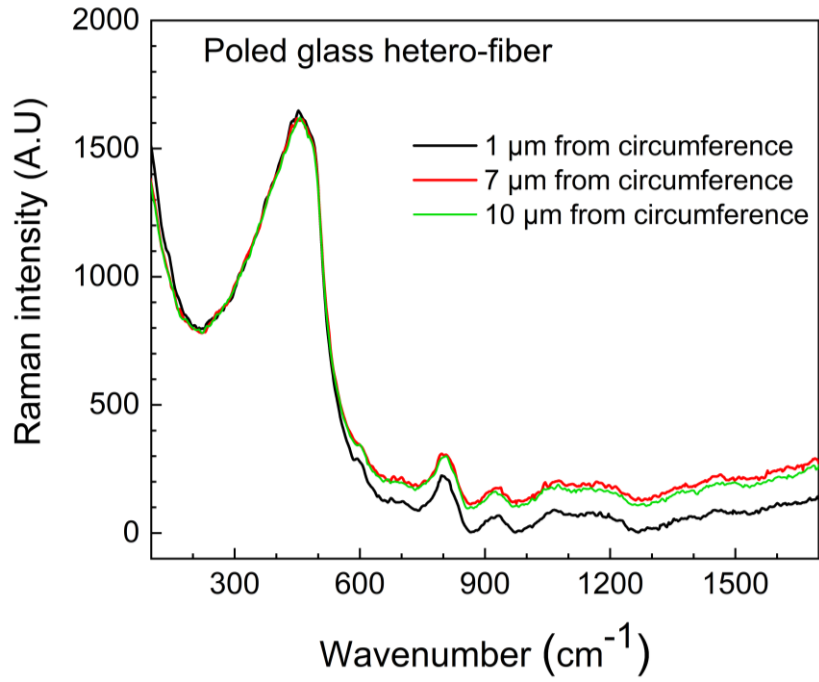


Figure 4.10 Raman spectra of the thermally poled hetero-fiber cross-section for three distances from fiber circumference.

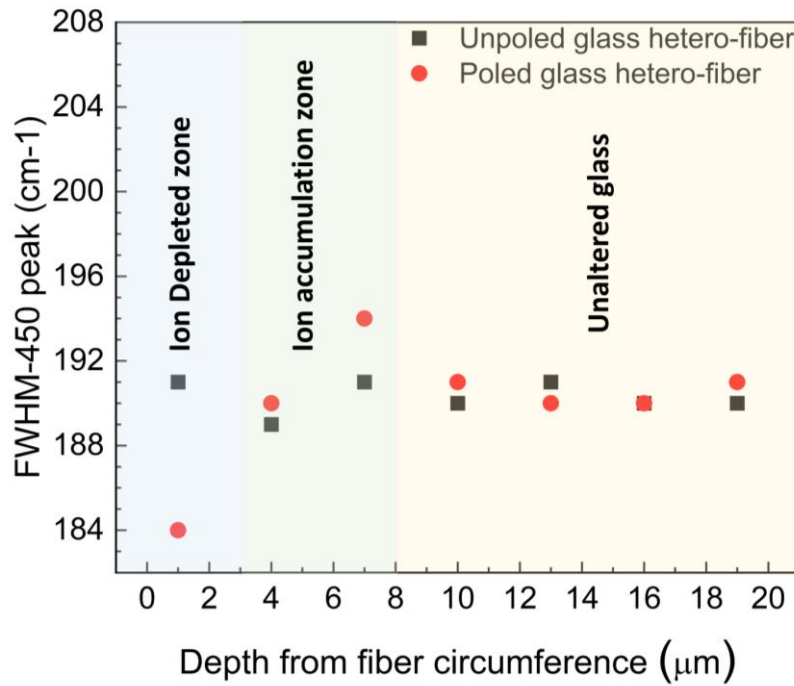


Figure 4.11 Silicate entities 450 cm^{-1} Raman band FWHM versus depth from the fiber circumference.

Moreover, the relative intensities of the two main modes at 450 cm^{-1} and 800 cm^{-1} indicate the average population of silicate and boroxol entities of the mixed

borosilicate network. The increase in the latter feature compared to the 450cm^{-1} feature suggests that the cation movement induces the coupling of the silicate entities to the boroxol rings, resulting in mixed borosilicate rings. Previous optical, spectral, elemental, and structural investigations established the effect of thermal poling on the refractive index properties of the Duran® hetero-fiber by forming two distinct annular, concentric regions, with the outer (ion-depleted-zone) undergoing negative refractive index changes and the middle (ion-accumulation-zone) undergoing positive refractive index changes. In agreement with this assumption are the FSR data obtained for WGMs with $l=1$, which were localized close to the periphery of the fiber. The blue shift of the TE(1,m) modes is attributed to the reduction of the refractive index of the outer “ion-depleted” layer due to the thermal poling and ion-migration process.

From the free spectral range and the spectral positioning of different order WGMs, we have evaluated a “nominal refractive index” for this outer zone used to build a refractive index profile used in the numerical simulations (see next chapter). More specifically, cavities poled for 75 minutes correspond to a locally probed, negative refractive index change of $\Delta n_{ID} \sim -6.3 \times 10^{-3}$. By correlating this refractive index change Δn_{ID} , with the EDX measurements of the ion-depleted and pristine zones, we can estimate an average refractive index change per combined Na/K ions concentration changes $\Delta c_{Na/K}$, as $\xi = \Delta n_{ID} / \Delta c_{Na/K}(\%)$, having an approximate value of 6.3×10^{-3} . By taking into account, the ratio ξ and the EDX ion-concentration data in Fig.4.8, the refractive index change of the middle ion-accumulation zone is estimated to be $\Delta n_{IA} \sim 1.0 \times 10^{-2}$; a Figure that agrees with the reports presented by others [117], [123]. The specific refractive index values best fit the simulation results presented in the next chapter with the experimental data. Additionally, we assume that both the Δn_{ID} and Δn_{IA} quantities are primarily attributed to ionic-polarizability-induced refractive index changes and less to stress-induced refractive index changes [124], as Duran® is a thermally tempered glass and stresses generated at the interface between the metal wire and the glass are primarily localized well away from the hetero-fiber circumference.

4.6.4 Finite element analysis simulations

After applying the radial thermal poling procedure to this Duran® hetero-fiber, the main question is the physical reason behind the suppression of higher radial (l) order WGMs supported in this fiber. Radially distributed loss and/or refractive index changes could be involved in a modal tailoring mechanism. However, because the overall loss and Q-factor of the relevant spectral resonances in the WGM spectra obtained for Duran® hetero-fibers before and after poling are not significantly different, the correlation between observed selective modal suppression and a loss-driven mechanism appears improbable. Instead, a purely refractive index-based mechanism can be investigated. The refractive index profile introduced by the thermal poling process hint at the excitation and resonance of specific radial modes.

In particular, we demonstrate that the suppression/destruction of higher-order radial WGMs in the thermally poled hetero-fiber cavities produced by the refractive index step profile formed in the outer ion-depletion and inner ion-accumulation zones is justified. As a result of the lower refractive index of the ion-depletion zone, the excitation efficiency for higher-order radial modes, primarily contained within the volume of the WGM resonating cavity, is reduced. The significant increase in the refractive index of the ion-accumulation zone, on the other hand, shifts higher-order radial modes ($l \geq 2$) in the middle annular zone, which is located 2.5-3 μm below the surface of the glass hetero-fiber, and consequently lowers the evanescent field and modal excitation.

The optical structures in question have been rigorously simulated using the finite element method (FEM) (COMSOL Multiphysics) to compare the optical characteristics of the poled glass cavity to those of the pristine one. This has further supported our assumption.

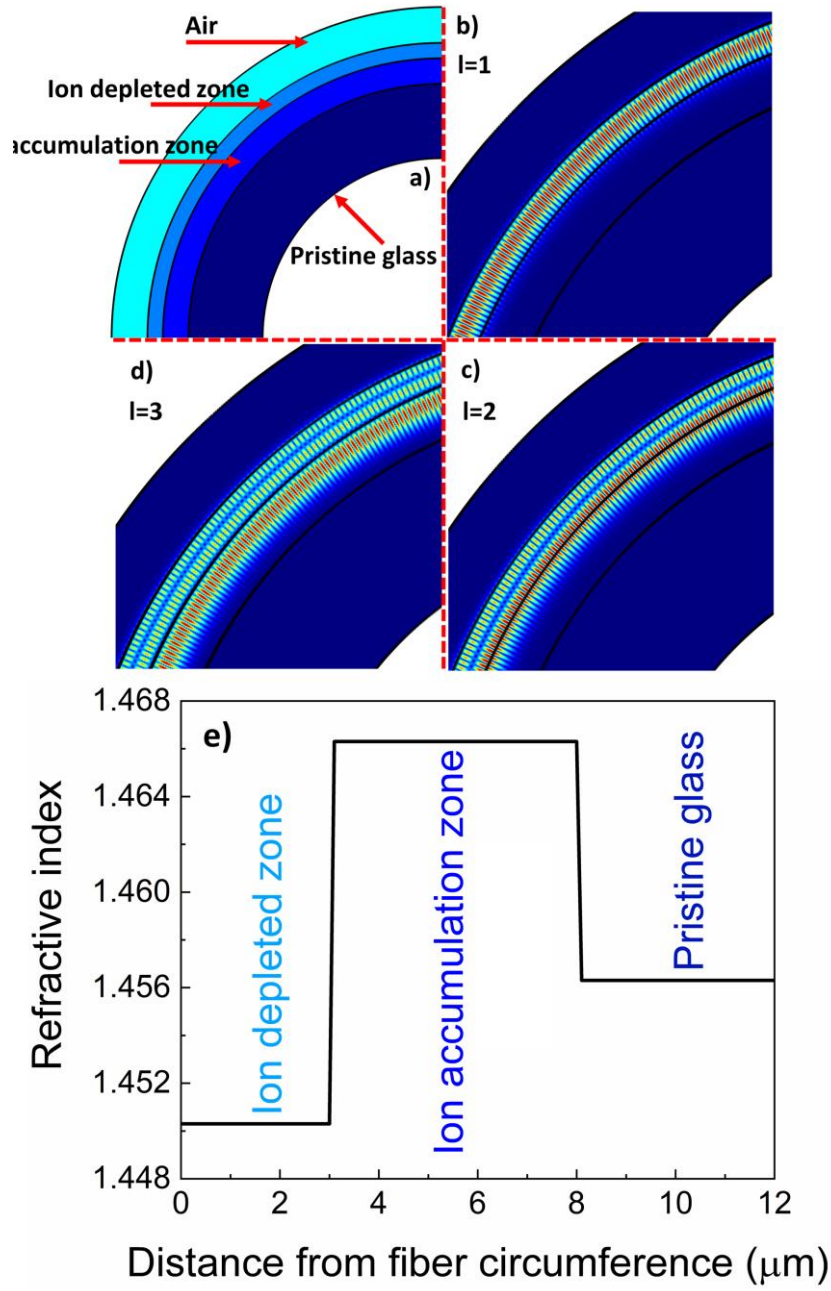


Figure 4.12 (a) Schematic of the resonant thermally poled cavity under study. (b-d) Normalized electric field intensity (V/m) WGMs modal results from a Finite element method program for TE Modes for azimuthal number $m=327$ and radial order $l=1$, $l=2$, and $l=3$, respectively. (e) Refractive index spatial distribution was used in the FEM simulation.

We carried out two types of simulations: eigenvalue simulations to investigate the WGM resonances supported by the cavity and harmonic propagation simulations with excitation to calculate transmittance spectra for horizontal and vertical polarizations and compare them with the experimental data. The geometry considered in the simulations is depicted in Figure 4.12a (one quadrant shown); it is the 2D representation of the cavity, justified by the homogeneity along the z -axis ($d/dz=0$). The dimensional parameters used were $r_{\text{fiber}}=57.5\text{ }\mu\text{m}$, $r_{\text{ID}}=54.5\text{ }\mu\text{m}$, and $r_{\text{IA}}=49.5\text{ }\mu\text{m}$. Its refractive indices are as follows: $n_{\text{ID}}=1.4503$, $n_{\text{IA}}=1.4663$, and $n_{\text{pristine}}=1.5563$. The distribution of the different refractive index zones in a hetero-fiber glass cavity that has been thermally poled for 75 minutes is depicted in Fig.4.12e. This refractive index profile was constructed using the ξ factor determined from the EDX ion density data and the FSRs for poled and unpoled cavities. Results of the eigenvalue simulation for the poled cavity (75 minutes) are depicted in Figures 4.12(b)-(d). Modes of first-, second-and third-radial-order are shown; they are associated with a different mode extent along the radial direction. According to Figure 4.11b, the field distribution ($|\text{Re}E_z|$) of the first-order radial mode ($l=1$) extends predominantly over the lower refractive index ion-depleted zone, which is expected to lower the effective index of the mode and shifts its spectral resonance position to the blue.

On the other hand, modes with $l \geq 2$ extend their overlap over the higher refractive index ion-accumulation zone. A strong overlap of the inner, higher-intensity lobe of the 2nd order ($l=2$) radial mode (Fig.4.12c) with the higher refractive index ion-accumulation zone is observed, which is expected to increase its effective index and red-shift the spectral resonance position of the waveguide. Figure 4.13 (a) and (c) show these relative spectral shifts for pristine and poled glass hetero-fiber WGM resonances. $\text{TE}(l, m)$ resonances are “blue-shifted” while $(\text{TE}2, m)$ resonances are “red-shifted” in very good agreement with the trends observed in the experimental data shown in Figure 4.6-4.8. For the TM polarized modes, similar conclusions are reached.

Table 4.1: Experimental vs. Comsol spectral data of specific WGMs before and after thermal poling

Experimental Data		
Radial order	1 st	2 nd
Unpoled Hetero-fiber	TE _{1,326} :1555.25 nm	TE _{2,316} :1557.24 nm
Poled Hetero-fiber	TE _{1,326} :1549.99 nm	TE _{2,316} :1558.56 nm
WGM Shift	Blueshift: -5.26 nm	Redshift: 1.32 nm
COMSOL Data		
Radial order	1 st	2 nd
Unpoled Hetero-fiber	TE _{1,326} :1555.97 nm	TE _{2,316} :1557.58 nm
Poled Hetero-fiber	TE _{1,326} :1549.92 nm	TE _{2,316} :1558.53 nm
WGM Shift	Blueshift: -6.05 nm	Redshift: 0.95 nm

Table 4.1 compares the experimental wavelength values of two modes (different radial order) versus the corresponding Comsol data obtained before and after thermal poling to provide a more detailed description. As can be seen, the differences in the blue and red shifts between experimental and simulation data are congruent and less than 1nm. It has also been demonstrated, by comparing Figures 4.13 (a) and (c), that the 2nd (TE₂, m) and 3rd (TE₃, m) order-radial modes are suppressed in the poled glass hetero-fiber, as evidenced by the shallower transmission minima. In contrast, the transmission depths, FSR, and linewidths (quality factors) of the first-radial-order modes (TE₁, m) are largely unaffected, which is in excellent agreement with the experimental results shown in Figures 4.6(a) and 4.8. (a). The TM modes exhibit similar “spectral cleaning” and agreement with the experiment.

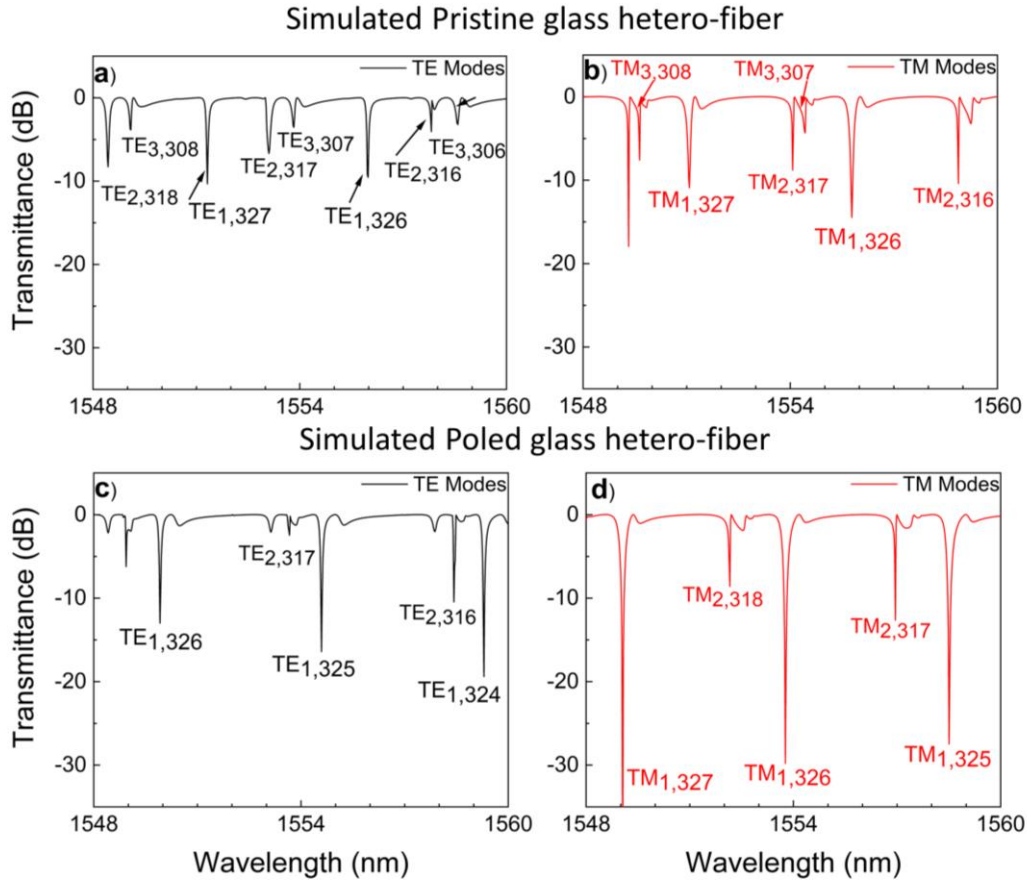


Figure 4.13 Finite element method WGMs spectral results for TE and TM polarization states, unpoled (a, b) and poled glass hetero-fiber (c, d).

Additionally, we calculated the energy fraction stored for each radial WGM order (l) in the air-extended evanescent wave for both poled and unpoled hetero-fibers, validating our experimental results (See Table 4.2 and 4.3).

TABLE 4.2: The normalized fractional energy stored outside the resonator (in the air) for WGMs with different radial orders of TE polarization (l) in thermally poled and unpoled hetero-fibers.

Radial order	Unpoled hetero fibers (%)	Poled hetero fibers (%)	Fractional change (%)
$l=1$	0.41	0.41	-0.25
$l=2$	0.45	0.33	-25.67
$l=3$	0.49	0.48	-1.63

TABLE 4.3: The normalized fractional energy stored outside the resonator (in the air) for WGMs with different radial orders of TM polarization (l) in thermally poled and unpoled hetero-fibers.

Radial order	Unpoled hetero fibers (%)	Poled hetero fibers (%)	Fractional change (%)
$l=1$	0.79	0.79	-0.73
$l=2$	0.78	0.58	-25.82
$l=3$	0.81	0.79	-1.57

As illustrated in Figures 4.6 and 4.7, the poling process reduces the depth (contrast) of the resonances (apart from the spectrum cleaning). However, this behavior is not a fundamental limitation of our approach. As demonstrated in Table II above, one of the effects of poling is that it reduces the energy stored outside the resonator (i.e., in the evanescently decaying tail), meaning that the coupling coefficient with the tapered fiber decreases. This can lead to better contrast for the resonances if the initial (unpoled) resonator-waveguide system is over-coupled (coupling loss is more significant than intrinsic loss) [125]. This is indeed the case in the simulations (Fig. 4.13). With decreased coupling coefficient due to poling, the originally over-coupled system approaches critical coupling (the condition coupling loss equals intrinsic loss) resonance depth is improved. However, in the experiment, the system turns out to be initially under-coupled. As a result, when the coupling coefficient decreases with poling, the system drifts further away from critical coupling and reduces the resonance depth. This difference is attributed between simulation and experiment to scattering loss in the coupling region present only in the experiment (non-ideal touching geometry of fiber and resonator, surface roughness, etc.). Tables 4.2 and 4.3 show that the energy stored in the evanescent field of the thermally poled samples' TE and TM radial order modes is less than that of the pristine hetero-fiber. The 1st and 3rd radial order modes undergo small changes ($\leq 1.6\%$) in their evanescent energy fraction for the thermally poled sample compared to the

pristine hetero-fiber. Therefore, they show a negligible change in their coupling constant with the excitation fiber and transmission depth. The 2nd radial order mode, on the other hand, exhibits a much more significant reduction of the order of 25% in their evanescent energy fraction, which results in a substantial change in their coupling constant with the excitation fiber and a large reduction in the transmission depth (effective “spectral cleaning”).

4.7 Thermal poling results without implementing nitrogen flow

To better understand the impact of nitrogen flow throughout the process, some experiments were conducted according to the experimental procedure described in subchapter 4.5, however, without using the nitrogen flow (open anode). Fig.4.14 illustrates how thermal poling affects the WGM spectra for each polarization component, with modal (loaded) Q-factors reaching 5.1×10^4 for both polarizations. Various thermal poling times were tried, but the one depicted in Figures 4.14c, d corresponds to the 75-minute poling time. No spectral clean-up was observed in contrast to the previous chapter’s thermal poling with N flow experiments.

There was no evidence of compression or extinction of the radial higher-order modes. According to the results presented in Figures 4.14a,b, the FSR of the $l=1$ radial modes of the pristine hetero-fiber was 4.99 nm, which is slightly larger than the value obtained in previous experiments (4.62nm). There are minor differences in fiber diameter between different glass fiber samples, which is responsible for this discrepancy. After 75 minutes of thermal poling, the FSR of the $l=1$ radial modes decreases to 4.98 nm (Fig.4.14 c,d), indicating a decrease in the refractive index of the glass hetero-fiber in the presence area of the specific modes described in the previous chapter. This FSR reduction is less than the ambient (N flow) atmospheric conditions. An approximate 2.5×10^{-3} decrease in refractive index in the ion-depleted region is formed due to this procedure. This

refractive index reduction value is nearly one-third of the value observed during the process with N flow at the same thermal poling time scale because of the ionic species that have entered the ion-depleted region during the thermal poling procedure.

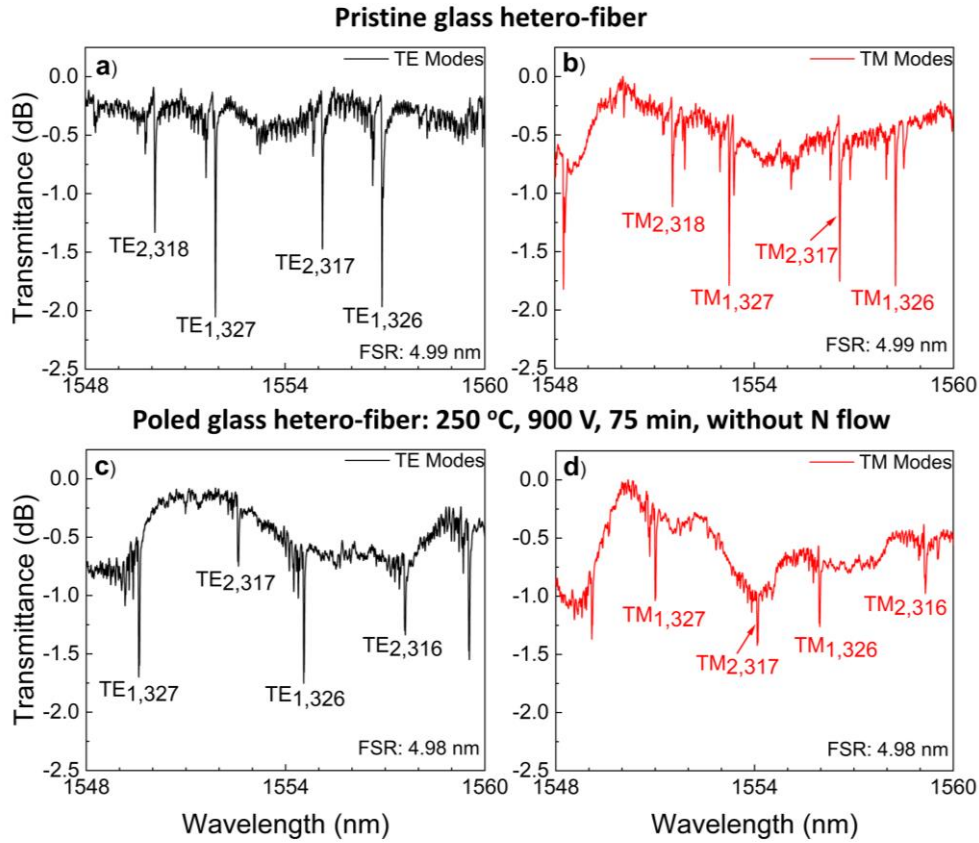


Figure 4.14 Experimental WGMs spectral results for both polarization states, TE Modes (black) and TM Modes (red), for pristine glass hetero-fiber (a,b) Experimental WGMs spectral results for both polarization states, TE Modes (black) and TM Modes (red), for poled glass hetero-fiber for 75 minutes poling time without N flow

A second significant difference between the two electrode configurations (closed and open) is that the second one blue-shifts the entire WGMs spectrum regardless of the radial order. This indicates that the refractive index step profile after the thermal poling procedure without N flow differs from the step profile after the N flow procedure described in the previous chapter. Specifically, the refractive index is smaller in the region close to the anode side than the initial unpoled optical fiber; however, this refractive index state goes deeply into the

glass ($\sim 6 \mu\text{m}$) compared with the nitrogen-poled optical fiber. Table 4.4 summarizes the mode shifts after the thermal poling procedure for specific TE modes.

Table 4.4: Experimental spectral data of specific WGMs before and after thermal poling

Experimental Data		
Radial order	1 st	2 nd
Unpoled Hetero-fiber	TE _{1,327} :1551.91 nm	TE _{2,317} :1555.13 nm
Poled Hetero-fiber	TE _{1,327} :1549.59 nm	TE _{2,317} :1552.67 nm
WGM Shift	Blueshift: -2.32 nm	Blueshift: -2.52 nm

This photonic behavior can be explained by considering the electric field distribution in the subanodic depleted layer for a soft glass modeled by Dussauze et al. [109] (Fig.4.15). According to Figure 4.12, the radial order modes with $l=3$ extend to $6 \mu\text{m}$. Consequently, the first three radial order modes ($l \leq 3$) realize the same refractive index in the case of thermal poling in the air atmosphere. Therefore, the electric field distribution and refractive index profile in the air-poled soft glass near the anode side show a shallower profile and more spatially extended, reaching $6 \mu\text{m}$ from the anode following the simulation above.

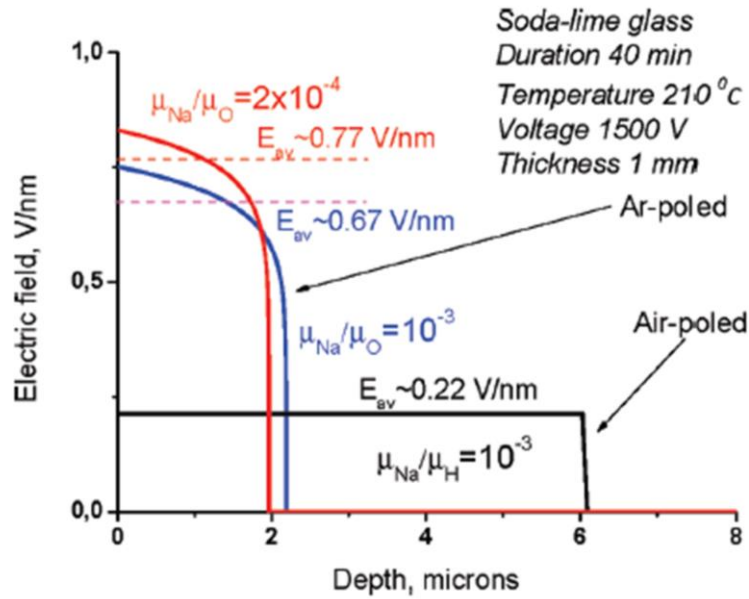


Figure 4.15 Modeling of the electric field distribution in the subanodic depleted layer of poling soda-lime glass with open (air-poled glass) and blocking (Ar-poled glass) anodes [109].

With non-linear 1028nm laser microscopy, we could trace the SHG signal caused by ion displacement in the poled hetero-fiber that was not subjected to N flow. Figure 4.16 shows an SHG image of the hetero-fiber cross-section illustrating the spatial distribution of second-order nonlinearity for a cavity poled without nitrogen at 250 °C for 75 minutes with a negative voltage of 900 V applied to the central wire. The image has been processed with ImageJ so to visualize the faint signal from the circumference of the optical fiber.

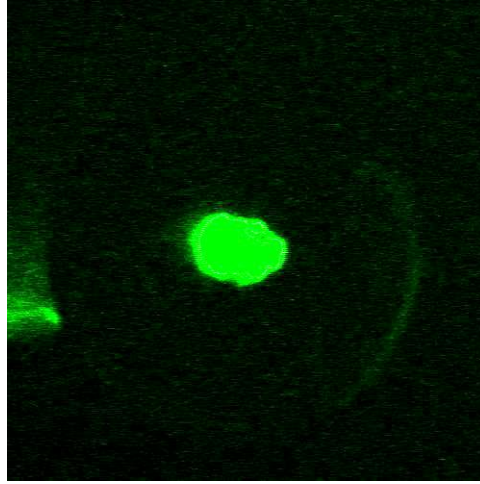


Figure 4.16 SHG processed image with ImageJ obtained from a poled hetero-fiber WGM cavity cross-section for 75 min poling time without nitrogen flow

It can be seen from the figure above that the SHG signal from the annular green ring around the hetero-fiber glass cavity's outer circumference is weaker than that presented in Figure 4.5a. The boundaries of the locally introduced non-linear dielectric susceptibility $\chi^{(2)}$ ring were unclear, so it was impossible to measure the dimensions of the ring.

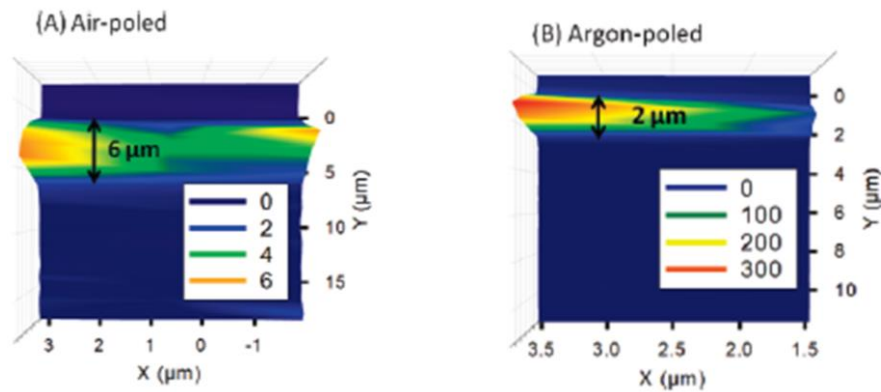


Figure 4.17 Measured on the cross-sections of soda-lime glasses that were air-poled (A) and argon-poled (B), the SHG signal was determined. The SHG signal value is expressed in arbitrary units; the position $Y=0$ corresponds to the anode side, while the positive values of Y are directed toward the cathode side [109].

The reduction of the SHG signal and the widening of the $x^{(2)}$ ring in thermal poling in atmospheric air conditions was also observed in other works (Fig. 4.17) [109].

As a result, the experiments with atmospheric air conditions were not continued because they did not reveal any interesting photonic behavior of WGMs in the process.

4.8 Chapter conclusions

Chapter 4 delves into an analysis of borosilicate glass optical fibers subjected to radially aligned thermal poling and subsequently scrutinizes the whispering gallery mode resonances within optical hetero-fibers. The research outcomes are systematically classified based on the nature of the anode implemented (either with or devoid of nitrogen flow). It was observed that the refractive index profile in proximity to the anode side was influenced by the kind of anode utilized, leading to variations in the attenuation of whispering gallery mode resonances. Regarding thermal poling in conjunction with nitrogen flow, the disruption of the glass network's macroscopic centrosymmetric symmetry adjacent to the anode side was affirmed via SHG microscopy. Furthermore, we employed EDX spectroscopy to discern the ionic spatial distribution in thermally poled hetero-fibers, establishing a distinctive refractive index profile near the anode side. This refractive index profile lessens the coupling coefficient pertinent to the radial higher-order modes, culminating in a spectrum "purification" for poling durations surpassing 75 minutes. Eventually, the spectral findings were validated via the finite element method simulation software Comsol Multiphysics.

Conversely, in the absence of nitrogen flow during the thermal poling process, positive ions are introduced from the ambient atmosphere into the borosilicate glass adjacent to the anode side, resulting in a notable contraction of the ion depletion zone. As a result, a deduced SHG signal was observed from the anode side, and there was no spectral annihilation of WGMs in the higher-order modes.

5 A study of silk fibroin photo-elasticity in whispering gallery modes cavities

This chapter examines the photoelasticity of silk fibroin cavities utilizing whispering gallery mode resonations. The small mode volumes intrinsic to WGMs facilitate illumination of the segmental properties of silk fibroin in its two distinct states, commonly referred to as Silk I and Silk II.

5.1 Silk fibroin

Silk fibroin is derived from the natural silk fibers produced by insects, such as silkworms and spiders. Silk from the silkworm (*Bombyx mori*) and spider silk comprise glycine-rich proteins, but their structures and compositions are distinct [53]. Natural *Bombyx mori* cocoons are primarily composed of two different proteins: SF, which makes up 70–80 weight percent of a cocoon, and sericin, which makes up 25–30 weight percent. The SF consists of α -helices, β -sheet crystals, and random coils assembled by repetitive amino acid sequences using hydrogen bonds, hydrophobic interactions, and van der Waals forces [52]. Because it can potentially trigger immune reactions, sericin is typically removed during the preparation process [126].

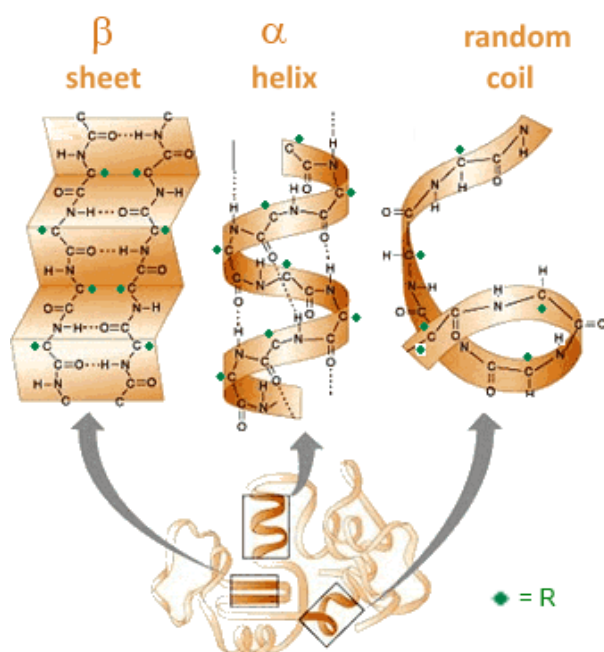


Figure 5.1 A schematic representation of Silk fibroin building blocks [127]

SF has superior biocompatibility and water solubility compared to natural biomaterials. Its biodegradability can be programmed from hours to years by altering processing methods or postprocessing procedures (e.g., water vapor annealing, methanol annealing, and ethanol annealing) to change the content of β -sheet crystals and the degree of organization of noncrystalline domains. Moreover, β -sheet crystals endow SF-based materials with superior mechanical properties (i.e., high strength and good toughness). It has been confirmed that the degradation rate of SF increases with decreasing the content of β -sheet crystals. It is generally accepted that fibroin's ordered and crystalline form is the precursor secondary structure. This structure is thought to transform into the β -sheet structure of Silk II when energy is introduced into the system [128]. The Silk II crystalline domains are the primary stabilizing crosslinks in silk fibers and provide the fibroin with strength, toughness, and resistance to dissolution.

5.2 Methods and experimental setup

5.2.1 Extraction of the silk fibroin

Silk Fibroin (SF) was extracted from row Bombyx Mori cocoons following the original Rochwood's protocol [129]. Cocoons were sliced and boiled in a 0.02 N sodium carbonate (Alfa Aesar) solution for 30 minutes to remove the glue-like cladding of sericin. The degummed fibroin obtained upon separation from sericin was then washed three times in highly pure water for 20 minutes to remove any excess sericin; it was then dried overnight under a hood. In a conventional oven at 60 degrees Celsius, degummed fibroin was dissolved in a 9.3 M lithium bromide (Alfa Aesar) solution for 4 hours, resulting in an amber-colored solution. To remove salts from the solution, it was dialyzed for 48 hours in a dialyzer cassette (Slide-A-Lazer 3.5 KDa) against ultra-pure water using an electrolyte solution. The dialyzed SF solution was centrifuged twice for 20 minutes at 4°C at 9000 rpm to remove any remaining fibroin. An 8% wt was produced and stored at 4°C in the fridge until needed (Fig. 5.2).

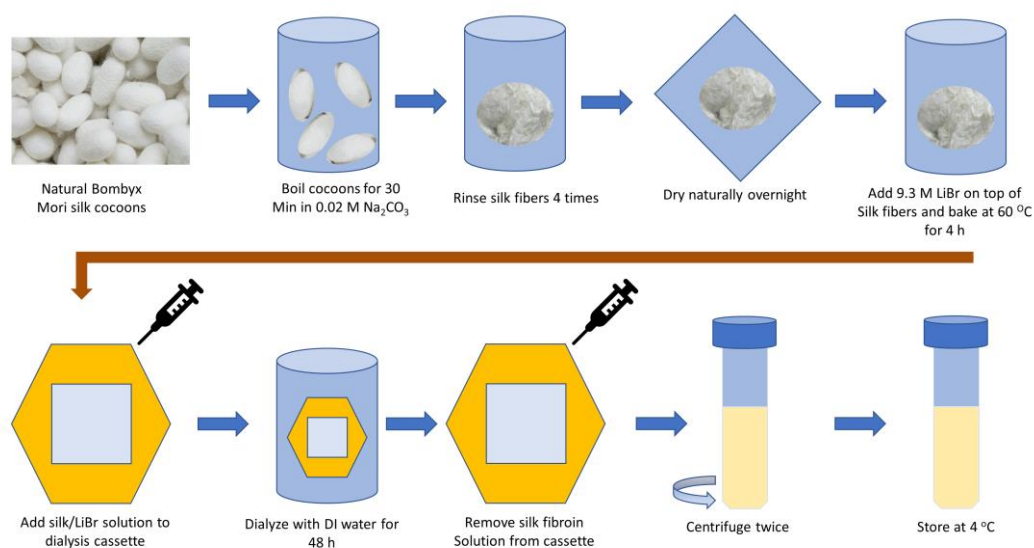


Figure 5.2 Process flowchart for the regenerated silk fibroin solution prepared from natural Bombyx mori cocoons

5.2.2 Silk fibroin cavity preparation for forming WGM resonators

Constructing silk fibroin cavities onto supporting glass optical fibers is necessary so to apply longitudinal strain to the silk fibroin cavities. The optical fibers were the SMF-28 telecommunications fibers with an initial diameter of 125 μm . However, they were reduced to less than 30 micrometers by applying a thermal taper using a GPX-3000 Vytran glass fiber processor (see Fig. 2.7). This was decided because, as the diameter of the optical fiber used for the cavity is decreased, the FSR between modes of the same radial order increases. As a result, the cavity's spectrum is clearer and easier to lock onto a particular mode and track as we apply external strain.

Initial attempts failed because fused silica optical fiber has low hydrophilicity. As a result, large silk droplets in height were formed after instilling the silk with the syringe. After the water evaporated, the cavities' shape was non-symmetric, as seen in Figure 5.3.



Figure 5.3 Optical microscope pictures of non-symmetric silk fibroin cavities formed in non-laser treated optical fiber support

The surface hydrophilicity of these SMF-28 optical fiber tapers was further enhanced by being irradiated with radiation from a 193nm excimer laser [130]. The supporting SMF-28 tapered optical fiber was submerged in deionized water during irradiation. The total energy dose that was dissipated to the fiber was 13 J/cm^2 . A tungsten amplitude mask defined hydrophilic areas of typical lengths

of less than 100 micrometers (Fig. 5.4). After that procedure, the silk fibroin droplets were dispersed onto the hydrophilic optical fiber tapers using a micro-syringe in a vertical placement mode (Fig. 5.5), forming elongated cylindrical cavities with typical lengths 100 μm and diameters of 33 μm .

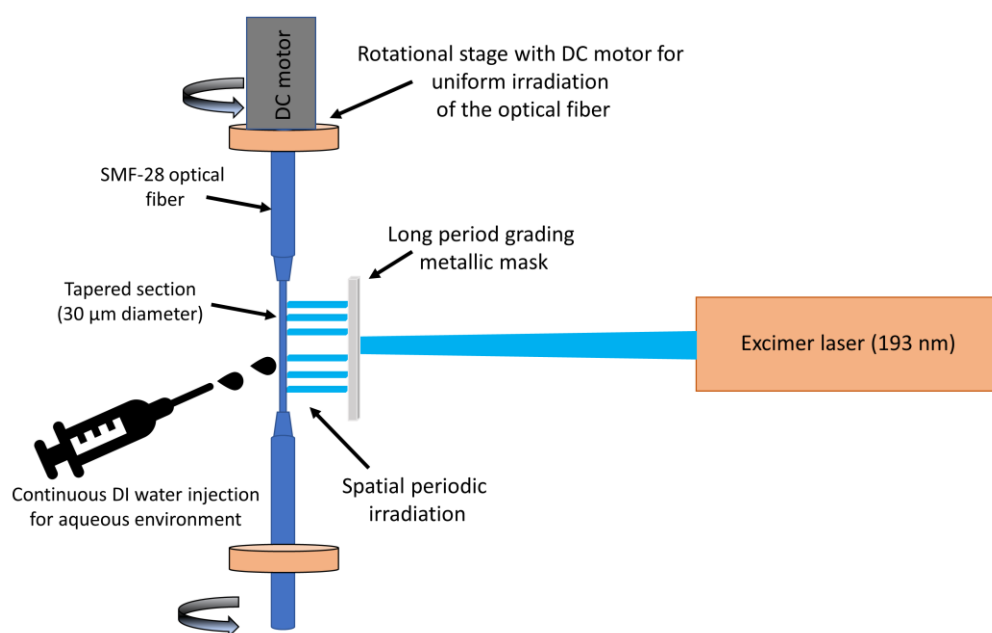


Figure 5.4 Vytran GPX-3000 glass fiber processor for thermally tapering down the optical fibers

More specifically, the glass's surface was coated with a thin silk fibroin overlayer with a thickness of 1.5 μm . These silk fibroin cylindrical cavities were left to dry in the ambient atmosphere thoroughly, so the soft material reached the Silk I amorphous state. Afterward, to transform the cavities into the crystalline Silk II structure, an annealing procedure took place at 180 $^{\circ}\text{C}$ for 10 minutes in ambient air, resulting in a nominal diameter shrinkage with a shrinkage ratio of 0.34%. With an average ramping rate of 8 $^{\circ}\text{C min}^{-1}$, the annealing process required approximately 20 minutes to reach a temperature of 180 $^{\circ}\text{C}$.

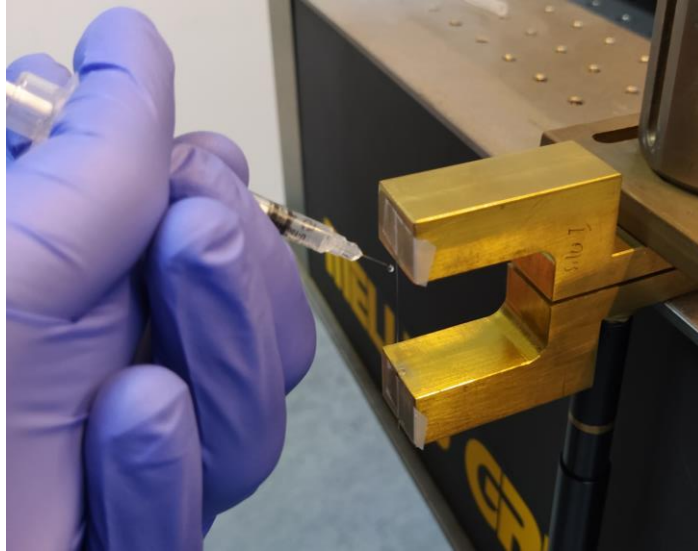


Figure 5.5 Silk fibroin injection on the surface of SMF-28 tapered optical fibers after UV irradiation procedure using a syringe.

5.2.3 Experimental setup

In Figure 5.6, the experimental setup used for the spectral characterization of whispering gallery mode resonance within the silk fibroin cavities is depicted. To suppress higher-order WGM excitation and thus obtain a few notch spectrum [131], a tapered optical fiber with a diameter of $2.2\ \mu\text{m}$ was selected to excite the WGMs within the silk fibroin optical cavity proximity mode. Light from a superluminescence diode was coupled into the excitation optical fiber taper, while the WGM spectral signature was traced through the same fiber using an optical spectrum analyzer.

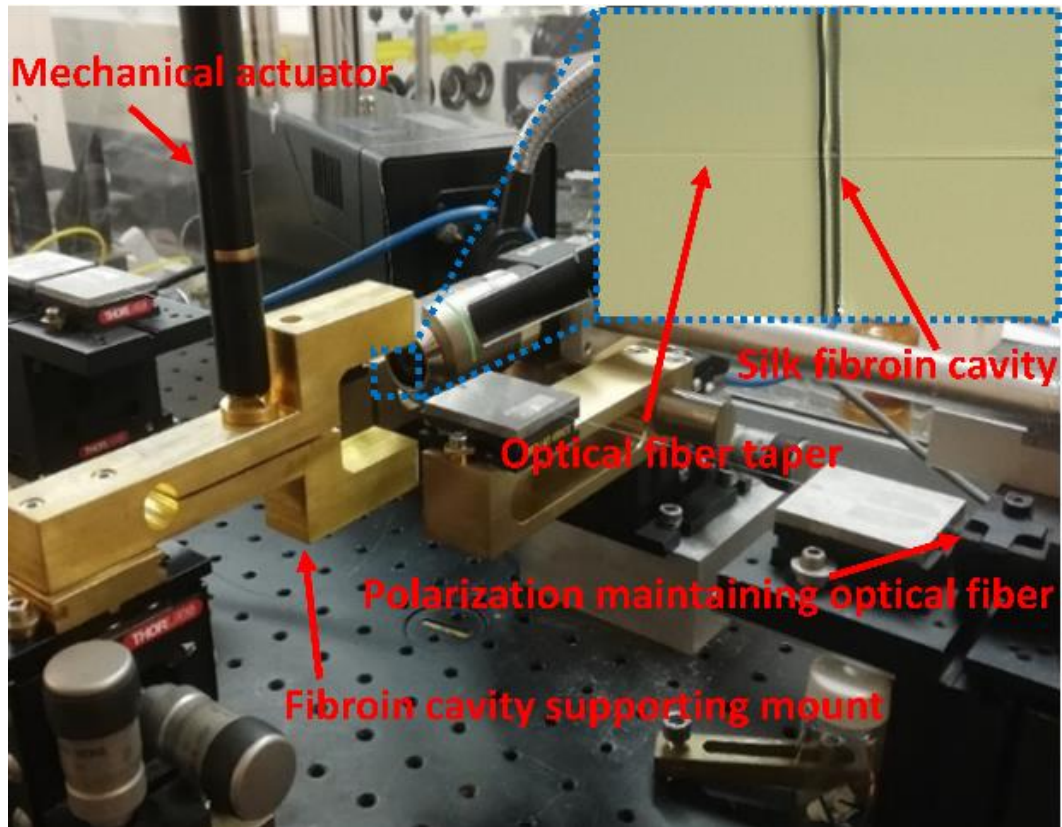


Figure 5.6 The experimental setup for the whispering gallery modes experiments measured the photoelastic properties of silk fibroin cavities. The silk fibroin cavity and the optical fiber taper that injects light (through the evanescent field) inside the cylindrical resonator are depicted in an inset image produced by a camera that uses CMOS technology.

We used a broadband lamp with a CMOS sensor-based camera with a 20x magnification objective lens for the imaging. The TE and TM analyses both used a polarization-maintaining optical fiber.

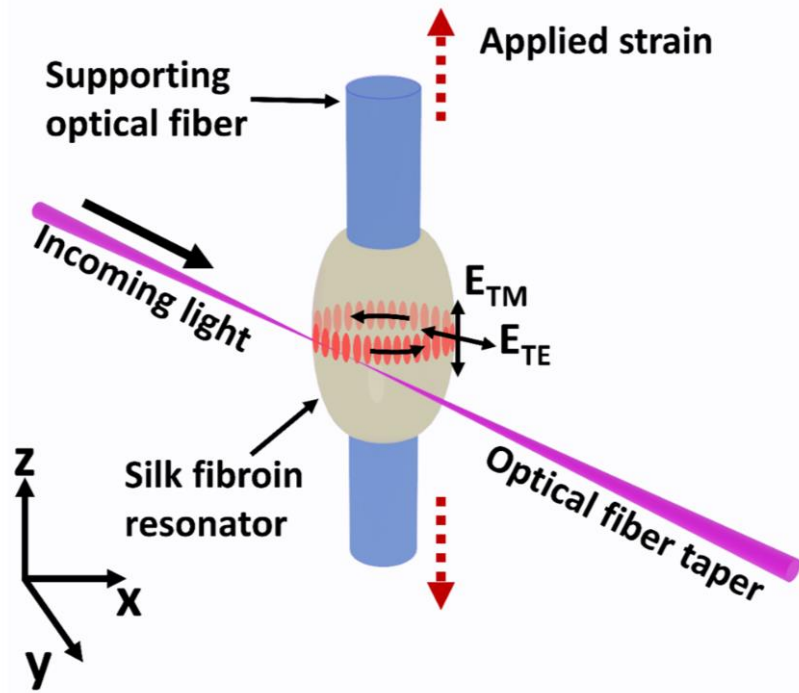


Figure 5.7 Sketch of the experimental apparatus used to characterize the silk fibroin resonating cavities spectrally

The tapered optical fiber with a diameter of 30 μm ensures a linear material response by allowing for the controllable application of minimal strains along the longitudinal axis of the supporting microfiber onto the cavity. Components of the tapered optical fiber-silk fibroin cavity were mounted on a bronze fork using UV glue, with the ability to apply strain under precise control. A DC servo motor actuator was used to precisely elongate the optical fiber with the silk fibroin cylinder (Fig. 5.6). The minimum achievable step for the micrometric actuator straining the brass fork was 0.2 micrometers. An optical spectrum analyzer (ANDO AQ6317B) was used for the signal recording. A polarization-maintained optical fiber was used to separate the TE and TM modes supported by the silk fibroin resonator. The strain exerted onto the 30 μm diameter taper section was calibrated using WGM resonance for TE and TM polarization while assuming the Pockel's coefficients holding for silica glass at the propagation

wavelength. Figure 5.8a presents scanning electron microscope (SEM) images illustrating a silk fibroin cavity, while Figure 5.8b shows its cross-sectional view.

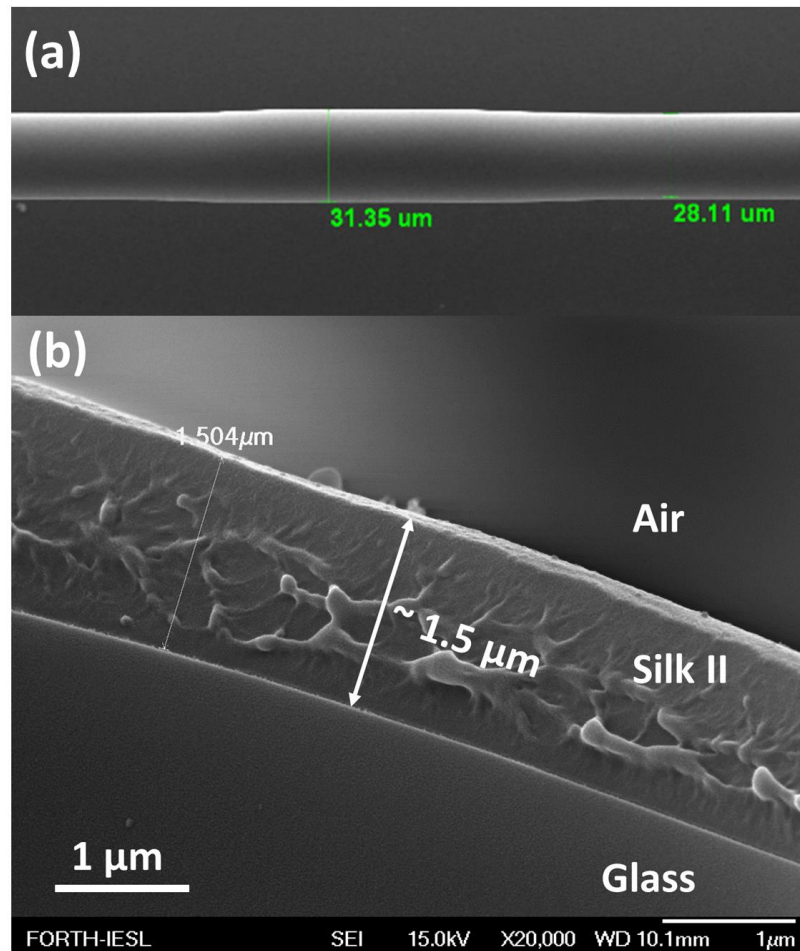


Figure 5.8 (a) SEM image of a typical silk fibroin cavity formed on a silica optical fiber taper to achieve Silk II structure after annealing. (b) Transversal SEM picture of a radial cross-section of a $\sim 1.5 \mu\text{m}$ thick Silk II fibroin film overlaid onto an underlying $\sim 87 \mu\text{m}$ -diameter silica glass optical fiber taper.

5.2.4 Brillouin Light Scattering measurements

We used Brillouin light scattering (BLS) to determine the mechanical properties of Silk I and II by measuring the velocity of longitudinal (c_L) and transverse (c_T) gigahertz (GHz) acoustic waves. The experimental apparatus, shown in Figure

5.9(a), can be used to measure BLS in 90A or backscattering geometry. In 90A geometry, the probed GHz waves have a wavevector $q = (4\pi/\lambda) \sin 45^\circ = 16.7 \mu\text{m}^{-1}$, where $\lambda = 532 \text{ nm}$ is the laser wavelength. In backscattering BLS the probed wavevector $q = 4\pi n/\lambda$, where n is the refractive index of the material. The samples for BLS in 90o transmission (90A) geometry consisted of smooth, homogeneous films with a thickness of ca. $13.5 \mu\text{m}$ on a 1 mm-thick soda lime glass slide. All the measured BLS spectra are better represented with Gaussian peak profiles.

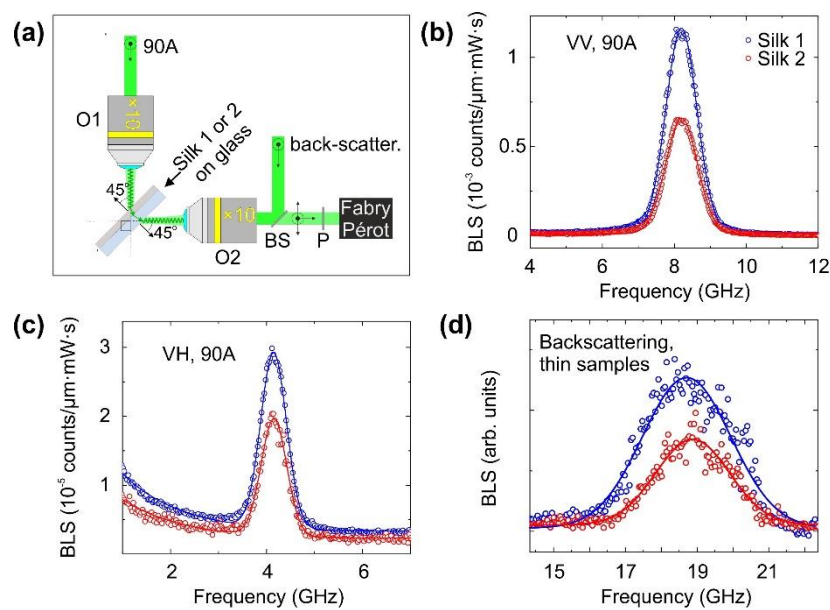


Figure 5.9 (a) The experimental setup used to measure Brillouin light scattering spectra for Silk 1 (blue) and 2 (red) in (b) 90o transmission geometry with VV polarization, (c) 90o transmission with VH polarization, and (d) thin samples resembling the WGM experiment in backscattering geometry with VV polarization. The spectra are represented with Gaussian peak profiles (solid lines). The spectra in (b) and (d) are normalized with the incident power, the exposure time, and the film thicknesses (13.5 and $13.3 \mu\text{m}$ for Silk 1 and 2, respectively).

In 90A with VV polarization (Fig. 5.9(a)), the frequency of longitudinal acoustic waves is $f_{L,1} = 8.19 \text{ GHz}$ and $f_{L,2} = 8.2 \text{ GHz}$, and the velocities $c_{L,1} = (3083 \pm$

10) m/s and $c_{L,2} = (3086 \pm 10) m/s$. In VH polarization (Fig. 5.9(b)) we probe transverse acoustic waves with a frequency $f_{T,1} = 4.15$ GHz and $f_{T,2} = 4.16$ GHz. The transverse velocities are $c_{T,1} = (1561 \pm 10) m/s$ and $c_{T,2} = (1563 \pm 10) m/s$ for Silk 1 and 2, respectively. The densities of Silk 1 and 2 are $1400 kg/m^3$ and $1450 kg/m^3$. The shear moduli ($G = \rho c_T^2$) are $G_1 = (3.41 \pm 0.05) GPa$ and $G_2 = (3.54 \pm 0.05) GPa$. The Poisson ratio $\nu = (1 - 0.5 c_L^2/c_T^2)/(1 - c_L^2/c_T^2) = 0.328$ for both samples. Young's moduli are found from:

$$E = \frac{(1 + \nu)(1 - 2\nu)}{1 - \nu} \rho c_L^2 \quad (5.1)$$

and they are equal with $E_1 = (9.05 \pm 0.05) GPa$ and $E_2 = (9.40 \pm 0.05) GPa$. The thick samples were also studied with backscattering BLS, from which we can extract the refractive index with the relationship $n = \sqrt{2} f^{BS} / 2 f^{90}$. At 532 nm wavelength, the measured values are $n_1 = 1.593$ and $n_2 = 1.596$. In addition to the thick samples for 90A measurements, we have prepared thin films of silk I and II using the processes described above onto CaF_2 substrates, which resemble the samples used in the WGM experiment. The thinner silk films could be measured with BLS in backscattering geometry (Fig. 5.7(c)), from which we extract the Young moduli of Silk 1 and 2 equal with $E_1 = (9.08 \pm 0.05) GPa$ and $E_2 = (9.90 \pm 0.05) GPa$, respectively.

In addition to the mechanical properties, BLS can be used to derive the relative values of the photoelastic constants in Silk 1 and 2. Although the mechanical properties are identical, the strain-induced optical anisotropy per optical axis of Silk 1 is significantly higher than Silk 2 (see the intensities in Figures 5.9(b) and (c)). The BLS intensity (I) for longitudinal waves and VV polarization is:

$$I^{VV} \propto \frac{|p_{12}|^2}{c_L^2}. \quad (5.2)$$

The BLS intensity for transverse waves and VH polarization is:

$$I^{VH} \propto \frac{|p_{44}|^2}{c_T^2} \frac{n^2 - \sin^2 45^\circ}{n^2} \quad (5.3)$$

where n is the refractive index and the p_{11} and p_{12} are photoelastic constants. Additionally, for isotropic solids we have $p_{44} = (p_{11} - p_{12})/2$. For the depolarization ratio we then have:

$$\frac{I^{VH}}{I^{VV}} = \left(\frac{f_L}{f_T}\right)^2 \frac{|p_{44}|^2}{|p_{12}|^2} \frac{n^2 - \sin^2 45^\circ}{n^2} \quad (5.4)$$

where f_L and f_T are the observed frequencies of the LA and TA phonons. From the relationship for I^{VV} we get $p_{12}^{silk\ 1}/p_{12}^{silk\ 2} = 1.32$. From I^{VH} we get $p_{44}^{silk\ 1}/p_{44}^{silk\ 2} = 1.23$. Finally, from I^{VH}/I^{VV} and all the above we get $p_{11}^{silk\ 1}/p_{11}^{silk\ 2} = 1.31$.

5.2.5 Calibration of the strain fork apparatus

As mentioned, the silk fibroin cavities were constructed onto the tapered optical fibers (TOF), with the tapered optical fibers constituting a stable support beam for exerting longitudinal strain. After drop-casting to create the silk fibroin

WGM cavity (sub-chapter 5.2.2), the TOFs fibers were mounted on a bronze fork using UV glue. Because the TOFs varied in diameter along the length of the metal fork, it was not easy to calculate the applied strain transferred to the silk fibroin cavities. The TOF waist was approximately 30 μm in the narrowest area, which increased as we moved toward the ends. Inscribing a fiber Bragg grating in the narrowest area and observing the resulting spectral shift as we strain the grating is the only way to accurately measure the strain applied in a given optical fiber taper. The strain was measured using a highly photosensitive optical fiber (GF1b). Initially, the spectral shift-strain relationship for the 30 μm optical fiber was determined. The experimental setup utilized is depicted in Figure 5.10. The 30 μm region of the TOF was glued on two XYZ micrometric mounts having in the middle an FBG inscribed. As a result, the strain is applied only in the 30 μm diameter area.

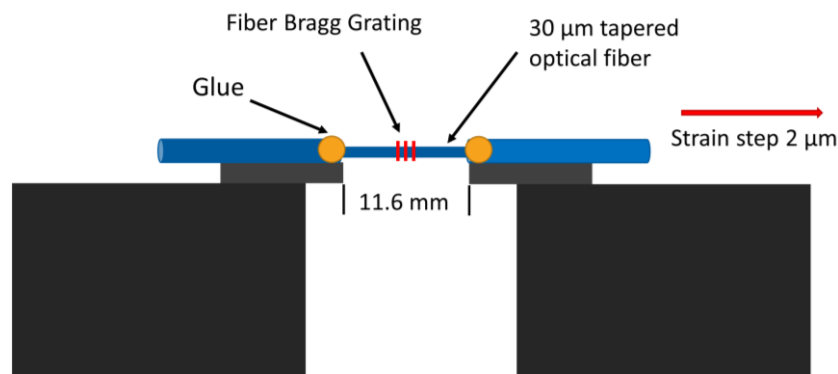


Figure 5.10 The experimental apparatus for determining the strain-optic coefficient of a 30 μm diameter GB1b optical fiber

We can determine the applied strain by knowing the initial length (11.6 mm) of the 30 μm diameter optical fiber and using micrometric steps of 2 μm each. From the mathematical relationship of strain, each step is $\varepsilon = \frac{\Delta L}{L} = \frac{2}{11.600} = 172 \mu\varepsilon$. The spectral response as we apply the strain is depicted in figure 5.11.

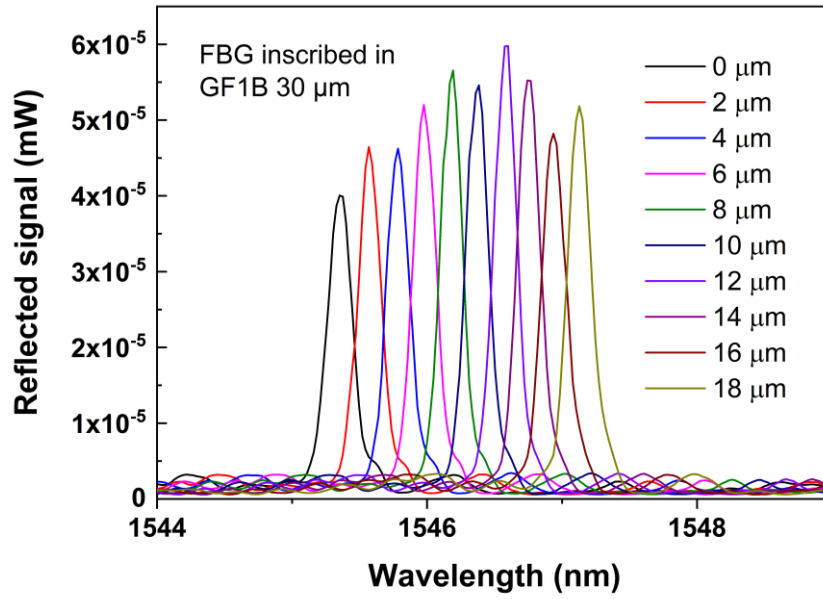


Figure 5.11 FBG spectral shift vs. applied strain

The 30 μm diameter GF1B optical fiber's strain-optical coefficient is determined by the wavelength shift's slope versus strain (Fig. 5.12).

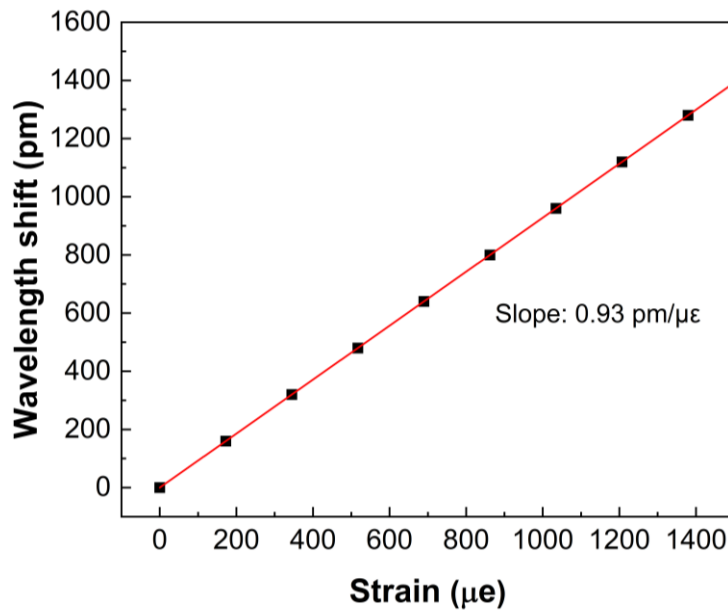


Figure 5.12 FBG spectral shift vs. applied strain

As shown in Figure 5.13, the TOF with an FBG inscription was then mounted on the bronze fork.

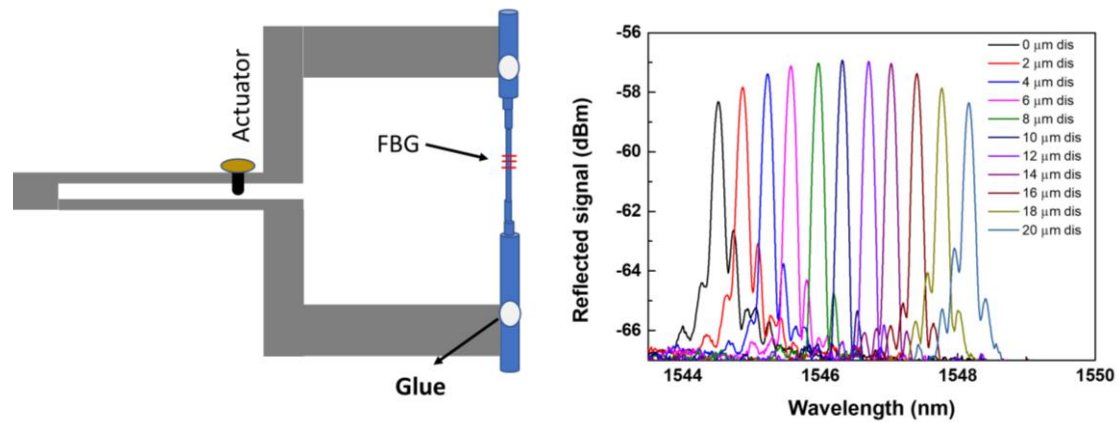


Figure 5.13 A TOF with FBG inscribed mounted on the bronze fork (left side). On the right side is depicted the wavelength shift of the FBG as we apply longitudinal strain.

Using the strain-optical coefficient ($0.93 \text{ pm}/\mu\epsilon$) of the $30 \text{ }\mu\text{m}$ diameter optical fiber and the FBG shift due to the fork strain, we can determine the strains we apply to silk WGM cavities built on the surface of the TOF (Fig. 5.14).

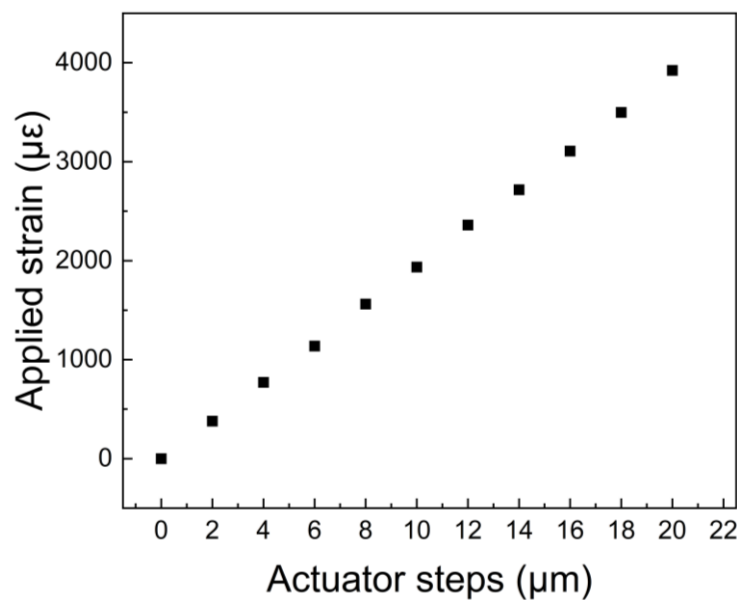


Figure 5.14 Relationship between the actuator steps and applied strain to silk fibroin cavities

5.2.6 Finite element analysis of the component's strain tensors

A mechanical strain simulation was carried out with the assistance of a finite element analysis program that is available commercially. The strain components along the z (the longitudinal axis) and t (transversal x - and y -axes) directions were conducted to determine Pockel's coefficients. In addition, it was essential to specify the component's actual Poisson ratio. We have calculated the value of the material in the form of a thick layer based on BLS measurements. We have already calculated the Poisson ratio based on BLS measurements for the silk fibroin material as a thick layer. We use this value ($\nu=0.328$) as a simulation input. The ε_z strain values used in those calculations were directly deduced from the experimental data available. Because of computational limitations, a scaling down at the length of the supporting optical fiber beam was made, reducing its total length from 37.5 mm to 400 μm . This reduction was made without altering the length of the silk fibroin cavity, which was maintained at 100 μm . The other geometric dimensions are the same as in the previous section for the silk cavity and the supporting glass beam. The distribution of strain components for Silk I is presented in Figure 5.15.

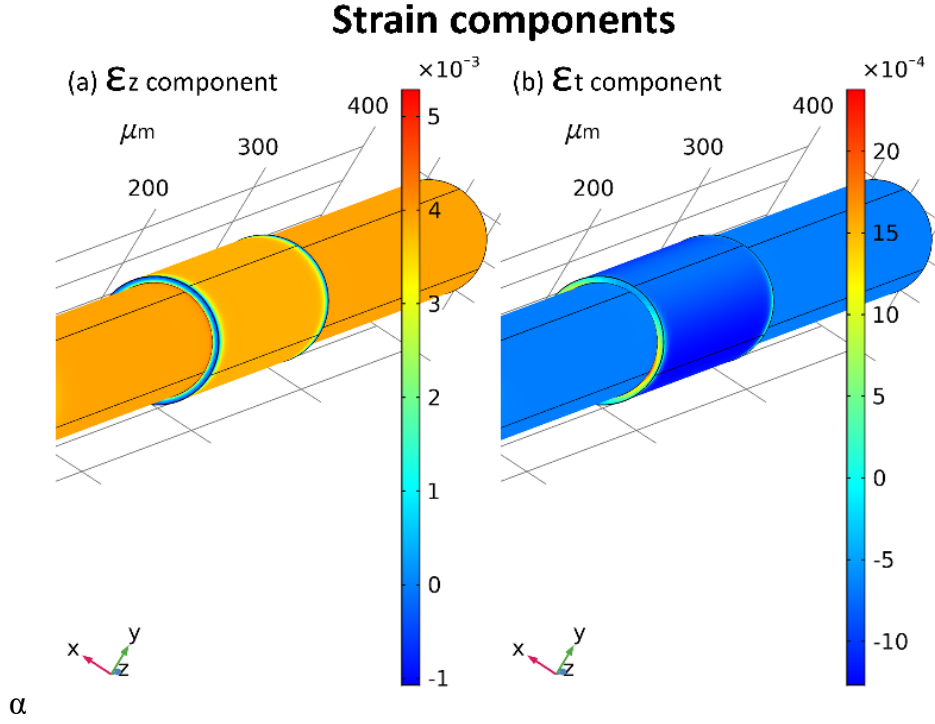


Figure 5.15 Finite element strain tensor analysis of the Silk I cylindrical shape resonator.

The ϵ_z component (a) represents the strain applied in the long axis of the optical fiber with a 3922 $\mu\epsilon$ strain value. On the contrary, ϵ_t component (b) is the induced strain on the transverse (vertical) axis with an 1118 $\mu\epsilon$ strain value. When applying the formula for Poisson's ratio, $\nu = \epsilon_t / \epsilon_z$, we get the value $\nu = 0.285$.

A mechanical stress simulation was conducted to calculate Young's modulus of the silk-optical fiber component. The dimensions are the same as the previous and the external strain ϵ_z . The Young's Modulus (E) values from BLS measurements were inputs to the finite element analysis program. The output of this simulation is the stress (σ) applied in the Silk cavity. By using the mathematical formula $E = \frac{\sigma}{\epsilon_z}$, we calculated Young's modulus values for Silk I and Silk II. The values are $E = 9.34$ GPa and $E = 9.69$ GPa for Silk I and Silk II. The stress colormap for Silk I is presented in Figure 5.16.

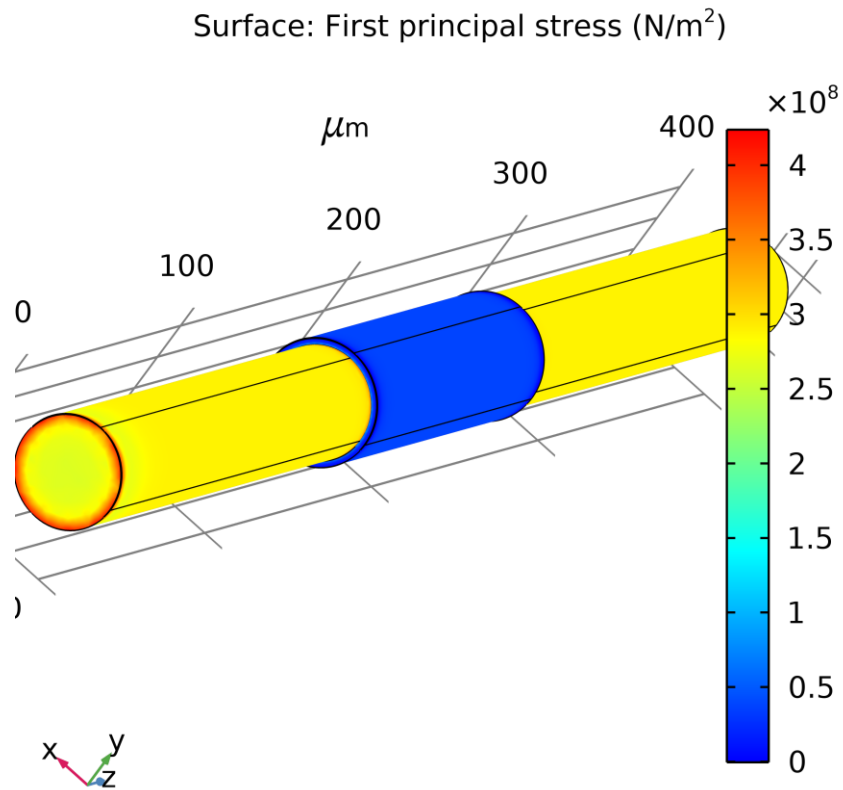
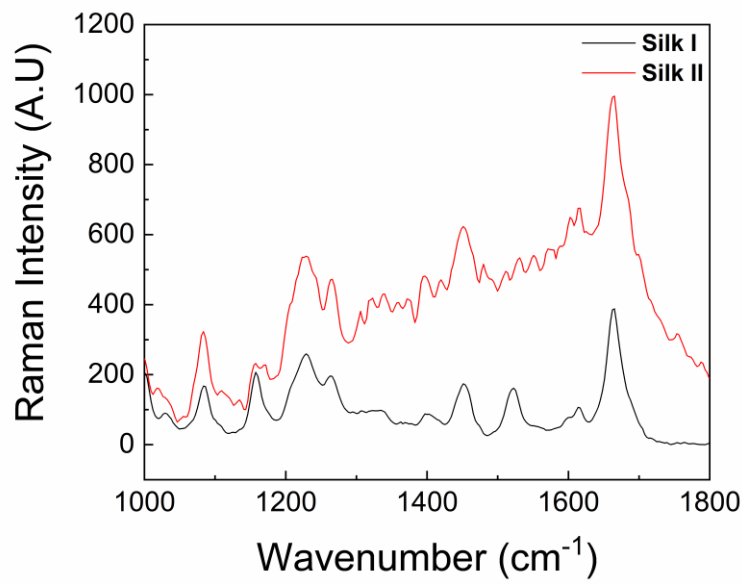


Figure 5.16 Finite element stress analysis of the Silk I cylindrical shape resonator when applying a tensile deformation.

5.2.7 Raman measurements

To investigate the crystallization process from the Silk I to the Silk II structure, Raman Silk I and II measurements were performed using a 532nm frequency double Nd: YAG, operating at 24mW, while focused on samples using an inverse microscope system and a 50X times objective lens. Exposure time was 5sec, while 5 measurements were taken per spot. Raman spectra for a WGM cavity in Silk I and II structure are presented in Figure 5.17.



H

Figure 5.17 Raman spectra of Silk I and II WGM cavities, obtained using 532nm laser excitation.

The peak of interest concerning the crystallization of β -sheets is the 1262cm^{-1} , 1236 cm^{-1} (Amide III), and 1085cm^{-1} , which appear amplified -by a factor of X2- in the Silk II measurement concerning the Silk I [132]. The peak at 1660 cm^{-1} is attributed to the Amide I structure.

5.3 Spectral Results

Several cylindrical cavities of silk fibroin, similar to the one shown in Figure 5.8, were cast from 8wt % silk fibroin aqueous solution using the process described in section 2 characterized by WGM resonance.

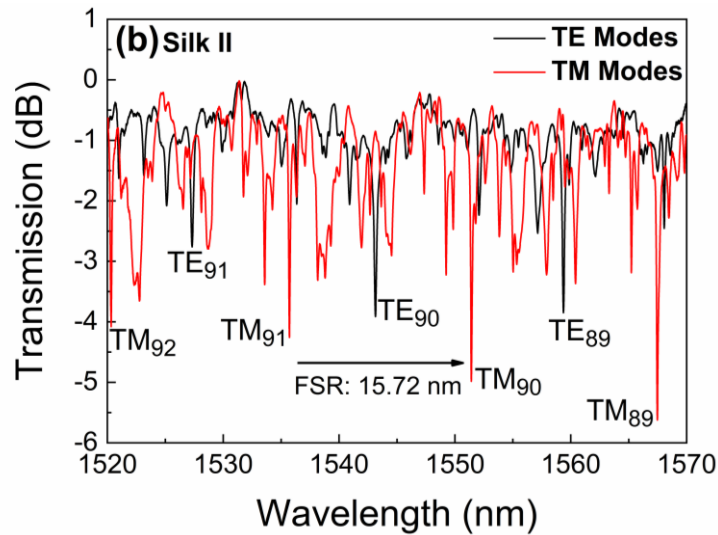
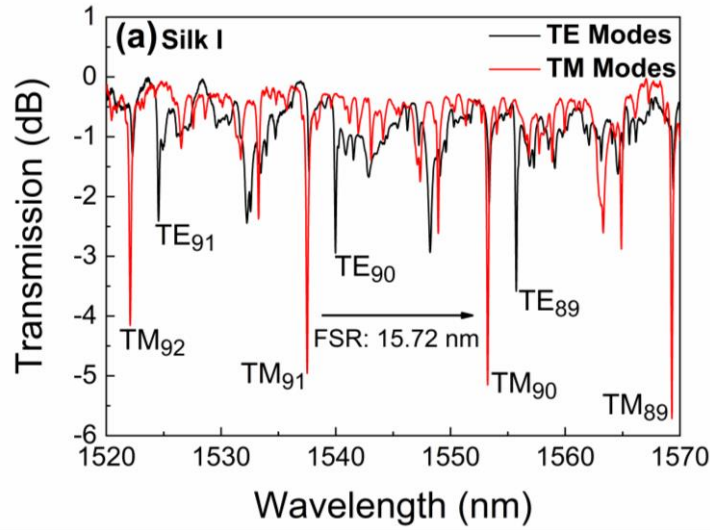


Figure 5.18 Normalized WGM spectra for a 32 μm diameter silk fibroin cavity, for TE (black) and TM (red) polarizations, as cast (Silk I) (a) and after thermal annealing at 180°C (Silk II) (b). The modal allocation presented above refers to modes with radial order $l=1$

Figure 5.18(a) depicts the experimental spectral data of WGM resonances for both polarizations over a broad wavelength range for a silk fibroin resonator as cast (Silk I), and Figure 5.18(b) presents the experimental spectral data of WGM resonances for the same cavity after a thermal annealing process (Silk II); these spectral data refer to the cavity depicted in Figure 5.8. (b). The annealing process is anticipated to improve the homogeneity of silk fibroin and marginally raise its refractive index. Under the assumption of a Lorentzian function fitting, the

quality factors Q measured to be the highest for the cavity shown in Figure 5.8(b) for TM_{89} were 1.35×10^4 for Silk I and 1.61×10^4 for Silk II. These Q -factor values rest below those reported by other groups on Silk I WGM cavities; however, they were measured in closed shape cavities of better radial symmetry than that cast here. The experimental free spectral range (FSR) ($\lambda^2/2\pi rn$) is measured at ~ 15.72 nm for both Silk I & II structure cavities for TM polarization; similar FSR figures hold for TE polarization for pristine (15.44 nm) and anneal (15.85 nm) state. Given that the difference in the TM modes refractive index between Silk I and Silk II structure is typically $\Delta n \sim 0.005$, a radius difference of $\Delta r \sim 5$ nm for the Silk II cavity is deduced because of the annealing process (about 0.34% shrinkage in the radial direction of the cavity). The as-cast (residual) birefringence $\Delta n_{\text{initial}}$ of the Silk I fibroin cavity was estimated from the wavelength positioning of the two polarization notches for a fixed azimuthal/radial order to be $\sim 0.5 \times 10^{-3}$. For the annealed Silk II fibroin cavity, $\Delta n_{\text{initial}} \equiv \Delta n_{\text{TM}} - \Delta n_{\text{TE}} \sim -5 \times 10^{-3}$. Thus, the $\Delta n_{\text{initial}}$ was found to have the opposite sign and a tenfold larger absolute value in Silk II than Silk I. This difference in residual birefringence is attributed to the thermally induced β -sheet formation and their orientation inside the cavity volume of Silk II.

The WGM resonance was described with full-wave eigenvalue simulations using COMSOL Multiphysics (subchapter 5.4). The silk fibroin cavity was considered perfectly cylindrical ($\partial/\partial z = 0$) and treated as a two-dimensional resonant structure in the simulations. This is justified by the slowly varying geometry of the cavity along the z -axis and the fact that modal excitations occur within its middle section, far from side-located turning points. According to experimental data, the free spectral range of first-order radial resonances is 16 nm. Figure 5.8 illustrates mode allocation for the first-radial-order modes under the cylindrical approximation. This mode allocation was accomplished with the help of the finite element analysis program. The figure displays some interstitial spectral features linked to the excitation of higher-radial-order modes. The as-casted (Silk I) fibroin cavity was subjected to controllable longitudinal strain,

and the spectral data of the TE and TM WGM of modal order $m=89$ are presented in Figure 5.19. The corresponding spectra for the Silk II fibroin cavity are depicted in Figure 5.20.

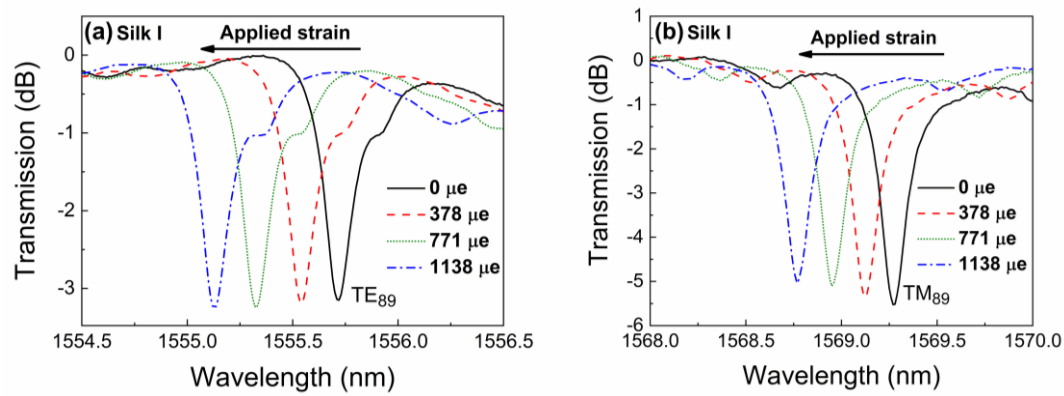


Figure 5.19 Transmission spectra of the TE and TM WGMs with modal order $m=89$, confined inside the silk fibroin cavity for Silk I state, under the applied strain along the longitudinal axis of the supporting optical fiber taper

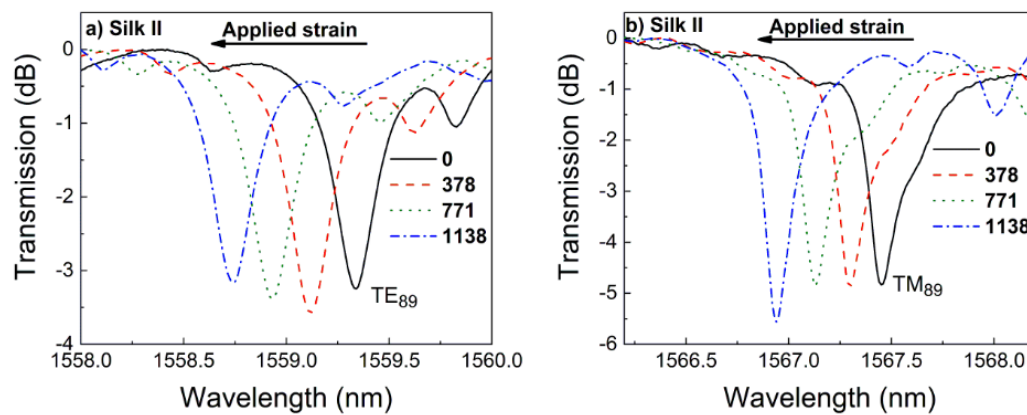


Figure 5.20 Transmission spectra of the TE and TM WGMs with modal order $m=89$, confined inside the silk fibroin cavity for Silk II state, under the applied strain along the longitudinal axis of the supporting optical fiber taper

As the amount of strain applied increases, the mode spectral positions for both polarizations undergo a frequency shift toward the blue end of the spectrum. This finding is in line with research that was done in the past on other cavity materials and geometries.

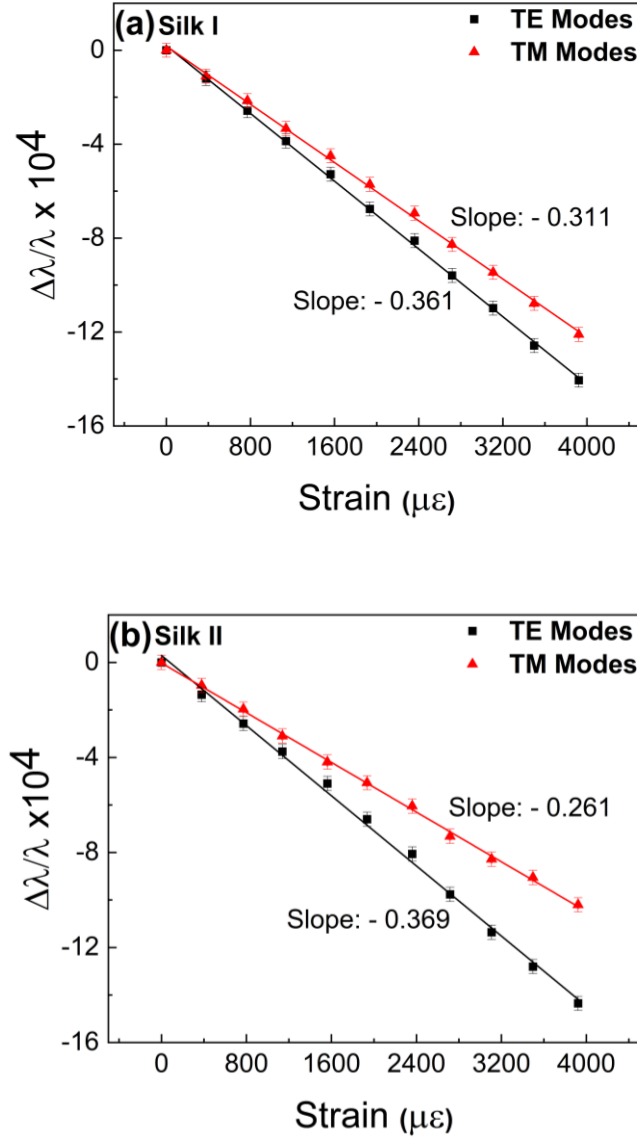


Figure 5.21 Wavelength normalized WGM spectral shift data versus strain for TE and TM polarizations for silk fibroin resonating cavities in Silk I (a) and Silk II (b) states.

Figure 5.21 illustrates the corresponding spectral shifts of the TE and TM WGMs of the silk fibroin cavity as a function of applied strain for both the as-cast (Silk I) state and the thermally treated (Silk II) state. The subsequent strain-induced optical birefringence emerging is presented in Figure 5.22.

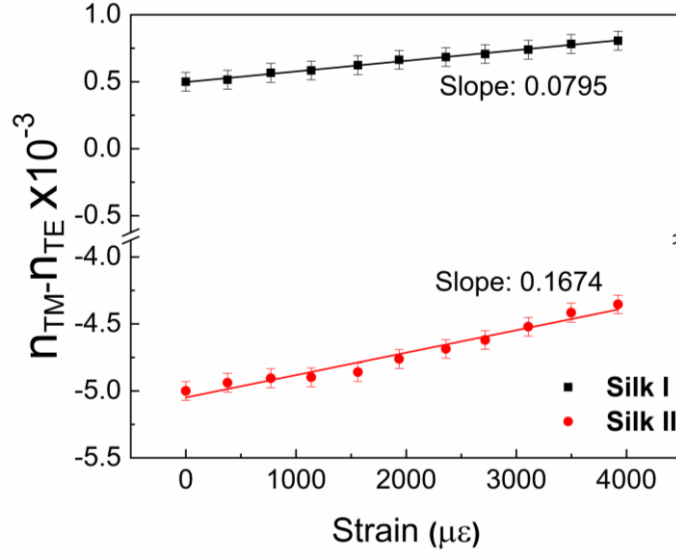


Figure 5.22 The strain-induced birefringence of Silk I and II state fibroin cavities was measured utilizing WGM resonance.

The dependence of the WGM spectral shifts versus elongation appeared linear and reversible; as a result, no material detachment occurred. These strain conditions were applied in the fibroin cavity for the Silk I and II structures. In addition to this, the slopes, $\frac{\Delta\lambda}{\lambda\epsilon}$ the TE and TM modes fall within the same order of magnitude as those obtained for other soft materials with a similar Young modulus. The data of $\Delta\lambda/\lambda$ versus strain ϵ of the fibroin cavity appended in Figure 5.22 reveal a quite interesting characteristic: the slopes $\frac{\Delta\lambda}{\lambda\epsilon}$ of the WGM for TE polarization are almost identical for Silk I and Silk II, while the slope of the TM polarization referring to Silk I is ~15% greater than that of Silk II. This was observed in all five silk fibroin cavities examined in Silk I and II, indicating that the strain-induced birefringence in the particular silk fibroin cavities is directional. Specifically, it mostly affects the TM polarization component parallel to the longitudinal axis of the supporting optical fiber taper.

Figure 5.22 demonstrates conclusively that the fibroin WGM cavity in the Silk II structure exhibits higher levels of both intrinsic and strain-induced birefringence than the Silk I structure. This purely optical behavior profoundly illustrates the fundamental protein rearrangements thermal annealing induces.

The birefringence data of Figure 5.21 are used for evaluating the photoelastic coefficients p_{11} and p_{12} and that of the strain-optical coefficient K' after estimating the strains exerted on the silk fibroin WGM cavity using a numerical 3D strain-stress analysis (Fig. 5.15 and Fig. 5.16) and the equation 3.32 & 3.36. Calculating the optical stress coefficient K involves utilizing data on Poisson's ratios and Young's moduli for two distinct silk fibroin states obtained through Brillouin Light Scattering (BLS) experiments. The optical, mechanical, and photo-elastic quantities of Silk I and Silk II fibroin films obtained from the WGM and BLS experiments are appended in Table 5.1.

Table 5.1. Experimentally obtained elasto-optic properties of Silk I and II WGM cavities.

	Initial Birefringence	Young modulus (GPa)	Photoelastic coefficients		Strain optical Coeff. K'	Stress-Optical Coeff. K (Br)
			p_{11}	p_{12}		
Silk I	$0.5 \times 10^{-3} \pm 7 \times 10^{-5}$	9.34 ± 0.0 5	$0.098 \pm 3 \times 10^{-3}$	$0.132 \pm 4 \times 10^{-3}$	$0.059 \pm 9 \times 10^{-3}$	8.1 ± 3.1
Silk II	$-5 \times 10^{-3} \pm 7 \times 10^{-5}$	9.69 ± 0.0 5	$0.048 \pm 3 \times 10^{-3}$	$0.120 \pm 4 \times 10^{-3}$	$0.129 \pm 9 \times 10^{-3}$	17.0 ± 0.7

To assess the dependability of our experimental setup, we computed the photoelastic coefficients p_{11} and p_{12} for an extensively studied material, namely silica glass. Consequently, we performed comparable experiments on a 30 μm diameter tapered optical fiber sample that lacked silk fibroin cavities atop it, employing the same strain levels as those in the experiments involving silk cavities. Figure 5.23 illustrates the spectral displacement of particular TE and TM mode resonances.

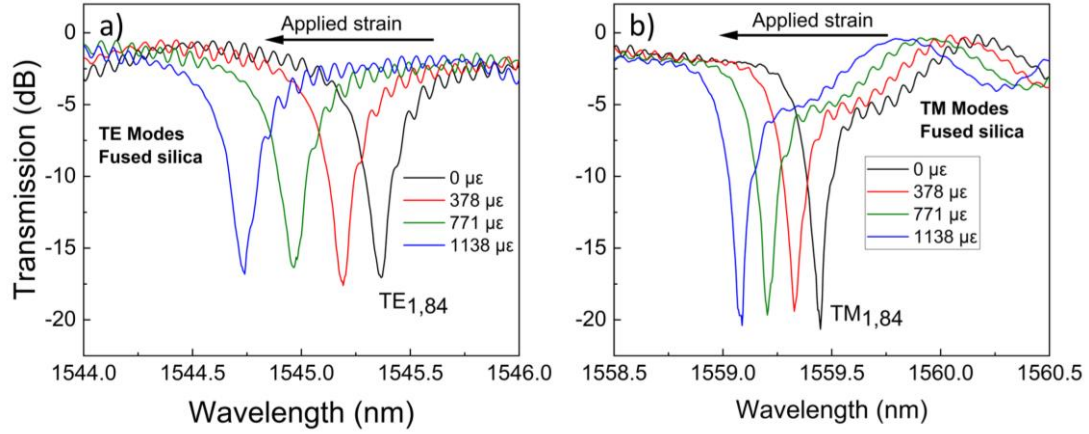


Figure 5.23 Transmission spectra of the TE and TM WGMs with modal order $m=84$, confined inside the fused silica cavity under the applied strain along the longitudinal axis of the optical fiber taper

Figure 5.24 presents a comparative analysis of the strain-induced shift measurements of WGM in cavities composed of all-silica and silk/silica glass composites.

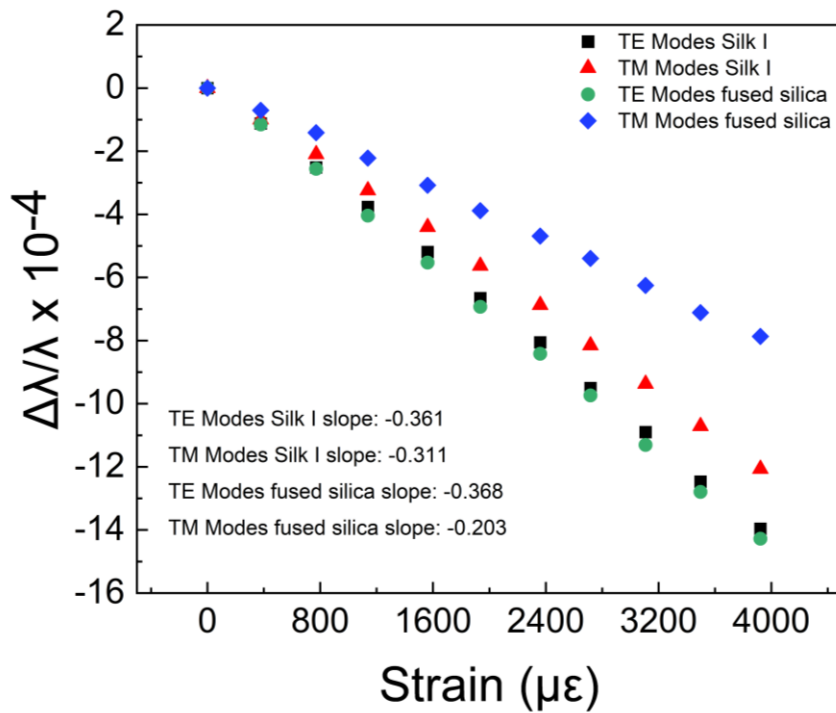


Figure 5.24 Normalised spectral shifts $\Delta\lambda/\lambda$ versus longitudinal strain applied, in an all-silica WGM cavity and a silk fibroin on-silica WGM cavity, resting in the same wavelength vicinity.

By employing the conventional mechanical properties of fused silica, namely a Poisson's ratio of 0.17 and Young's modulus of 72 GPa, it is possible to calculate the photoelastic coefficient of this material. Notably, prior studies have demonstrated that the photoelastic coefficients obtained through measurements of the WGMs of all-silica glass cavities ($p_{11}=0.117$ and $p_{12}=0.253$) are in excellent agreement with the values reported in the existing literature [66].

5.4 Details of simulations for mode allocation in silk fibroin cavities

The whispering gallery modes of the investigated system were computed using full-wave eigenvalue simulations [133] within COMSOL Multiphysics. The simulations considered the silk fibroin cavity cylindrical and treated as a two-dimensional resonant structure. This is justified by the geometry of the cavity, which changes slowly along with the z -axis, and the fact that modal excitations occur within the cavity's middle section, which is far from side-located turning points. Two indices, the azimuthal (m) and radial (l) orders, as well as the resonant modes' polarization (TE: $H=H_z$ and TM: $E=E_z$), are used to describe the modes' resonant frequencies.

Before employing the numerical simulations in the silk fibroin cavities that were the subject of the study, their accuracy was verified in an archetypical cylinder resonator geometry by comparing the results of the simulations against rigorous analytical solutions [134]. A homogeneous cylinder with $n_{\text{cyl}}=1.513$, $n_{\text{host}}=1$ and $r=15.8\ \mu\text{m}$ is considered. The calculated resonant wavelength between theory and simulation for an indicative TE ($m=89$) and TM ($m=89$) resonant mode is presented in Table S1. It is observed that there is an excellent agreement, with the fractional error in resonant frequency falling below 1%. The transcendental equations that are solved are [134] :

$$\frac{1}{u} \frac{J'_m(u)}{J_m(u)} - \frac{1}{v} \frac{H_m^{(1)'}(v)}{H_m^{(1)}(v)} = 0, \quad (5.5)$$

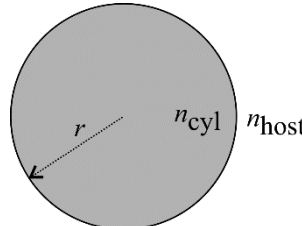
for the TE ($\mathbf{H}=H_z\mathbf{z}$) and

$$\frac{k_{\text{cyl}}^2}{u} \frac{J'_m(u)}{J_m(u)} - \frac{k_{\text{host}}^2}{v} \frac{H_m^{(1)'}(v)}{H_m^{(1)}(v)} = 0, \quad (5.6)$$

For the TM ($\mathbf{E}=E_z\mathbf{z}$) polarization, respectively, where $u = k_{\text{cyl}}r$ and $v = k_{\text{host}}r$, with $k_{\text{cyl}} = k_0 n_{\text{cyl}}$ and $k_{\text{host}} = k_0 n_{\text{host}}$. Each equation can have an uncountable infinite number of roots corresponding to different modes of radial order l . This is true for every azimuthal order m .

Table 5.2. Analytical and simulated results for the archetypical dielectric cylinder structure are compared and contrasted concerning their respective calculated resonant frequencies. This is demonstrated in the enclosing inset.

Mode	$\lambda_0 -$ theory (nm)	$\lambda_0 -$ simulation (nm)	Fractional error
TE, $m=89$	1562.8	1562.7	-0.6%
TM, $m=89$	1551.0	1550.9	-0.6%



The system under study is depicted in Figure 5.8(a). It is a two-dimensional equivalent of an actual structure. The parameters are $n_{\text{Silk I}} = 1.5215$, $n_{\text{SiO}_2} = 1.45$, $r_{\text{out}} = 15.78 \mu\text{m}$. Modes of different azimuthal and radial order can be supported

by the structure, identified by the azimuthal order (m) radial order (l). Indicative examples of first-radial order modes of the TE polarization are shown in Figure 5.25(c-d). The free spectral range is ~ 16 nm in close agreement with the measurement. We determine the mode allocation in experimental results based on the calculated resonant wavelengths. Examples of higher-radial-order resonances are depicted in Figure 5.25(e-f). The resonant wavelengths can be associated with secondary spectral features of the experimental transmission curve [135], as seen in Figure 5.25(b).

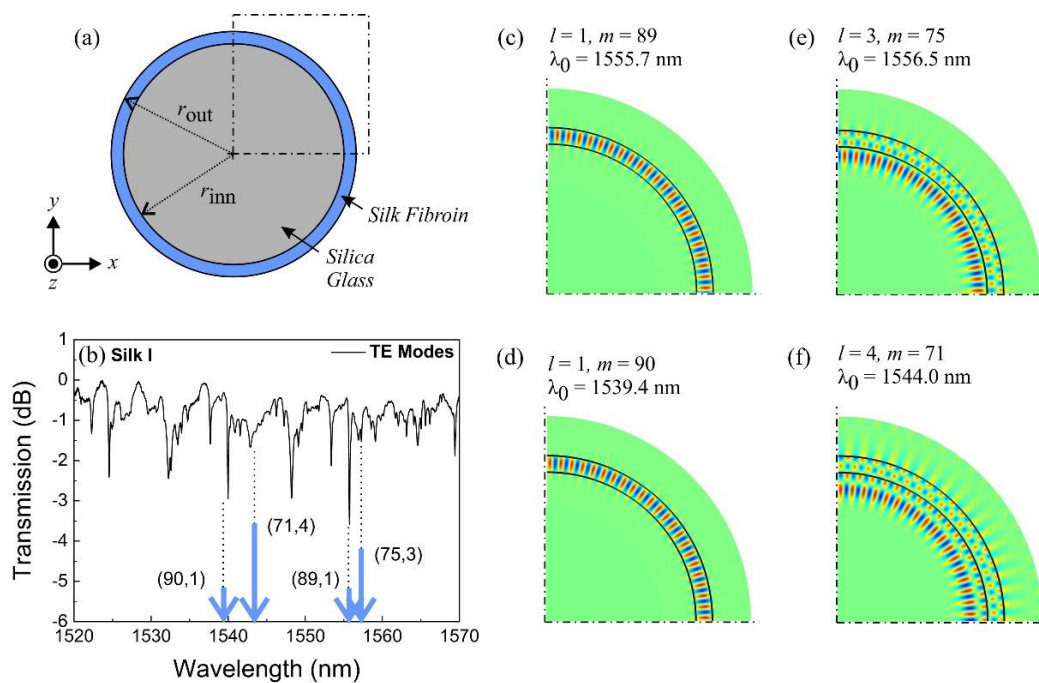


Figure 5.25 (a) Schematic of resonant silk fibroin cavity under study. A cylindrical structure is assumed, invariant along z , modeled as a 2D geometry. (b) Experimentally measured transmission spectra for TE polarization reproduced from Figure 2 in the manuscript. (c-f) Mode profiles for indicative resonances of first (c), second (d), third (e), and fourth (f) radial order (l). The simulated resonant wavelength is marked in panel (b) and is in very good agreement with the spectral locations of the experimental features.

As a post-processing step in the finite element method eigenvalue simulations, the stored energy density was integrated within the various material regions to determine how light is confined within the silk layer. This calculation is crucial for determining whether the elasto-optical parameters of the silica glass influence the experimental measurements. For the TE mode of Silk I with azimuthal order $m=89$, depicted in Figure 5.25(c), only 2.1% of the total stored energy resides in the silica glass, 97.1% in the silk layer, and the remaining 0.8% in the surrounding air. The corresponding percentage in silica for the first-radial order TM Modes is approximately 1.2%. Consequently, nearly all injected light intensity will be waveguided through the silk fibroin region for the exciting first-order radial modes in the structure. Therefore, the contribution of silica glass to the photoelastic behavior is negligible and can be disregarded. The modes become leakier for higher radial orders, and gradually, light further resides in the silica region [see Fig. 5.25(e-f)]. Specifically, for modes of radial order $l = [2,3,4]$ the stored energy in silica is in the order of (32%, 67%, 71%), respectively, and in air (1.8%, 2.5%, 6.1%).

5.5 Discussion

According to the results of the WGM performed on thin film cavities, the amorphous Silk I and the semi-crystalline Silk II have the same chemical stoichiometry but differ in their refractive and photoelastic properties. Silk II demonstrates a significant strain-induced optical birefringence, with the component with a higher refractive index being measured along the longitudinal axis of the WGM cavities. It is worth noting that Young's modulus of Silk II is only slightly higher than that of Silk I. As such, the transformation of Silk fibroin from an amorphous to a semi-crystalline structure affects the strain-induced optical birefringence, $\Delta n_{\text{TM-TE}}$, (by order of magnitude), and the optical stress coefficient (by more than 50%) to a greater extent than the elastic material

response, which is impacted only marginally (by 4%). These findings highlight the fundamental importance of segmental orientation in the context of photoelasticity. Silk I is comprised mainly of α -helix and random coil conformations and substantially less of β -sheet crystalline domains, also preserving a reasonable water content, which acts as a plasticizer [136]. Silk I's low initial (residual) birefringence (Table 5.1), a characteristic typically associated with atactic polymers, also confirms its amorphous structure [137], [138]. The photoelasticity figures for Silk I are similar to those holding for bulk polymers; for comparison, the strain and stress-optical coefficients of polystyrene are ~ 0.01 and $\sim 12\text{Br}$, respectively, while assuming $E=3.4\text{GPa}$, significantly lower than for the E value in Silk I, with similar Poisson's ratio. The high E values of Silk I and II imply dense local packing, as suggested by the relatively high density (1450 kg/m^3) [139].

The polarization splitting and birefringence data for the Silk II structure illustrate the structural transformation that occurs in the Silk II structure. The system receives energy from the annealing process in ambient air, which gradually dehydrates the Silk I material and promotes the formation of β -sheets for reaching the Silk II stage [140]. The carefully controlled rise in temperature that characterizes the annealing process during ambient air exposure is known to play a critical role in transforming Silk fibroin from its amorphous Silk I form to the more stable, semi-crystalline Silk II structure. This transformation is made possible by severing intramolecular hydrogen bonds within the Silk I structure, allowing the constituent molecules to reorganize themselves into more stable and highly ordered β -sheet conformations. Notably, this reorganization occurs without any danger of oxidation [141]. It is worth emphasizing that the structural crossover from Silk I to Silk II can indeed impact the material's segmental orientation. Nonetheless, our observations indicate that the effect on the elastic modulus is relatively subtle, suggesting that there may be a similar local packing arrangement for Silk I and Silk II. For a natural silk fiber system, specifically *Nephila pilipes* spider silk fiber [142], the elastic Young's modulus is strongly

anisotropic due to the chain stretching along the fiber axis. The experimental E for both Silk film samples is very close to the E value for the *Nephila pilipes* spider silk fiber normal to the fiber axis being about twice lower than along the fiber axis [142].

The different TM WGM polarization $\Delta\lambda/\lambda$ slopes of Figure 5.22 for Silk I and II denote that the strain-induced birefringence cannot be explained by the high stiffness of the β -sheets [143], considering that the two fibroin structures have very similar mechanical properties. Instead, the apparent disparity in the birefringence and stress optical coefficient is mainly due to p_{11} , which relates to the segmental optical anisotropy of the two Silk structures. Thus, the origin of large optical anisotropy in Silk II is attributed to the number and orientation of the β -sheets and the stretched chains linking these nanocrystals compared to Silk I. This feature is captured explicitly with the WGM resonator experiments and remains elusive in the elastic Young's modulus for the thicker film samples of the BLS experiment.

5.6 Chapter conclusions

This chapter delves into examining the photoelastic characteristics of two states of silk fibroin: the amorphous (Silk I) and the semi-crystalline (Silk II). Employing Brillouin Light Scattering (BLS) spectroscopy, we computed significant mechanical parameters, such as Poisson's ratio and Young's Modulus, for both states of Silk fibroin. Intriguingly, these mechanical properties exhibited no alteration as we transitioned from the Silk I to the Silk II state, a phenomenon attributed to the semi-crystalline nature of the Silk II state. However, an intriguing discovery was made regarding the strain-induced birefringence in Silk II. By applying the Whispering Gallery Mode (WGM) resonance technique, the calculated birefringence in Silk II was twice as high compared to Silk I. The outcome was in conjunction with the beta-sheets

alignment parallel to the strain-induced longitudinal strain axis. This causes the emergence of two distinctive axes for light propagation – a fast axis and a slow axis. This differentiation contributes to a significant enhancement of strain-induced birefringence in the Silk II state.

6 Thesis Conclusions and future plans

6.1 WGMs resonances in thermally poled glass optical cavities

This thesis used WGM resonance as a diagnostic approach in tracing transparent optical materials' optical and other physical properties in micrometric cavities. Our investigations, which used optical, spectral, and structural characterization techniques, revealed for the first time the effect of thermal poling on whispering gallery mode resonances localized inside glass hetero-fiber cavities. The WGM hetero-fiber cavity examined was fabricated from Duran® glass containing a silver wire in its center. Two different thermal poling configurations were used. The first one was equipped with a blocking anode, necessitating using nitrogen flow throughout the process. A non-blocking anode was chosen in the second setup, which means the thermal poling was conducted under atmospheric air conditions.

Regarding the blocking anode, our investigations revealed that the ion depletion and ion accumulation zones impact the resonance properties of radially poled glass cylindrical cavities through the selective suppression or even destruction of higher-order radial WGMs, the effective “spectral cleaning” of these cavities. Thermal poling significantly alters the radial distribution of the refractive index and, consequently, the excitation properties of higher-order radial WGMs (particularly for TE/TM_(2, m) WGMs), preferentially shifting their power distribution closer to the hetero-fiber cavity center. Using FEM simulations, we have confirmed the impact of the low refractive index ion depletion zone and the high refractive index ion-accumulation zone on dampening the higher radial order WGM resonances, consistent with the spectral findings. Additionally, we should point out that the current “spectral cleaning” is caused by poling-induced preferential WGM power redistribution and

evanescent mode coupling reduction, which distinguishes it from previous “spectral cleaning techniques” [131], [144], [145]. Our research suggests that the elaboration of thermal poling of circular symmetry glass cavities can serve as a precise refractive index and polarization engineering tool for modal selection, with potential applications including modal suppression in lasing cavities and spectral cleaning of sensing devices that use WGM resonances, particularly when combined with new types of active glasses [146]. Aside from that, the wavelength shifts and variations in excitation efficiency of the various WGM resonances can be used to better understand and monitor the dynamics of ion migration during glass poling.

The concept of thermal poling of ion-rich glasses can be strategically applied to creating sensors capable of measuring high-intensity electric fields. An external electric field, acting through the electro-optic effect, can alter the refractive index in the region proximate to the fiber circumference where the glass possesses a non-zero second-order susceptibility $\chi^{(2)}$. Consequently, shifts in the Whispering Gallery Modes (WGMs) resonances can be transduced by the externally applied electric field and act as a practical sensor. Operational environments characterized by high electric fields, such as those in power lines, can disrupt conventional electronic sensors' electronic components. Therefore, developing an all-optical sensor, undeterred by such electric fields, could solve this issue effectively.

Initial groundwork for constructing this type of sensor was undertaken during my doctoral research. A diagrammatic portrayal of this can be found in Figure 6.1.

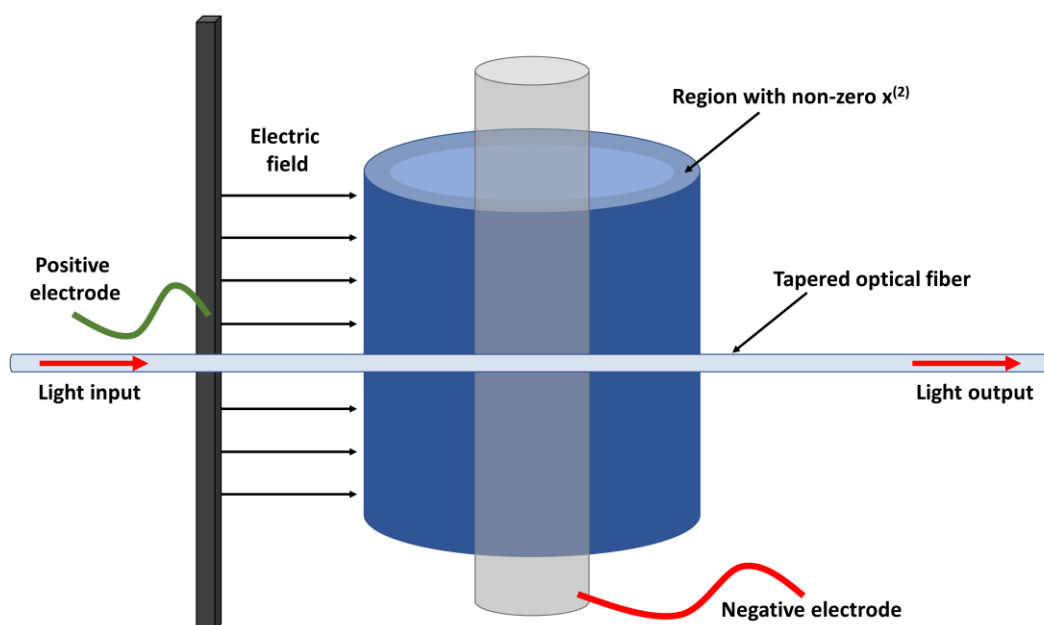


Figure 6.1 A diagrammatic depiction of the setup subjected to tests as an electric field sensor

Nonetheless, the setup depicted above possesses a fundamental flaw in its ability to sense electric fields. The problem arises from the existence of silver cable within the core of the hetero-fiber. Upon the application of an electric field between the positive and negative electrodes, a Lorentz force comes into effect between these electrodes. This causes the hetero-fiber to move, which, in turn, results in a shift in the position of the tapered fiber. The spectral shifts caused by the arbitrary movement of the tapered fiber are substantially more pronounced than those resulting from the electro-optic effect. Thus, the future objective is to implement a method to remove the metallic wire from the core of the hetero-fiber or to thermally pole ion-rich glass cylindrical capillaries that can readily accommodate the insertion and removal of such metal cables within them.

6.2 WGMs resonances in silk fibroin optical cavities

The whispering gallery mode resonance, which offers high accuracy and significant insight capabilities in the study of soft materials, was utilized by us to look into the photoelastic properties of silk fibroin. We propose that the photoelasticity of Silk II is primarily attributable to the high optical polarizability properties of the β -sheets and their strain-induced alignment, as opposed to the mechanical properties of the annealed fibroin. Brillouin light spectroscopy uncovered an unexpected similarity between the elastic Young's moduli of Silk I and Silk II. By illuminating the significance of β -sheets and their influence on the optical properties of Silk II, our study has paved the way for further research into the topic. Applying external stimulations (i.e., high voltage poling) for tuning the formation and orientation of β -sheets emerges as a promising approach for developing optical biomaterials with high polarizability properties for linear or non-linear [147] optical operations. Silk II's β -sheet-dominated refractivity and photoelasticity can be exploited further in developing planar or fiber-guided wave structures with exotically high birefringence [137] for polarization-selective passive and active photonic devices. In addition, the light scattering properties of Silk II, both elastic and inelastic, merit investigation. The investigation of fundamental materials' properties using WGMs was greatly aided by the small mode volume of these resonances. This strong interaction enables us to probe these materials' optical and other physical properties with exceptional sensitivity and precision, providing insights into their behavior and properties at the microscale level.

The potential for future research lies in combining the two works presented in this thesis, specifically in silk fibroin WGM cavities. A schematic representation of this concept is illustrated in Figure 6.2. Specifically, the creation of WGM cavities on hetero-fibers could be integrated with a modified thermal poling

procedure, inducing Silk II crystallinity at an elevated state whereby the electric field orientation would dictate the direction of the b-sheets. As a result, WGM cavities could be created with a specific and controllable orientation of the silk fibroin b-sheets, developing novel optical and mechanical properties. The thermal poling setup outlined in this thesis will be employed, with a notable modification in the poling conditions: a temperature of 180 °C will be maintained for 15 minutes. Various voltage values will be tested as part of this innovative investigation.

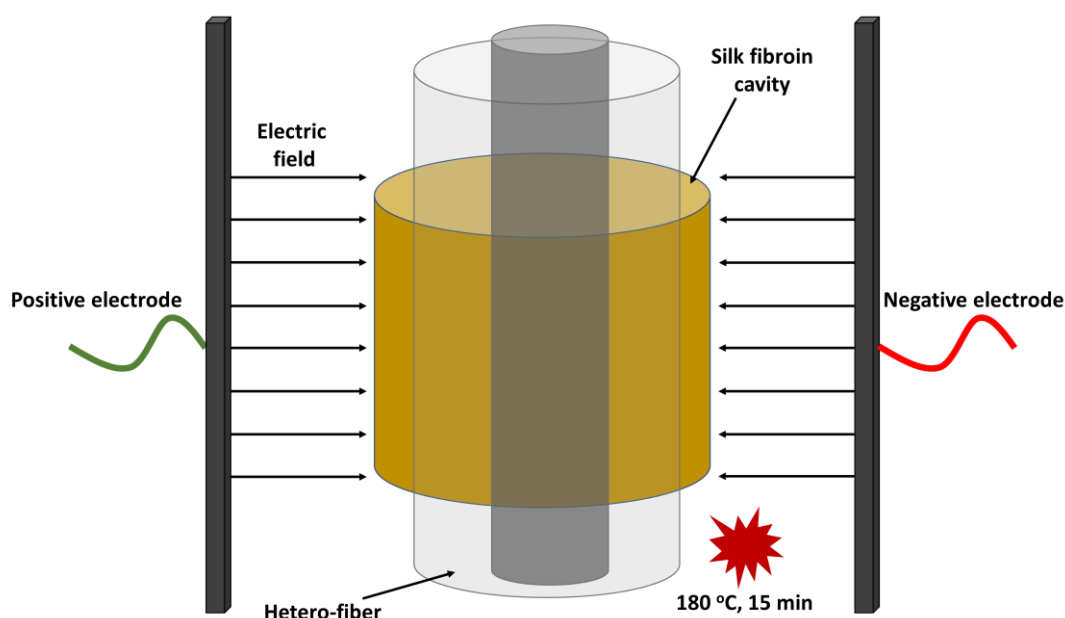


Figure 6.2 A schematic representation of the proposed setup for the thermal poling of silk fibroin cavities

The proposed concept is expected to result in creating a material endowed with distinct mechanical and photoelastic properties, thus expanding the potential applications in the field of material science.

References

- [1] M. R. Foreman, J. D. Swaim, and F. Vollmer, “Whispering gallery mode sensors,” *Adv. Opt. Photon.*, vol. 7, no. 2, pp. 168–240, 2015.
- [2] L. R. O. M. F.R.S., “CXII. The problem of the whispering gallery,” *London, Edinburgh, Dublin Philos. Mag. J. Sci.*, vol. 20, no. 120, pp. 1001–1004, 1910.
- [3] K. J. Vahala, “Optical microcavities,” *Nature*, vol. 424, no. 6950, pp. 839–846, 2003.
- [4] M. L. Gorodetsky, A. A. Savchenkov, and V. S. Ilchenko, “Ultimate Q of optical microsphere resonators,” *Opt. Lett.*, vol. 21, no. 7, pp. 453–455, 1996.
- [5] X. Jiang, A. J. Qavi, S. H. Huang, and L. Yang, “Whispering-Gallery Sensors,” *Matter*, vol. 3, no. 2, pp. 371–392, Aug. 2020.
- [6] C.-H. Dong *et al.*, “Fabrication of high-Q polydimethylsiloxane optical microspheres for thermal sensing,” *Appl. Phys. Lett.*, vol. 94, no. 23, p. 231119, 2009.
- [7] T. Ioppolo, M. Kozhevnikov, V. Stepaniuk, M. V. Ötügen, and V. Sheverev, “Micro-optical force sensor concept based on whispering gallery mode resonators,” *Appl. Opt.*, vol. 47, no. 16, pp. 3009–3014, Jun. 2008.
- [8] T. Ioppolo, J. Stubblefield, and M. V. Ötügen, “Electric field-induced deformation of polydimethylsiloxane polymers,” *J. Appl. Phys.*, vol. 112, no. 4, p. 44906, 2012.
- [9] F. Vollmer and L. Yang, “Review Label-free detection with high-Q microcavities: a review of biosensing mechanisms for integrated devices,” vol. 1, no. 3–4, pp. 267–291, 2012.

- [10] Q. Ma, L. Huang, Z. Guo, and T. Rossmann, "Spectral shift response of optical whispering-gallery modes due to water vapor adsorption and desorption," *Meas. Sci. Technol.*, vol. 21, no. 11, p. 115206, Oct. 2010.
- [11] Y. Zhi, X.-C. Yu, Q. Gong, L. Yang, and Y.-F. Xiao, "Single Nanoparticle Detection Using Optical Microcavities," *Adv. Mater.*, vol. 29, no. 12, p. 1604920, 2017.
- [12] F. Vollmer, S. Arnold, and D. Keng, "Single virus detection from the reactive shift of a whispering-gallery mode," *Proc. Natl. Acad. Sci.*, vol. 105, no. 52, pp. 20701–20704, 2008.
- [13] L. He, S. K. Ozdemir, J. Zhu, W. Kim, and L. Yang, "Detecting single viruses and nanoparticles using whispering gallery microlasers.," *Nat. Nanotechnol.*, vol. 6, no. 7, pp. 428–432, Jun. 2011.
- [14] L. Shao *et al.*, "Detection of Single Nanoparticles and Lentiviruses Using Microcavity Resonance Broadening," *Adv. Mater.*, vol. 25, no. 39, pp. 5616–5620, 2013.
- [15] F. Vollmer, D. Braun, A. Libchaber, M. Khoshshima, I. Teraoka, and S. Arnold, "Protein detection by optical shift of a resonant microcavity," *Appl. Phys. Lett.*, vol. 80, no. 21, pp. 4057–4059, 2002.
- [16] M. K. Park *et al.*, "Label-free aptamer sensor based on silicon microring resonators," *Sensors Actuators B Chem.*, vol. 176, pp. 552–559, 2013.
- [17] S. Berneschi *et al.*, "Optical whispering gallery mode resonators for label-free detection of water contaminants," *TrAC Trends Anal. Chem.*, vol. 126, p. 115856, 2020.
- [18] J. Álvarez Freile, G. Choukrani, K. Zimmermann, E. Bremer, and L. Dähne, "Whispering Gallery Modes-based biosensors for real-time monitoring and binding characterization of antibody-based cancer immunotherapeutics," *Sensors Actuators B Chem.*, vol. 346, p. 130512, 2021.

- [19] Y. Sun, S. I. Shopova, G. Frye-Mason, and X. Fan, “Rapid chemical-vapor sensing using optofluidic ring resonators,” *Opt. Lett.*, vol. 33, no. 8, pp. 788–790, Apr. 2008.
- [20] V. M. N. Passaro, F. Dell’Olio, and F. De Leonardis, “Ammonia Optical Sensing by Microring Resonators,” *Sensors*, vol. 7, no. 11, pp. 2741–2749, 2007.
- [21] V. Melissinaki, O. Tsilipakos, M. Kafesaki, M. Farsari, and S. Pissadakis, “Micro-Ring Resonator Devices Prototyped on Optical Fiber Tapers by Multi-Photon Lithography,” *IEEE J. Sel. Top. Quantum Electron.*, vol. 27, no. 6, pp. 1–7, 2021.
- [22] T. Ioppolo and M. V. Ötügen, “Magnetorheological polydimethylsiloxane micro-optical resonator,” *Opt. Lett.*, vol. 35, no. 12, pp. 2037–2039, Jun. 2010.
- [23] T. Ioppolo, U. Ayaz, and M. V. Ötügen, “Tuning of whispering gallery modes of spherical resonators using an external electric field,” *Opt. Express*, vol. 17, no. 19, pp. 16465–16479, Sep. 2009.
- [24] A. R. Ali, T. Ioppolo, V. Ötügen, M. Christensen, and D. MacFarlane, “Photonic electric field sensor based on polymeric microspheres,” *J. Polym. Sci. Part B Polym. Phys.*, vol. 52, no. 3, pp. 276–279, 2014.
- [25] R. Madugani, Y. Yang, V. H. Le, J. M. Ward, and S. Nic Chormaic, “Linear Laser Tuning Using a Pressure-Sensitive Microbubble Resonator,” *IEEE Photonics Technol. Lett.*, vol. 28, no. 10, pp. 1134–1137, 2016.
- [26] M. Manzo, T. Ioppolo, U. K. Ayaz, V. LaPenna, and M. V. Ötügen, “A photonic wall pressure sensor for fluid mechanics applications,” *Rev. Sci. Instrum.*, vol. 83, no. 10, p. 105003, 2012.
- [27] M. Konstantaki *et al.*, “Silk Fibroin Enabled Optical Fiber Methanol Vapor Sensor,” *IEEE Photonics Technol. Lett.*, vol. 32, no. 9, pp. 514–

- 517, 2020.
- [28] R. A. Myers, N. Mukherjee, and S. R. J. Brueck, “Large second-order nonlinearity in poled fused silica,” *Opt. Lett.*, vol. 16, no. 22, pp. 1732–1734, 1991.
 - [29] P. G. Kazansky, L. Dong, P. Hua, and P. S. J. Russell, “High second-order nonlinearities in poled silica fibers,” in *Conference on Lasers and Electro-Optics*, 1994, p. CFC3.
 - [30] T. Fujiwara, D. Wong, and S. Fleming, “Large Electrooptic Modulation in a Thermally-Poled Germanosilicate Fiber,” *IEEE Photonics Technol. Lett.*, vol. 7, no. 10, pp. 1177–1179, 1995.
 - [31] N. Myrén *et al.*, “Wide wedge-shaped depletion region in thermally poled fiber with alloy electrodes,” *Opt. Express*, vol. 12, no. 25, pp. 6093–6099, 2004.
 - [32] D. Wong, W. Xu, S. Fleming, M. Janos, and K.-M. Lo, “Frozen-in Electrical Field in Thermally Poled Fibers,” *Opt. Fiber Technol.*, vol. 5, no. 2, pp. 235–241, 1999.
 - [33] W. Margulis, O. Tarasenko, and N. Myrén, “Who needs a cathode? Creating a second-order nonlinearity by charging glass fiber with two anodes,” *Opt. Express*, vol. 17, no. 18, p. 15534, 2009.
 - [34] H. An and S. Fleming, “Investigating the effectiveness of thermally poling optical fibers with various internal electrode configurations,” *Opt. Express*, vol. 20, no. 7, pp. 7436–7444, Mar. 2012.
 - [35] F. De Lucia and P. J. A. Sazio, “Thermal Poling of Optical Fibers: A Numerical History,” *Micromachines*, vol. 11, no. 2, 2020.
 - [36] F. Lind, D. Palles, D. Möncke, E. I. Kamitsos, and L. Wondraczek, “Modifying the surface wetting behavior of soda-lime silicate glass substrates through thermal poling,” *J. Non. Cryst. Solids*, vol. 462, pp. 47–

50, 2017.

- [37] A. Lepicard *et al.*, “Surface Reactivity Control of a Borosilicate Glass Using Thermal Poling,” *J. Phys. Chem. C*, vol. 119, no. 40, pp. 22999–23007, Oct. 2015.
- [38] M. Dussauze, E. I. Kamitsos, E. Fargin, and V. Rodriguez, “Refractive index distribution in the non-linear optical layer of thermally poled oxide glasses,” *Chem. Phys. Lett.*, vol. 470, no. 1, pp. 63–66, 2009.
- [39] P. Maxime, D. Marc, F. Evelyne, P.-Q. Angeline, and C. Thierry, “Hardness reinforcement by surface engineering of soda lime silicate glass under thermal poling,” in *Photonics and Fiber Technology 2016 (ACOFT, BGPP, NP)*, 2016, p. BT5B.1.
- [40] A. Dergachev *et al.*, “Control of soda-lime glass surface crystallization with thermal poling,” *J. Non. Cryst. Solids*, vol. 533, p. 119899, 2020.
- [41] S.-T. Han *et al.*, “An Overview of the Development of Flexible Sensors,” *Adv. Mater.*, vol. 29, no. 33, p. 1700375, 2017.
- [42] L. Li, Z. Wu, S. Yuan, and X.-B. Zhang, “Advances and challenges for flexible energy storage and conversion devices and systems,” *Energy Environ. Sci.*, vol. 7, no. 7, pp. 2101–2122, 2014.
- [43] S. Ummartyotin, J. Juntaro, M. Sain, and H. Manuspiya, “Development of transparent bacterial cellulose nanocomposite film as substrate for flexible organic light emitting diode (OLED) display,” *Ind. Crops Prod.*, vol. 35, no. 1, pp. 92–97, 2012.
- [44] Q. Hua *et al.*, “Skin-inspired highly stretchable and conformable matrix networks for multifunctional sensing,” *Nat. Commun.*, vol. 9, no. 1, p. 244, 2018.
- [45] X.-S. Zhang, M. Han, B. Kim, J.-F. Bao, J. Brugger, and H. Zhang, “All-in-one self-powered flexible microsystems based on triboelectric

- nanogenerators,” *Nano Energy*, vol. 47, pp. 410–426, 2018.
- [46] X. & G. K. Das, R., He, “Flexible, printed and organic electronics 2019-2029: forecasts, players & opportunities.,” *IDTechEx.com*, 2018. .
- [47] H. Park *et al.*, “Enhanced Moisture-Reactive Hydrophilic-PTFE-Based Flexible Humidity Sensor for Real-Time Monitoring,” *Sensors*, vol. 18, no. 3, 2018.
- [48] J. Chen *et al.*, “Polydimethylsiloxane (PDMS)-Based Flexible Resistive Strain Sensors for Wearable Applications,” *Appl. Sci.*, vol. 8, no. 3, 2018.
- [49] D. Ji, T. Li, W. Hu, and H. Fuchs, “Recent Progress in Aromatic Polyimide Dielectrics for Organic Electronic Devices and Circuits,” *Adv. Mater.*, vol. 31, no. 15, p. 1806070, 2019.
- [50] K. P. Sibin *et al.*, “Highly transparent and conducting ITO/Ag/ITO multilayer thin films on FEP substrates for flexible electronics applications,” *Sol. Energy Mater. Sol. Cells*, vol. 172, pp. 277–284, 2017.
- [51] Y. Jiang *et al.*, “Laser-Etched Stretchable Graphene–Polymer Composite Array for Sensitive Strain and Viscosity Sensors,” *Nano-Micro Lett.*, vol. 11, no. 1, p. 99, 2019.
- [52] M. Jian, Y. Zhang, and Z. Liu, “Natural Biopolymers for Flexible Sensing and Energy Devices,” *Chinese J. Polym. Sci.*, vol. 38, no. 5, pp. 459–490, 2020.
- [53] O. Hakimi, D. P. Knight, F. Vollrath, and P. Vadgama, “Spider and mulberry silkworm silks as compatible biomaterials,” *Compos. Part B Eng.*, vol. 38, no. 3, pp. 324–337, 2007.
- [54] B. Zhu *et al.*, “Silk Fibroin for Flexible Electronic Devices,” *Adv. Mater.*, vol. 28, no. 22, pp. 4250–4265, 2016.
- [55] S. Fan *et al.*, “Silk materials for medical, electronic and optical applications,” *Sci. China Technol. Sci.*, vol. 62, no. 6, pp. 903–918, 2019.

- [56] J. Huang *et al.*, “Stretchable and Heat-Resistant Protein-Based Electronic Skin for Human Thermoregulation,” *Adv. Funct. Mater.*, vol. 30, no. 13, p. 1910547, 2020.
- [57] M. Lee, H. Jeon, and S. Kim, “A Highly Tunable and Fully Biocompatible Silk Nanoplasmonic Optical Sensor,” *Nano Lett.*, vol. 15, no. 5, pp. 3358–3363, May 2015.
- [58] L. Xu *et al.*, “High-Q silk fibroin whispering gallery microresonator,” *Opt. Express*, vol. 24, no. 18, pp. 20825–20830, Sep. 2016.
- [59] G. C. Righini *et al.*, “Whispering gallery mode microresonators: Fundamentals and applications,” *La Riv. del Nuovo Cim.*, vol. 34, no. 7, pp. 435–488, 2011.
- [60] M. N. Zervas, M. N. M. Nasir, M. Ding, and G. S. Murugan, “Hybrid plasmonic bottle microresonators,” *Int. Conf. Transparent Opt. Networks*, pp. 2–6, 2014.
- [61] G. Senthil Murugan, J. Wilkinson, and M. Zervas, “Selective excitation of whispering gallery modes in a novel bottle microresonator,” *Opt. Express*, vol. 17, Aug. 2009.
- [62] H. Hossein, M. Mohammad-Ali, H. Matthias, C. D. N., and K. Mercedeh, “Parity-time-symmetric microring lasers,” *Science (80-.)*, vol. 346, no. 6212, pp. 975–978, Nov. 2014.
- [63] K. Hey Tow, D. M. Chow, F. Vollrath, I. Dicaire, T. Gheysens, and L. Thévenaz, “Exploring the Use of Native Spider Silk as an Optical Fiber for Chemical Sensing,” *J. Light. Technol.*, vol. 36, no. 4, pp. 1138–1144, 2018.
- [64] W. Huang, S. Ling, C. Li, F. G. Omenetto, and D. L. Kaplan, “Silkworm silk-based materials and devices generated using bio-nanotechnology,” *Chem. Soc. Rev.*, vol. 47, no. 17, pp. 6486–6504, Aug. 2018.

- [65] D. W. Kim *et al.*, “Novel fabrication of fluorescent silk utilized in biotechnological and medical applications.,” *Biomaterials*, vol. 70, pp. 48–56, Nov. 2015.
- [66] X. Roselló-Mechó, M. Delgado-Pinar, A. Díez, and M. V. Andrés, “Measurement of Pockels’ coefficients and demonstration of the anisotropy of the elasto-optic effect in optical fibers under axial strain,” *Opt. Lett.*, vol. 41, no. 13, pp. 2934–2937, Jul. 2016.
- [67] K. Milenko, S. Pissadakis, G. Gkantzounis, A. Aluculesei, and G. Fytas, “Probing Stress-Induced Optical Birefringence of Glassy Polymers by Whispering Gallery Modes Light Localization,” *ACS Omega*, vol. 2, no. 12, pp. 9127–9135, 2017.
- [68] K. Okamoto, “Chapter 1 - Wave theory of optical waveguides,” in *Fundamentals of Optical Waveguides (Second Edition)*, Second Edi., K. Okamoto, Ed. Burlington: Academic Press, 2006, pp. 1–12.
- [69] K. Okamoto, “Chapter 3 - Optical fibers,” in *Fundamentals of Optical Waveguides (Second Edition)*, Second Edi., K. Okamoto, Ed. Burlington: Academic Press, 2006, pp. 57–158.
- [70] International Telecommunications Union, “Optical Fibres, Cables and Systems,” pp. 144–147, 2009.
- [71] E. Hecht, *Optics*. Pearson, 2012.
- [72] Yariv, “Yariv A., Yeh P.-Photonics_ Optical Electronics in Modern Communications (2007).” .
- [73] D. Marcuse, “Theory of dielectric optical waveguides,” 1974.
- [74] “Light Rays,” in *Optics, Light and Lasers*, John Wiley & Sons, Ltd, 2006, pp. 1–32.
- [75] R. Black and L. Gagnon, *Optical Waveguide Modes: Polarization, Coupling and Symmetry*. 2010.

- [76] S. W. Harun, K. S. Lim, C. K. Tio, K. Dimyati, and H. Ahmad, "Theoretical analysis and fabrication of tapered fiber," *Optik (Stuttg.)*, vol. 124, no. 6, pp. 538–543, 2013.
- [77] F. Gonthier, "Tapered single-mode fibres and devices. Part 1: Adiabaticity criteria," *IEE Proc. J*, vol. 138, no. 5, pp. 343-354(11), 1991.
- [78] S. Ravets, J. E. Hoffman, P. R. Kordell, J. D. Wong-Campos, S. L. Rolston, and L. A. Orozco, "Intermodal energy transfer in a tapered optical fiber: optimizing transmission," *J. Opt. Soc. Am. A*, vol. 30, no. 11, pp. 2361–2371, 2013.
- [79] B. R. Johnson, "Theory of morphology-dependent resonances: shape resonances and width formulas," *J. Opt. Soc. Am. A*, vol. 10, no. 2, pp. 343–352, 1993.
- [80] J. D. Love, "Evanescent wave coupling of whispering gallery modes of a dielectric cylinder," *IEE Proc. J*, vol. 140, no. 3, pp. 177-188(11), 1993.
- [81] J. C. Knight, G. Cheung, F. Jacques, and T. A. Birks, "Phase-matched excitation of whispering-gallery-mode resonances by a fiber taper," *Opt. Lett.*, vol. 22, no. 15, pp. 1129–1131, 1997.
- [82] V. B. Braginsky, M. L. Gorodetsky, and V. S. Ilchenko, "Quality-factor and nonlinear properties of optical whispering-gallery modes," *Phys. Lett. A*, vol. 137, no. 7, pp. 393–397, 1989.
- [83] M. L. Gorodetsky, A. D. Pryamikov, and V. S. Ilchenko, "Rayleigh scattering in high-Q microspheres," *J. Opt. Soc. Am. B*, vol. 17, no. 6, pp. 1051–1057, 2000.
- [84] M. Delgado-Pinar, X. Roselló-Mechó, E. Rivera-Pérez, A. Díez, J. L. Cruz, and M. V. Andrés, "Whispering Gallery Modes for Accurate Characterization of Optical Fibers' Parameters," in *Applications of Optical Fibers for Sensing*, C. Cuadrado-Laborde, Ed. Rijeka: IntechOpen, 2018.

- [85] T. A. Birks, J. C. Knight, and T. E. Dimmick, "High-resolution measurement of the fiber diameter variations using whispering gallery modes and no optical alignment," *IEEE Photonics Technol. Lett.*, vol. 12, no. 2, pp. 182–183, 2000.
- [86] J. R. Wait, "Electromagnetic Whispering Gallery Modes in a Dielectric Rod," *Radio Sci.*, vol. 2, no. 9, pp. 1005–1017, 1967.
- [87] C.-L. Zou *et al.*, "Taper-microsphere coupling with numerical calculation of coupled-mode theory," *J. Opt. Soc. Am. B*, vol. 25, no. 11, pp. 1895–1898, Nov. 2008.
- [88] M. L. Gorodetsky and V. S. Ilchenko, "Optical microsphere resonators: optimal coupling to high-Q whispering-gallery modes," *J. Opt. Soc. Am. B*, vol. 16, no. 1, pp. 147–154, Jan. 1999.
- [89] N. Mukherjee, R. A. Myers, and S. R. J. Brueck, "Dynamics of second-harmonic generation in fused silica," *J. Opt. Soc. Am. B*, vol. 11, no. 4, pp. 665–669, 1994.
- [90] T. G. Alley, S. R. J. Brueck, and R. A. Myers, "Space charge dynamics in thermally poled fused silica," *J. Non. Cryst. Solids*, vol. 242, no. 2, pp. 165–176, 1998.
- [91] U. K. Krieger and W. A. Lanford, "Field assisted transport of Na⁺ ions, Ca²⁺ ions and electrons in commercial soda-lime glass I: Experimental," *J. Non. Cryst. Solids*, vol. 102, pp. 50–61, 1988.
- [92] P. G. Kazansky, A. R. Smith, P. S. J. Russell, G. M. Yang, and G. M. Sessler, "Thermally poled silica glass: Laser induced pressure pulse probe of charge distribution," *Appl. Phys. Lett.*, vol. 68, no. 2, pp. 269–271, 1996.
- [93] D. Pureur, A. C. Liu, M. J. F. Digonnet, and G. S. Kino, "Absolute measurement of the second-order nonlinearity profile in poled silica," *Opt. Lett.*, vol. 23, no. 8, pp. 588–590, 1998.

- [94] A. Kudlinski, Y. Quiquempois, and G. Martinelli, “Modeling of the $\chi^{(2)}$ susceptibility time-evolution in thermally poled fused silica,” *Opt. Express*, vol. 13, no. 20, pp. 8015–8024, 2005.
- [95] D. Faccio, V. Pruneri, and P. G. Kazansky, “Dynamics of the second-order nonlinearity in thermally poled silica glass,” *Appl. Phys. Lett.*, vol. 79, no. 17, pp. 2687–2689, 2001.
- [96] M. H. Sadd, Ed., “Appendix D - Review of Mechanics of Materials,” in *Elasticity (Second Edition)*, Second Edi., Boston: Academic Press, 2009, pp. 518–531.
- [97] Š. Višňovský, *Optics in Magnetic Multilayers and Nanostructures*. 2006.
- [98] “<https://www.cmscientific.eu/>.” .
- [99] A. Petropoulou *et al.*, “All-Fiber Plasmonic Platform Based on Hybrid Composite Metal/Glass Microwires,” *J. Phys. Chem. C*, vol. 122, no. 45, pp. 26169–26176, Nov. 2018.
- [100] J. W. Gooch, “Sellmeier Equation,” in *Encyclopedic Dictionary of Polymers*, J. W. Gooch, Ed. New York, NY: Springer New York, 2011, pp. 653–654.
- [101] ABRISA Technologies, “Specialty Glass Materials Products & Specifications,” no. 877, pp. 1–35, 2014.
- [102] P. G. Kazansky and P. S. J. Russel, “Thermally poled glass: frozen-in electric field or oriented dipoles?,” *Opt. Commun.*, vol. 110, no. 5–6, pp. 611–614, 1994.
- [103] F. C. Garcia, I. C. S. Carvalho, E. Hering, W. Margulis, and B. Lesche, “Inducing a large second-order optical nonlinearity in soft glasses by poling,” *Appl. Phys. Lett.*, vol. 72, no. 25, pp. 3252–3254, 1998.
- [104] G. Violakis, V. Tsafas, G. Filippidis, and S. Pissadakis, “Electrically Poled, MNA-Microstructured Optical Fibers for Second Harmonic

- Generation,” *IEEE J. Sel. Top. Quantum Electron.*, vol. 26, no. 4, p. 1, 2020.
- [105] L.-E. Tympa, K. Katsara, P. N. Moschou, G. Kenanakis, and V. M. Papadakis, “Do Microplastics Enter Our Food Chain Via Root Vegetables? A Raman Based Spectroscopic Study on *Raphanus sativus*,” *Materials (Basel)*., vol. 14, no. 9, 2021.
- [106] M. Fabbri and J. R. S. Senna, “Numerical Simulation of Ion Transport During Anodic Bonding,” *Proc. XXV Iber. Lat. Am. Congr. Comput. Methods*, no. November 2004, p. 10, 2004.
- [107] C. M. Lepienski, J. A. Giacometti, G. F. Leal Ferreira, F. L. Freire, and C. A. Achete, “Electric field distribution and near-surface modifications in soda-lime glass submitted to a dc potential,” *J. Non. Cryst. Solids*, vol. 159, no. 3, pp. 204–212, 1993.
- [108] O. Deparis, P. G. Kazansky, A. Podlipensky, A. Abdolvand, G. Seifert, and H. Graener, “Evolution of poling-assisted bleaching of metal-doped nanocomposite glass with poling conditions,” *Appl. Phys. Lett.*, vol. 86, no. 26, p. 261109, 2005.
- [109] M. Dussauze *et al.*, “How does thermal poling affect the structure of soda-lime glass?,” *J. Phys. Chem. C*, vol. 114, no. 29, pp. 12754–12759, 2010.
- [110] V. Pruneri, F. Samoggia, G. Bonfrate, P. G. Kazansky, and G. M. Yang, “Thermal poling of silica in air and under vacuum: The influence of charge transport on second harmonic generation,” *Appl. Phys. Lett.*, vol. 74, no. 17, pp. 2423–2425, 1999.
- [111] M. Dussauze, E. I. Kamitsos, E. Fargin, and V. Rodriguez, “Structural Rearrangements and Second-Order Optical Response in the Space Charge Layer of Thermally Poled Sodium–Niobium Borophosphate Glasses,” *J. Phys. Chem. C*, vol. 111, no. 39, pp. 14560–14566, Oct. 2007.
- [112] H. An and S. Fleming, “Investigating the effectiveness of thermally poling

- optical fibers with various internal electrode configurations,” *Opt. Express*, vol. 20, no. 7, p. 7436, 2012.
- [113] N. Bloembergen, R. K. Chang, S. S. Jha, and C. H. Lee, “Optical Second-Harmonic Generation in Reflection from Media with Inversion Symmetry,” *Phys. Rev.*, vol. 174, no. 3, pp. 813–822, 1968.
- [114] T. Christopoulos, O. Tsilipakos, G. Sinatkas, and E. E. Kriezis, “On the calculation of the quality factor in contemporary photonic resonant structures,” *Opt. Express*, vol. 27, no. 10, pp. 14505–14522, May 2019.
- [115] M. D. Ingram, C. T. Imrie, I. Konidakis, and S. Voss, “Significance of activation volumes for cation transport in glassy electrolytes,” *Phys. Chem. Chem. Phys.*, vol. 6, no. 13, pp. 3659–3662, 2004.
- [116] D. E. CARLSON, K. W. HANG, and G. F. STOCKDALE, “Ion Depletion of Glass at a Blocking Anode: II, Properties of Ion-Depleted Glasses,” *J. Am. Ceram. Soc.*, vol. 57, no. 7, pp. 295–300, 1974.
- [117] A. L. R. Brennand and J. S. Wilkinson, “Planar waveguides in multicomponent glasses fabricated by field-driven differential drift of cations,” *Opt. Lett.*, vol. 27, no. 11, p. 906, 2002.
- [118] M. Dussauze, E. Fargin, M. Lahaye, V. Rodriguez, and F. Adamietz, “Large second-harmonic generation of thermally poled sodium borophosphate glasses,” *Opt. Express*, vol. 13, no. 11, p. 4064, 2005.
- [119] N. J. Smith and C. G. Pantano, “Structural and compositional modification of a barium boroaluminosilicate glass surface by thermal poling,” *Appl. Phys. A Mater. Sci. Process.*, vol. 116, no. 2, pp. 529–543, 2014.
- [120] M. Dussauze, E. I. Kamitsos, E. Fargin, and V. Rodriguez, “Refractive index distribution in the non-linear optical layer of thermally poled oxide glasses,” *Chem. Phys. Lett.*, vol. 470, no. 1–3, pp. 63–66, 2009.
- [121] A. K. Yadav and P. Singh, “A review of the structures of oxide glasses by

- Raman spectroscopy,” *RSC Adv.*, vol. 5, no. 83, pp. 67583–67609, 2015.
- [122] W. L. Konijnendijk and J. M. Stevels, “The structure of borosilicate glasses studied by Raman scattering,” *J. Non. Cryst. Solids*, vol. 20, no. 2, pp. 193–224, 1976.
- [123] R. Oven, “Measurement of planar refractive index profiles with rapid variations in glass using interferometry and total variation regularized differentiation,” *J. Mod. Opt.*, vol. 62, pp. S53–S60, 2015.
- [124] C. De Bernardi *et al.*, “Effects of Potassium Concentration and Induced Stress on the Refractive Index Profile of K⁺-Na⁺ Ion-exchanged Glass Waveguides,” *J. Mod. Opt.*, vol. 35, no. 6, pp. 907–917, Jun. 1988.
- [125] Q. Li, T. Wang, Y. Su, M. Yan, and M. Qiu, “Coupled mode theory analysis of mode-splitting in coupled cavity system,” *Opt. Express*, vol. 18, no. 8, pp. 8367–8382, 2010.
- [126] M. Torculas, J. Medina, W. Xue, and X. Hu, “Protein-Based Bioelectronics,” *ACS Biomater. Sci. Eng.*, vol. 2, no. 8, pp. 1211–1223, Aug. 2016.
- [127] “<http://www.chim.lu/ech1025.php>.”.
- [128] P. Cebe, B. P. Partlow, D. L. Kaplan, A. Wurm, E. Zhuravlev, and C. Schick, “Silk I and Silk II studied by fast scanning calorimetry,” *Acta Biomater.*, vol. 55, pp. 323–332, Jun. 2017.
- [129] D. N. Rockwood, R. C. Preda, T. Yücel, X. Wang, M. L. Lovett, and D. L. Kaplan, “Materials fabrication from Bombyx mori silk fibroin,” *Nat. Protoc.*, vol. 6, no. 10, pp. 1612–1631, 2011.
- [130] R. L. DeRosa, P. A. Schader, and J. E. Shelby, “Hydrophilic nature of silicate glass surfaces as a function of exposure condition,” *J. Non. Cryst. Solids*, vol. 331, no. 1, pp. 32–40, 2003.
- [131] M. N. M. Nasir, G. S. Murugan, and M. N. Zervas, “Spectral cleaning and

- output modal transformations in whispering-gallery-mode microresonators,” *J. Opt. Soc. Am. B*, vol. 33, no. 9, pp. 1963–1970, 2016.
- [132] P. Monti, G. Freddi, A. Bertoluzza, N. Kasai, and M. Tsukada, “Raman spectroscopic studies of silk fibroin from *Bombyx mori*,” *J. Raman Spectrosc.*, vol. 29, no. 4, pp. 297–304, Apr. 1998.
- [133] O. Tsilipakos, T. V Yioultsis, and E. E. Kriezis, “Theoretical analysis of thermally tunable microring resonator filters made of dielectric-loaded plasmonic waveguides,” *J. Appl. Phys.*, vol. 106, no. 9, p. 93109, 2009.
- [134] J. A. Stratton, *Electromagnetic theory*. New York; London: McGraw-Hill Book Company, Inc., 1941.
- [135] O. Tsilipakos and E. Kriezis, “Microdisk resonator filters made of dielectric-loaded plasmonic waveguides,” *Opt. Commun.*, vol. 283, pp. 3095–3098, 2010.
- [136] H.-J. Jin and D. L. Kaplan, “Mechanism of silk processing in insects and spiders,” *Nature*, vol. 424, no. 6952, pp. 1057–1061, 2003.
- [137] T. Inoue, “Strain-Induced Birefringence of Amorphous Polymers and Molecular Design of Optical Polymers,” *ACS Appl. Polym. Mater.*, vol. 3, no. 5, pp. 2264–2273, May 2021.
- [138] T. Inoue, D.-S. Ryu, K. Osaki, and T. Takebe, “Viscoelasticity and birefringence of syndiotactic polystyrene. I. Dynamic measurement in supercooled state,” *J. Polym. Sci. Part B Polym. Phys.*, vol. 37, no. 4, pp. 399–404, Feb. 1999.
- [139] N. Minoura, M. Tsukada, and M. Nagura, “Fine structure and oxygen permeability of silk fibroin membrane treated with methanol,” *Polymer (Guildf)*, vol. 31, no. 2, pp. 265–269, 1990.
- [140] L. F. Drummy, D. M. Phillips, M. O. Stone, B. L. Farmer, and R. R. Naik, “Thermally Induced α -Helix to β -Sheet Transition in Regenerated Silk

- Fibers and Films,” *Biomacromolecules*, vol. 6, no. 6, pp. 3328–3333, Nov. 2005.
- [141] Z. He, T. Zhao, X. Zhou, Z. Liu, and H. Huang, “Sequential Order of the Secondary Structure Transitions of Proteins under External Perturbations: Regenerated Silk Fibroin under Thermal Treatment,” *Anal. Chem.*, vol. 89, no. 10, pp. 5534–5541, May 2017.
- [142] Z. Wang, Y. Cang, F. Kremer, E. L. Thomas, and G. Fytas, “Determination of the Complete Elasticity of *Nephila pilipes* Spider Silk,” *Biomacromolecules*, vol. 21, no. 3, pp. 1179–1185, Mar. 2020.
- [143] L.-D. Koh *et al.*, “Structures, mechanical properties and applications of silk fibroin materials,” *Prog. Polym. Sci.*, vol. 46, pp. 86–110, 2015.
- [144] G. S. Murugan, M. N. Petrovich, Y. Jung, J. S. Wilkinson, and M. N. Zervas, “Hollow-bottle optical microresonators,” *Opt. Express*, vol. 19, no. 21, pp. 20773–20784, 2011.
- [145] M. Ding, G. Senthil Murugan, G. Brambilla, and M. N. Zervas, “Whispering gallery mode selection in optical bottle microresonators,” *Appl. Phys. Lett.*, vol. 100, no. 8, p. 81108, 2012.
- [146] I. Konidakis, A. Karagiannaki, and E. Stratakis, “Advanced composite glasses with metallic{,} perovskite{,} and two-dimensional nanocrystals for optoelectronic and photonic applications,” *Nanoscale*, vol. 14, no. 8, pp. 2966–2989, 2022.
- [147] Y. Zhao, Y. Li, K. T. T. Hien, G. Mizutani, and H. N. Rutt, “Observation of spider silk by femtosecond pulse laser second harmonic generation microscopy,” *Surf. Interface Anal.*, vol. 51, no. 1, pp. 56–60, Jan. 2019.

Publications

Results of this thesis were Published in Academic Journals

[1] Korakas Nikolaos, Vassilis Tsafas, Odysseas Tsilipakos, Ioannis Konidakis, Bruno J. Moog, Chris Craig, George Filippidis, Dan Hewak, Michalis Zervas, and Stavros Pissadakis. 2022. ‘Whispering gallery mode resonances in thermally poled borosilicate glass hetero-fibers’, Journal of Lightwave Technology, p. 1. doi: 10.1109/JLT.2022.3164980.

[2] N. Korakas, D. Vurro, O. Tsilipakos, T. Vasileiadis, B. Graczykowski, A. Cucinotta, S. Selleri, G. Fytas, S. Iannotta and S. Pissadakis, 2023. "Photo-elasticity of silk fibroin harnessing whispering gallery modes" Nature Scientific Reports 13, 9750 (2023). <https://doi.org/10.1038/s41598-023-36400-0>

Publication in Academic Journals from other projects

[1] Violakis, Georgios & Korakas, Nikolaos & Pissadakis, Stavros. (2018). Differential loss magnetic field sensor using a ferrofluid encapsulated D-shaped optical fiber. Optics Letters. 43. 142. 10.1364/OL.43.000142.

[2] Korakas, Nikolaos & Violakis, Georgios & Mader, Arnaud & Pissadakis, Stavros. (2019). Azimuthal Alignment Method for Optimizing Bragg Grating Inscription in Photonic Crystal Fibers. IEEE Photonics Technology Letters. 31. 857-860. 10.1109/LPT.2019.2910461.

[3] Konstantaki, M.; Violakis, G.; Pappas, G.A.; Geernaert, T.; Korakas, N.; Tiriakidis, N.; Tiriakidi, T.; Tiriakidis, K.; Thienpont, H.; Berghmans, F.; Botsis, J.; Pissadakis, S. Monitoring of Torque Induced Strain in Composite Shafts with Embedded and Surface-Mounted Optical Fiber Bragg Gratings. *Sensors* 2021, 21, 2403. <https://doi.org/10.3390/s21072403>

Conference paper

[1] Konstantaki, Maria & Violakis, G. & Geernaert, Thomas & Korakas, Nikolaos & Tiriakidis, Nikolaos & Tiriakidi, Th & Tiriakidis, K. & Thienpont, Hugo & Berghmans, Francis & Pissadakis, Stavros. (2018). Optical Fiber Bragg Grating Sensors for Torque Induced Strain Monitoring in Filament Wound Composite Shafts. ThE98. 10.1364/OFS.2018.ThE98.

[2] Korakas, Nikolaos & Vurro, Davide & Tsilipakos, Odysseas & Cucinotta, Annamaria & Selleri, Stefano & Iannotta, Salvatore & Pissadakis, Stavros. (2021). Optical birefringence in strain tuneable silk fibroin whispering gallery mode cavities. 1-1. 10.1109/CLEO/Europe-EQEC52157.2021.9542304.

[3] Korakas, Nikolaos & Tsafas, Vassilis & George, Filippidis & Moog, Bruno & Craig, Christopher & Hewak, Daniel & Zervas, Michalis & Pissadakis, Stavros. (2021). Whispering gallery mode resonances in thermally poled borosilicate glass optical microcavities. 1-1. 10.1109/CLEO/Europe-EQEC52157.2021.9542571.